Signal Processing for Radar-Based Gait Analysis

Seifert, Ann-Kathrin

(2020)

ANN-KATHRIN SEIFERT

SIGNAL PROCESSING FOR RADAR-BASED GAIT ANALYSIS

SIGNAL PROCESSING FOR RADAR-BASED GAIT ANALYSIS

Dem Fachbereich Elektrotechnik und Informationstechnik
der Technischen Universität Darmstadt

TECHNISCHE
UNIVERSITÄT
DARMSTADT

zur Erlangung des akademischen Grades eines
Doktor-Ingenieurs (Dr.-Ing.)
genehmigte Dissertation von

ANN-KATHRIN SEIFERT, M.SC.

Erstgutachter: Prof. Dr.-Ing. Abdelhak M. Zoubir
Zweitgutachter: Prof. Dr. Moeness G. Amin

Darmstadt 2020

Seifert, Ann-Kathrin – *Signal Processing for Radar-Based Gait Analysis*
Darmstadt, Technische Universität Darmstadt
Jahr der Veröffentlichung der Dissertation auf TUprints: 2020
URN: urn:nbn:de:tuda-tuprints-142281
Tag der mündlichen Prüfung: 17.09.2020

ACKNOWLEDGMENTS

I would like to thank everyone who contributed to the success of this work and supported me during the time of my doctoral studies.

First of all, I sincerely thank my supervisor Prof. Dr.-Ing. Abdelhak M. Zoubir for giving me the opportunity to pursue my Ph.D. at the Signal Processing Group. Thank you for your guidance and support, and for giving me the chance to work with so many outstanding people throughout the last five years.

Further, my deepest gratitude to my co-supervisor Prof. Dr. Moeness G. Amin. Thank you for always providing valuable feedback on my work, whether through discussions or in written form. Thank you for inviting me to you lab, the Center for Advanced Communications at Villanova University, USA, where I could collect my first experimental data. It has been truly inspiring to work with you.

I also would like to thank Prof. Dr. mont. Mario Kupnik, Prof. Dr.-Ing. Anja Klein, and Prof. Dr. rer. nat. Sascha Preu for being on my committee.

A huge thank you goes to all current and former members of the Signal Processing Group who made the last few years most enjoyable. It has been a pleasure working with Dr.-Ing. Sara Al-Sayed, Jack Dagdagan, Dr.-Ing. Christian Debes,[1] Dr.-Ing. Nevine Demitri,[1] Mahmoud El-Hindi, Dr.-Ing. Michael Fauss,[1] Dr. Stefano Fortunati,[1] Dr.-Ing. Lala Khadidja Hamaidi,[1] Prof. em. Dr.-Ing. Eberhard Hänsler, Dr. Roy Howard, Huiping Huang,[1] Amare Kassaw,[1] Dr.-Ing. Sahar Khawatmi,[1] Dr.-Ing. Mark Ryan Leonard,[1] Toufik Mouchini, Dr.-Ing. Michael Muma,[1] Afief Dias Pampudi,[1] Prof. Dr.-Ing. Henning Puder,[1] Ziliang Qiao, Christian Schroth, Sergey Sukhanov,[1] Dr.-Ing. Wassim Suleiman, Dr.-Ing. Christian Weiss, Dr.-Ing. Wenjun Zeng. I thank Dr.-Ing. Tim Schäck, Patricia Binder, Dr.-Ing. Freweyni Kidane Teklehaymanot,[1] Aylin Taştan, and Jasin Machkour for the interesting conversations and wonderful time that we had in our office. A very special thanks to Dr.-Ing. Jürgen Hahn,[1] Di Jin,[1] Dr.-Ing. Simon Rosenkranz,[1] and Dr.-Ing. Adrian Šošić[1] for the most memorable c(h)onference trip ever. Thanks a lot to Martin Gölz[1] and Dominik Reinhard[1] for valuing (regular) coffee breaks as much as I do – even in home office times (thanks also to David Schenck[1]).

A special thanks goes to Renate Koschella and Hauke Fath for their help and support regarding administrative, technical and all other issues throughout all these years.

I would also like to thank everybody from the Center for Advanced Communications at Villanova University, USA, who supported and inspired me in various ways. Thank you for welcoming me so warm-heartedly in your group when I visited in spring 2016. A special thanks to Prof. Dr. Fauzia Ahmad and Dr. Baris Erol[1] for helping me with the experiments, even when I was back in Germany already. Thanks a lot to Janice Moughan for taking care of the arrangements for my stay as well as various conference visits. Thanks to Dr. Xiangrong Wang[1] and Dr. Maryam Hajebi for being so kind to let me stay with you. Thanks to my sister-in-mind Dr. Branka Jokanović[1] for being so much fun.

I sincerely thank Dr. Martin Grimmer from the Institute of Sport Science at Technische Universität Darmstadt for collaborating and for providing the Locomotion Laboratory that made it possible to conduct a gait study. In particular, I

1 with these persons I had the pleasure to travel to or meet at various conferences in China, USA, Italy, and Spain – thanks for all the great memories!

thank you for your open-mindedness, the enriching discussions, and the help with the data collection.

Thanks a lot to everyone who took the time and participated in my experiments (most of which are mentioned above). Without you this research could not have been possible. In this context, I would also like to thank Prof. Dr. Suzanne Smeltzer from the Center of Nursing Research at Villanova University, USA, who helped to get in touch with individuals with diagnosed gait disorders.

Finally, I would like to thank my family and friends for always being there for me during this challenging time. Thanks to my parents, Berthold and Hildegard, and my brother, Philipp, for always supporting me and never having any doubts in me achieving my goals. Thank you, Basti, for encouraging me to pursue a Ph.D. in the first place. Thank you, Laura, for always having a good advice (also beyond design issues). Thank you, Caro, for encouraging me to do so much more.

Last but not least, I would like to thank Jonas for always supporting me and being so patient with me.

Darmstadt, October 2020

KURZFASSUNG

In dieser Dissertation werden Signalverarbeitungsmethoden für die radarbasierte Ganganalyse entwickelt. Analysiert man die von einem sich bewegenden, nicht starren Objekt zurückgestreuten Hochfrequenzwellen im Zeit-Frequenz-Bereich, sind sogenannte Mikro-Doppler-Signaturen erkennbar. Betrachtet man eine laufende Person, besteht eine Beziehung zwischen den Mikro-Doppler-Signaturen und den kinematische Informationen des Gangs, da Geschwindigkeit, Beschleunigung und Rotation der einzelnen Körperteile erfasst werden. Demnach können diese Radar-Mikro-Doppler-Signaturen zur allgemeinen Gangklassifikation und zur grundlegenden Ganganalyse herangezogen werden.

Im Bereich der Radar-basierten Gangklassifizierung wird ein Signalverarbeitungskonzept entwickelt, um zwischen fünf Laufstilen zu unterscheiden, darunter anormaler Gang und das Gehen mit einem Gehstock. Dazu werden verschiedene mehrdimensionale Signaldarstellungen, einschließlich des Spektrogramms und des sogenannten Kadenz-Geschwindigkeits-Diagrams, berücksichtigt. Diese Darstellungen werden zur Ermittlung physikalisch interpretierbarer Merkmale und als Ausgangspunkt für das automatisierte Lernen von Merkmalen mit Hilfe der Hauptkomponentenanalyse verwendet. Die so erhaltenen Merkmalssätze werden bezüglich ihrer entsprechenden Klassifizierungsleistung bewertet und verglichen. Zusätzlich wird ein Gangasymmetrie-Detektor vorgestellt, um Unterschiede zwischen den Bewegungen des linken und rechten Beins anhand von Radar-Mikro-Doppler-Signaturen zu erkennen. Die Bewertung der entwickelten Methoden erfolgt auf der Grundlage realistischer experimenteller Radardaten von zehn gesunden Personen und vier Personen mit diagnostizierten Gangstörungen.

Im Hinblick auf eine Radar-basierte Ganganalyse demonstriert die vorliegende Arbeit den Nutzen des Doppler-Radars zur Messung einer Reihe medizinisch relevanter Gangparameter, einschließlich der Schrittzeit und der maximalen Geschwindigkeiten der unteren Extremitäten. Hierbei wird eine neue Methode zur Messung der Flugzeit mittels Radar vorgestellt. Insgesamt werden elf biomechanische Gangparameter extrahiert und mit Hilfe Marker-basierter Motion-Capture-Daten qualitativ und quantitativ evaluiert. Darüber hinaus werden parametrische Modelle für die Radialgeschwindigkeiten der unteren Extremitäten während des Gehens entwickelt. Diese Modelle werden dann verwendet, um die Gelenkwinkel der unteren Extremitäten, d.h. den Hüft- und Kniewinkel, aus Radar-Mikro-Doppler-Schrittsignaturen zu bestimmen. Die entwickelten Methoden werden anhand experimenteller Daten von neunzehn gesunden Testpersonen, die auf einem Laufband gehen, evaluiert. Dabei wird eines der Knie durch eine verstellbare Orthese systematisch eingeschränkt, um verschiedene Grade von Ganganomalie zu simulieren.

Die Ergebnisse dieser Arbeit zeigen die Leistungsfähigkeit von Radar, Gangunterschiede zu erfassen. Insbesondere ermöglichen die entwickelten Signalverarbeitungsmethoden die Unterscheidung zwischen verschiedenen Gehstilen, sowie die Messung medizinisch relevanter Gangparameter anhand von Radar-Rückstreuungen. Damit wird gezeigt, dass die Hochfrequenzsensorik eine geeignete Technologie für die unauffällige Ganganalyse im häuslichen Umfeld darstellt. Die vorliegende Arbeit leistet somit einen Beitrag zum immer

wichtiger werdenden Anwendungsbereich des Radars für die Beobachtung von Menschen in Innenräumen mit Anwendung z.B. im Bereich der Telemedizin und des betreuten Wohnens.

ABSTRACT

In this PhD thesis signal processing methods are developed for radar-based gait analysis. Analyzing the backscattered radio frequency waves from a moving non-rigid target in the time-frequency domain, reveals so-called micro-Doppler signatures. In the case of a walking person, these micro-Doppler signatures relate to gait kinematics by capturing velocity, acceleration, and rotation of individual body parts. Hence, they can be exploited for general gait classification and basic gait analysis.

In the area of radar-based gait classification, a signal processing framework is developed to discriminate between five walking styles, including abnormal and cane-assisted gait. Toward this end, different joint-variable signal representations, including the spectrogram and the so-called cadence-velocity diagram, are adapted. These representations are used to identify physically interpretable features, and as input to automatic feature learning using principal component analysis. The thus obtained feature sets are evaluated and compared in terms of their corresponding classification performance. Additionally, a gait asymmetry detector is presented to identify differences between the left and right leg's motions from radar micro-Doppler signatures. The evaluation of the developed methods is based on realistic experimental radar data of 10 able-bodied individuals, and four persons with diagnosed gait disorders.

Toward radar-based gait analysis, the thesis demonstrates the use of Doppler radar for measuring a set of medically relevant gait parameters, including stride time and maximal lower limb velocities. Here, a new method is presented for measuring the flight time through a radar device. In total, 11 biomechanical gait parameters are extracted and qualitatively and quantitatively assessed by using marker-based motion capture data. Further, parametric models for the radial velocities of the lower limbs during walking are developed. These models are then employed to estimate lower limb angular kinematics, namely, the hip and knee angle, from radar micro-Doppler step signatures. The developed methods are evaluated based on experimental data of 19 able-bodied test persons walking on a treadmill. Here, one of the knees was systematically restricted through an adjustable orthosis to simulate different degrees of gait abnormality.

The results of this thesis demonstrate the capabilities of radar to capture differences in gait patterns. In particular, the developed signal processing frameworks allow for discriminating between different walking styles and the measurement of medically relevant gait parameters based on radar backscatterings. Thus, it is shown that radio frequency sensing is a viable technology for unobtrusive in-home gait analysis. As such, this thesis contributes to the growing field of radar for indoor human monitoring with application to, e.g., telemedicine and assisted living.

CONTENTS

LIST OF FIGURES

LIST OF TABLES

ACRONYMS

2D two-dimensional

2D-PCA two-dimensional principal component analysis

2D2D-PCA two-directional two-dimensional principal component analysis

3D three-dimensional

10FCV 10-fold cross-validation

ACC classification accuracy

ADL activities of daily living

BIC Bayesian information criterion

CVD cadence-velocity diagram

CW walking with a cane in sync with one leg

CW/OOS walking with a cane out of sync with any leg

EM electromagnetic

FNR false negative rate

FPR false positive rate

FT Fourier transform

FF fundamental frequency

FMCW frequency modulated continuous wave

GAN generative adversarial network

GRF ground reaction force

HAR human activity recognition
IF instantaneous frequency
LOSOCV leave-one-subject-out cross-validation
L1 limping with one leg
L2 limping with both legs
LOS line-of-sight
LLS linear least squares
MAE mean absolute error
MCS mean cadence spectrum
MoCap motion capture
MSE mean squared error
MSSIM mean structural similarity index
NN nearest neighbor
NLS nonlinear least squares
NW normal walking
NOH number of harmonics
PIR passive infrared sensor
PCA principal component analysis
RCS radar cross section
RF radio frequency
RMSE root mean squared error
ROC receiver operating characteristic
SD standard deviation
STFT short-time Fourier transform
SVD singular value decomposition
SSIM structural similarity
SOH sum-of-harmonics
SVM support vector machine
TFR time-frequency representation
TPR true positive rate

1 INTRODUCTION

World-wide, the population aged over 60 years is growing [Wor18]. As shown in Fig. 1.1, the proportion of this age group to the total population is predicted to nearly double between 2015 and 2050, from 12 % to 22 % [Wor18; Uni19a]. As such, the growth in proportion of the elderly is increasing more dramatically compared to previous decades [Wor18]. This phenomenon is also known as population aging [Wor18]. In Germany and the USA, the percentages of population aged 60 years or over have already reached 29 % and 23 %, respectively, in 2020 [Uni19a].

population aging

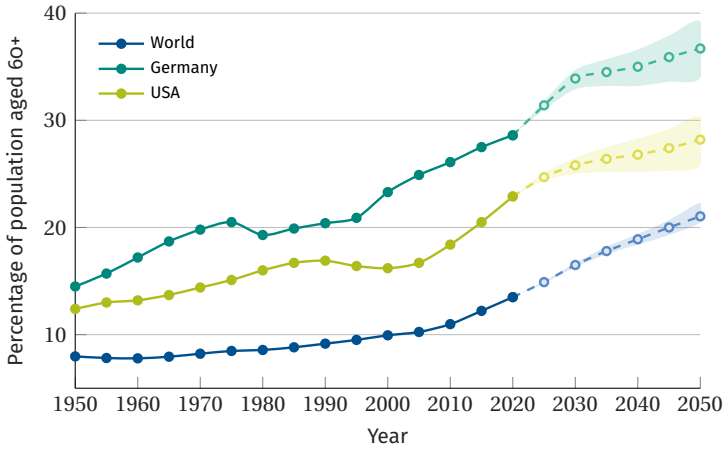

Figure 1.1: The percentage of population aged 60 years or over. From 2020 onward, the graphs show the median of predicted proportions along with the 95 % confidence intervals. [Uni19a; Uni19b]

The quality of life, which often goes along with good health, is a key factor for the elderly to actually benefit from the extra years of life. Measures for supporting *healthy aging* include the development of people-centered and integrated health services[1] [Wor18]. To this end, ambient assisted living technologies have become the focus of many research activities to provide seamless *in-home* health monitoring [BMB+16]. Seniors desire to live independently in their own homes as long as possible. This is not only understandable, but also from a clinical point of view, *aging in place* has been shown to be advantageous over moving to assisted living facilities or nursing homes [MPP+05]. Further, people with disabilities and individuals living in geographically isolated communities benefit from remote health services.

aging in place

One way to assess the general state of individual health is through gait analysis. The human gait is a complex motion and requires the concerted interaction between many systems, including strength, sensation and coordination [LRW12]. Gait analysis encompasses the measurement and assessment of quantities that characterize human locomotion. For a variety of diseases, clinical research has shown that gait analysis can facilitate diagnosis and enhance

gait analysis

1 the term *integrated health services* refers to "the organization and management of health services so that people get the care they need, when they need it, in ways that are user-friendly, achieve the desired results and provide value for money." [Wor08]

patient treatment. Pathologies affecting the gait include, e.g., neurodevelopmental disorders (e.g. cerebral palsy and Down syndrome) and neurodegenerative disorders (e.g. Parkinson's and Alzheimer's disease) [JPL+18; GTK+17; CLLY16; WBH+15]. Thus, gait analysis is, e.g., employed in geriatrics (e.g. fall risk assessment), orthopedics, prosthetics, and rehabilitation (e.g. post stroke) [JPL+18; CLLY16; GRWS19; BWH06; PK17]. Further, gait analysis is important in the areas of biomechanical research, sports medicine and athletic training.

This thesis is concerned with signal processing for radar-based gait analysis. In so doing, the doctoral research contributes to the need for innovative technological solutions for remote health services.

In the following, Section 1.1 elaborates on the motivation for using radio frequency (RF) sensing for human gait analysis. The state of the art and the thesis' contributions in the area of signal processing for radar-based gait analysis are summarized in Section 1.2. Finally, Section 1.3 gives an overview of the thesis structure, while Section 1.4 lists the publications that have been produced during the period of doctoral candidacy.

1.1 MOTIVATION

Thorough clinical gait studies are often time-consuming, costly and lack reproducibility [Sim04]. For this reason, numerous ongoing research efforts aim at developing cost-efficient technologies for unobtrusive and long-term gait analysis. A great variety of sensors have been proposed for analyzing the gait. Here, we focus on systems that are capable of providing pervasive locomotion monitoring *in home*, e.g., to support aging in place and enable independence in assisted living [DMS+16]. These systems can broadly be categorized into wearable[2] (direct) and non-wearable (indirect) solutions [MGM14]. While wearable sensors are typically directly attached to a person or to their clothes, non-wearable sensors are deployed (stationary) within the home. However, wearable sensors require precise placement, necessitate the user's cooperation and can be uncomfortable to wear. For these reasons, non-wearable technologies are desirable.

mobile gait analysis

The diagram in Fig. 1.2 gives an overview of state-of-the-art non-contact sensing modalities for gait recognition and analysis. Typically, there is a trade-off between the *richness of information* provided by the sensor, and the *perceived privacy* by the user. In particular for in-home scenarios, the latter typically defines the user's acceptance of the device.

non-wearable sensors

The least informative sensors to be used for gait analysis are passive infrared sensors (PIRs). Designed as motion detectors, they operate a near infrared light[3] and recognize motions in their field of view. Using multiple PIR sensors, the average gait velocity can be calculated based on the detection times of the individual sensors [RAJ+16; KMD+12; HAH+10].

passive infrared sensors

Another cheap and non-intrusive way to analyze the walking pattern of a person, is to use microphones. The sound of the feet while walking can be used to infer spatiotemporal gait parameters for basic gait analysis [UBJ15]. Also, the acoustic gait information can enrich gait analysis systems when combined with other sensors [HGB+14]. However, the performance of audio-based systems can easily be affected by ambient noise, footwear and floor cover material. Operating at frequencies higher than the upper audible limit of human hearing,

sound-based systems

2 for reviews on wearable technologies for gait analysis see e.g. [JPL+18; ELB+17; CLLY16; TLZF12]
3 electromagnetic (EM) waves with wavelengths in the range of 0.72 µm to 1.3 µm [CW11]

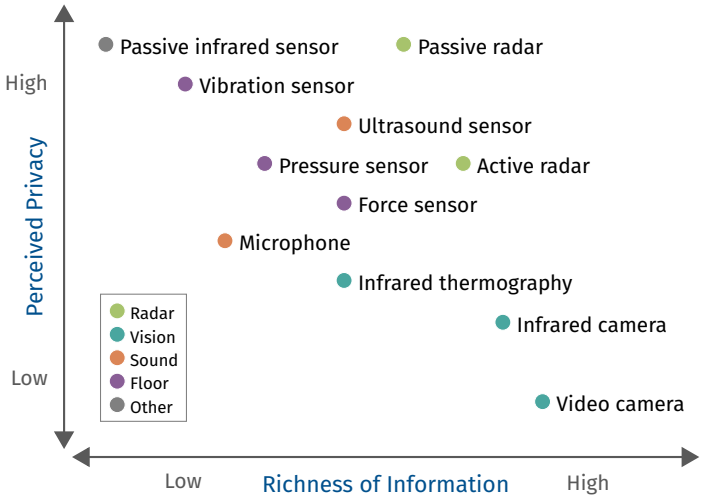

Figure 1.2: Overview of non-wearable ambient solutions for in-home gait analysis. Typically, there is a trade-off between the richness of information provided by the sensor, and the perceived privacy by the user. (adapted from [DMS+16])

the use of active ultrasound sensors have been investigated for gait recognition [GCBS17; DBMS13; BCW11; MSBE10; KR07]. However, it is currently not possible to separate motions of several people in the field of view of the sensor, e.g., by exploiting range information.

floor sensors

For the measurement of spatiotemporal gait parameters, instrumented walkways with integrated force platforms or pressure sensors have been employed [DMP+17; GZA09]. While the use of so-called ground reaction forces (GRFs) is well established in clinical gait analysis [Kir06], portable gait mats have the disadvantages that they are of limited size and the person has to walk on a predefined course [MGM14]. More recently, less intrusive low-cost vibration sensors have been studied for indoor human motion sensing [CLVS20]. Being placed on the floor throughout a home along usual pathways, they capture the vibrations in the floor caused by a walking person.

vision-based sensors

The most widely studied marker-less motion capture systems[4] for gait analysis are cameras.[5] Operating at visible light [CHSW17; WSS+13] or near-infrared light,[3,6] [LCAL19; GTK+17; XMC+15; EG15; PWBN14; SS13] they provide frontal or sagittal views on a person's gait in form of videos. Utilizing long-wavelength infrared radiation,[7] infrared thermography provides silhouette information based on the contrast between the person's surface temperature, and that of other objects and the background. Thus, basic gait patterns can be recognized from the infrared thermography images [XMS+10]. However, despite recent advances in vision-based marker-less gait monitoring systems, their performance is still limited to laboratory conditions and using a large number of cameras [CECS18]. Typically, this type of sensor requires the entire body to be in the field of view to extract and track the silhouette of the subject accurately. Then, the human posture is modeled by locating a finite number of points on the skeleton. In practical scenarios, vision-based systems are easily affected by distance, lighting conditions, shadowing and clothing. While depth cameras

4 "standard" motion capture systems operate with multiple infrared cameras and passive reflective *markers* that are attached to the test subject; hence, they are not *marker-less*
5 for a review on vision-based motion analysis see e.g. [CECS18]
6 this includes the use of the Microsoft Kinect
7 EM waves with wavelengths in the range of 8 µm to 15 µm [CW11]

utilizing (structured) infrared light are generally considered unobtrusive, the perceived privacy of video cameras is low, and thus they are less accepted as an in-home modality.

radio-frequency sensors

In this thesis, the applicability of radio frequency (RF)[8] sensing for gait analysis is investigated. Since it is contact-less, privacy-preserving, and does not require any instrumentation on the user, it is a viable technology for continuous and unobtrusive in-home gait monitoring. Further, radar[9] systems can be used in conjunction to other wearable and non-wearable sensors. The advantages of RF sensing are that it is not sensitive to lighting conditions, clothing and background complexity, that usually affect vision-based systems. Further, RF sensors can be installed discretely, since radio waves can penetrate common materials [CW11]. While in this thesis only active radar systems are considered, it is noted that passive RF modules have been used for human activity classification [LTP18]. Passive radar systems do not send EM waves but exploit *signals of opportunity* by, e.g., leveraging existing communication signals, such as Wi-Fi [JCM+18].

micro-Doppler effect

Human activities may be recognized using radar by exploiting features caused by the so-called micro-Doppler effect [Che19]. In the Doppler domain, the resulting micro-Doppler signatures occur as modulations around the carrier frequency of the transmitted EM wave. Representing them in a joint time-frequency domain provides an additional time dimension which accounts for the time-varying nature of the observed motions. These micro-Doppler signatures are characteristic for targets' motions, and, thus, are the basis of discriminating movements. Specifically, in the case of a walking human, the micro-Doppler signatures describe gait kinematics by capturing velocity, acceleration, and rotation of individual body parts.

radar for indoor monitoring

Throughout the last two decades, RF sensing has gained much attention in the field of human activity recognition (HAR) for indoor human monitoring.[10] Figure 1.3 illustrates various applications of radar for indoor monitoring and corresponding motion classes, along with some examples of motions.

Remote health and *telemedicine* describe the service of long-distance diagnosis and monitoring via telecommunication technologies. In this context, the RF sensing technology, through active or passive radar devices, has gained much attention in the recent past [SF19; FLS19]. Here, radar has been employed for non-contact vital sign monitoring, with application to the detection of, e.g., sudden infant death syndrome or sleep apnea [ZHM+18; HZG+18; LZS+17; SIT+16; WSRC14].

Closely related to remote health and telemedicine are the concepts of *assisted living* and *aging in place*, which have the goal to empower seniors to live independently and safely in their own homes as long as possible. Besides vital sign monitoring, radar has been successfully applied for the detection of medical emergencies such as falls [JA18; AZAH16; JAA16; SHRS15]. Another important concept in ambient assisted living is monitoring activities of daily livings (ADLs), which helps to assess a person's functional status, and, thus, the ability to live independently [DMS+16]. In case of radar-based recognition, these activities are often considered in combination with other motions, such as walking [EGA20; EA19; SÖG18; JAE17; BPH15; KL09].

8 the RF spectrum comprises EM waves with wavelengths in the range of 1 mm to 100 km [Ell16]
9 the word *radar* is an acronym for radio dection and ranging and "as a palindrome, this name also evokes the basic send/echo idea behind these measurement systems" [CB09]
10 for an overview see e.g. [GA19; LFD+19; MPGL17; Ami17; LPH+17]

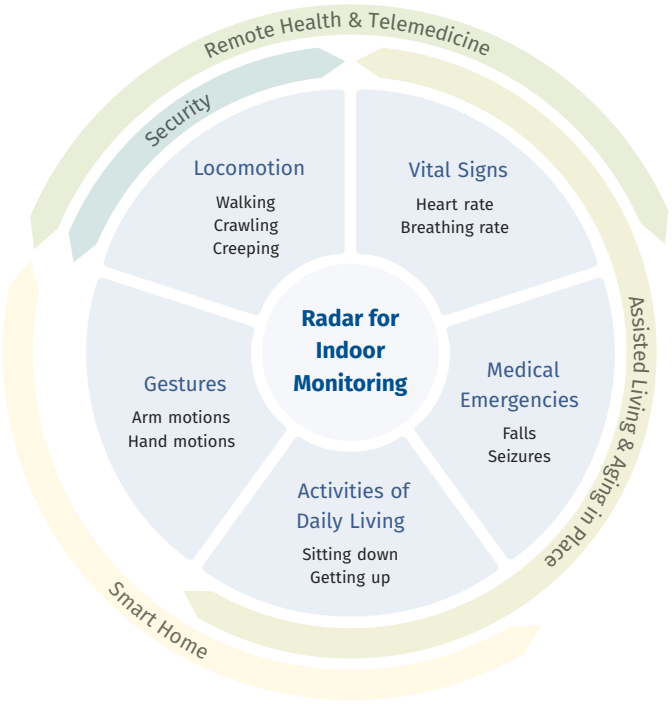

Figure 1.3: Overview of radar for indoor human motion sensing, where applications can broadly be categorized into remote health & telemedicine, assisted living & aging in place, smart home, and security. In practice, neither motion classes nor applications are strictly distinct and often overlap. (adapted from [GA19])

Beyond health-related applications, locomotion recognition, in general, is key to *security* applications such as intruder detection. In this regard, RF sensing has been employed for the detection [KM16; KHK15] and identification [VKJ+18; CLFG18; KM16; RB15] of individuals.

Finally, radar has recently become of increased interest for *smart home* applications to automatically control lighting scenes and appliances based on ADLs, or to facilitate man-machine interaction via hand gesture [AZS19; GL17] or arm motion recognition [ZAS20].

1.2 STATE OF THE ART AND CONTRIBUTIONS

The main contributions of this thesis fall into two areas. In the field of Radar-Based Gait Classification, the aim is to distinguish between different walking styles within the class of human gait. As such, we deal with an *intra-motion category* classification problem. In this context, also the influence of walking aids on the radar backscatterings is considered. Since, in practice, gait classes are neither distinct nor always known, the next step is to move Toward Radar-Based Gait Analysis. Using RF sensing, the aim is to provide medical practitioners and physiotherapists with commonly accepted gait parameters to assist in therapy. In the following, the state of the art is separately reviewed for the respective areas, and corresponding contributions in this thesis are summarized.

1.2.1 *Radar-Based Gait Classification*

Human gait has first been studied using radar in, e.g., [Che08; CLHW06; GMG01]. Early investigations focused on extracting basic gait parameters, such as the stride rate, stride length and walking speed to detect a person's presence and to discern human walking patterns from animal ones [TS09; HD08; Ote05]. More advanced radar-based gait classification methods were concerned with discriminating between walking with and without arm swinging [TPB15; TBA10; LIA10; OSA11; WF11; MA09], walking while holding an object [CLFG18; FRG15; LPTB12], or different walking speeds [RB15; CPM+15].

More recently, radar-based detection of walking aids has gained increased interest, but has not been widely examined yet. Amin *et al.* [AAZB15b; AAZB15a] were first to show that walking aids, such as a cane or a walker, can be detected by carefully analyzing the back-scattered radar signal. Later, Gürbüz *et al.* [GCBS17] investigated the effect of various walking aids on the characteristics of radar return signals. Different degrees of mobility were examined, namely, unaided walking, simulated limping, walking with a cane/tripod or a walker, and using a wheelchair. More recently, Seyfiouğlu *et al.* [SÖG18] used a deep convolutional autoencoder for discriminating 12 classes of aided and unaided indoor human activities, whereof half were gait motions including walking with a cane or a walker.

While all of the above works considered gait motions, none of them focused solely on the differences in micro-Doppler signatures due to altered lower limb motions or the use of walking aids. Considering medical applications of radar-based gait analysis, a deepened understanding of these effects is required before RF sensing can be employed in practical in-home gait monitoring systems. In this regard, it is noted that only few works have considered human movements with the radar having a back-view on the person, see e.g. [BPH15; WSRC14]. However, none of them elaborates on the possible differences in micro-Doppler gait signatures when receding from or approaching the radar system.

In terms of radar-based gait classification, the original contributions of this thesis are constituted by:

- *Section 5.1.1* **Detailed analysis and biomechanical interpretation of radar micro-Doppler gait signatures:** Through extensive experiments, it is shown that radar backscatterings of human locomotion are distinctively different when observing the motion from the front compared to from behind. This behavior can be exploited for the detection of abnormal steps and cane motions. [SAZ17a]

- *Section 6.1.1* **Extraction of physically interpretable features:** By utilizing different joint-variable radar signal representations pertinent features that have a physical meaning, such as the step rate, are obtained from experimental radar data. Here, the spectrogram, the so-called cadence-velocity diagram (CVD), and signals derived from these are considered. [SZA17; SAZ18; SAZ19]

- *Section 6.1.2* **Extraction of subspace-based features:** By using automated data-driven feature learning techniques, namely, principal component analysis (PCA) and its extensions, the offerings of two-dimensional (2D) radar signal representations are examined for the classification of different walking

styles. Here, the spectrogram, the CVD, and signals derived from these are considered. [SZA17; SSAZ18; SAZ19]

- **Evaluation and comparison of different feature sets for the classification of five walking styles:** Novel and state-of-the-art feature sets are compared by means of their ability to discern between five different gait classes, including normal walking, simulated limping and assisted gait. The performance of the proposed framework is evaluated using experimental radar data of 10 able-bodied test subjects and four individuals with diagnosed gait disorders. [SAZ19] *Section 6.2*

- **Development of a framework for automated gait asymmetry detection:** Micro-Doppler step signatures are automatically extracted from radar measurements of short duration. Then, image-based features and physical features are calculated to quantify the (dis)similarity between consecutive steps. Based on these features, a subsequent detector is designed to recognize gait asymmetry at a limited rate of false alarms. The performance of the proposed framework is evaluated based on experimental radar data of 10 able-bodied volunteers and four individuals with diagnosed gait disorders. [SZA19] *Chapter 7*

1.2.2 *Toward Radar-Based Gait Analysis*

In order to employ radar systems as medical tools, the aim is to capture spatiotemporal and kinematic gait parameters, such as the flight time or the swing velocity of the feet, since they are valuable to clinicians for assessing the gait (see e.g. [SMF+17; SCC+19; WBH+15] as well as references in [JPL+18]). In this regard, relevant prior research on radar-based gait analysis includes the work of Wang *et al.* [WSRC14], who employed pulse-Doppler radar to estimate the step time and the walking speed of 13 volunteers. Further, based on radar micro-Doppler signatures of 74 seniors, Saho *et al.* [SUSM19] showed that not only the walking speed, but also leg and foot velocities are indicative for lower cognitive functions in the elderly.

A way to objectively assess the capabilities of RF sensing for basic gait analysis is to compare radar-based gait parameters to simultaneously recorded marker-based motion capture (MoCap) data. The latter have previously been utilized for interpreting and simulating micro-Doppler gait signatures [RGC17; Che19]. For example, in automotive scenarios, Held *et al.* [HSK+18] used MoCap data for analyzing micro-Doppler signatures of human gait for enhanced pedestrian detection and early movement prediction. Karabacak *et al.* [KGG+15] utilized MoCap data and the commonly used global human walking model by Boulic, Magnenat-Thalman and Thalman [BTT90] to simulate micro-Doppler gait signatures and validated their use for classification. By use of motion capturing, Abdulatif *et al.* [AAKS17] developed an improved motion model for tracking individual body components based on radar measurements. However, most of these works merely qualitatively discuss the consistency between radar measurements and (simultaneously) recorded MoCap data.

Eventually, for a more advanced gait analysis, one would like to move beyond discrete biomechanical measures in order to gain insights into the underlying gait mechanisms. Analyzing the time-varying gait kinematics over an entire gait cycle allows for better identification of subtle changes in the gait profile. In this regard, e.g., the lower limb joint velocities and angles are of interest. The former

are revealed by time-frequency analysis of the backscattered radar signals, since the measured Doppler shift is directly proportional to the velocities of the body parts.

Here, the global human walking model by Boulic *et al.* [BTT90] has also been used for describing the lower limb joint kinematics. For example, in [vDG03; vDG08], van Dorp and Groen exploited this relation and presented model- and feature-based approaches to estimate the gait cycle frequency and length from experimental micro-Doppler signatures with the goal to minimize the difference between simulated and measured data.

In this research area, the thesis advances the state of the art as follows:

Chapter 10

- **Extraction of biomechanical gait parameters:** Novel and existing methods are employed to extract 11 spatiotemporal and kinematic parameters from radar micro-Doppler signatures. Based on experimental data of 19 able-bodied test subjects walking on an instrumented treadmill, the accuracy of the extracted gait parameters is assessed through simultaneously recorded marker-based motion capturing utilizing GRFs. Five degrees of gait abnormalities are investigated, which were introduced by an adjustable orthosis, such that one of the knees could not be fully bent. [SGZ20]

Section 11.1

- **Formulation of parametric models for lower limb joint velocities:** By combining the global human walking model by Boulic, Magnenat-Thalmann, and Thalmann [BTT90], describing the positioning of lower limb joints during walking, and the bilateral symmetric model for the angular kinematics of the lower limb joints [YNC04], models for the radial knee and ankle velocities are formulated. The models' parameters directly reflect biomechanical gait characteristics and thus allow to account for gait abnormalities.

Section 11.2

- **Estimation of lower limb angular kinematics:** Using the above parametric models for the lower limb joint velocities, the corresponding angular kinematics, namely, the time-varying hip and knee angles, are estimated from micro-Doppler step signatures via Hough transform. Experimental data of 19 able-bodied test subjects are used to assess the accuracy of estimated angle trajectories in comparison to simultaneously recorded marker-based motion capturing utilizing GRFs.

1.2.3 *Additional Contributions*

In cooperation with colleagues, three conference papers have been published during the period of doctoral candidacy. The respective achievements will not be detailed in this thesis, but are summarized below:

- **Unsupervised person enumeration and labeling:** Based on experimentally assessed micro-Doppler stride signatures of four persons, an unsupervised clustering enumeration and labeling algorithm is employed to first estimate the numbers of clusters in the data set, i.e., the number of individuals observed by the radar, and then identify individuals by assigning distinct labels to the clusters. In addition, the performance of the cluster enumeration and labeling algorithm is evaluated in a sequential manner: whenever new radar measurements become available, the number of clusters is re-estimated. It is shown that the proposed method

is able to correctly estimate the number of persons, and track the change in the number of individuals as we observe more data. [TSM+18]

- **Robust and sequential detection of gait asymmetry:** Combining ideas of robust statistics and sequential analysis, an online approach for radar-based gait analysis is proposed. To this end, the radar micro-Doppler signatures are analyzed and salient features are extracted, which quantify the (dis)similarity between consecutive steps, and, thus, gait (a)symmetry. The distributions of these features under each gait class are obtained by means of kernel density estimation. To account for the inaccuracies of the density estimation, an uncertainty model is used to obtain a set of most similar distributions. These distributions are then employed to construct a sequential probability ratio test to render a fast and reliable decision about the underlying gait class. Based on real radar data, it is shown that the proposed approach can achieve high detection rates at reduced measurement durations. [SRZA19]

- **Robust genetic algorithm for the prediction of the maximal knee angle during walking:** Given a set of radar features, the maximal knee angle during walking is predicted using a new robust genetic algorithm based nonlinear regression method. It simultaneously performs feature selection, parameter optimization for the support vector machine and outlier rejection by encoding these aspects into the chromosome design. Using experimental radar data, it is shown that the proposed algorithm significantly outperforms competing methods in terms of prediction accuracy. [DSMZ19]

1.3 THESIS OVERVIEW

Following this introduction, the doctoral thesis is organized into four parts, as illustrated Fig. 1.4, where the main contributions are detailed in Parts II and III.

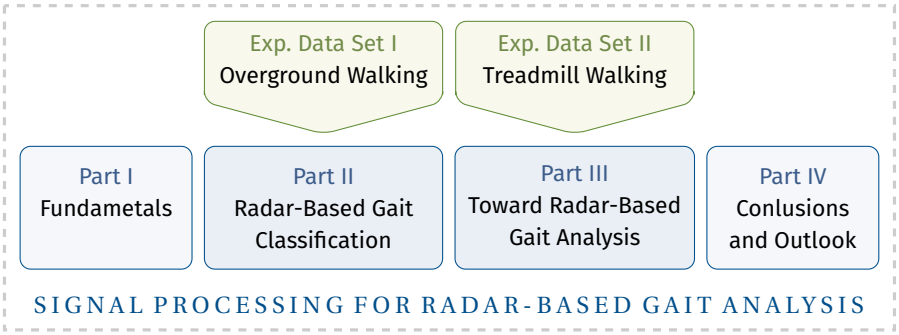

Figure 1.4: Overview of the thesis structure.

First, Part I provides the fundamentals of radar micro-Doppler signatures and briefly introduces basic gait analysis terminology.

Part II deals with radar-based gait classification and the presented methods are evaluated based on experimental radar data from overground walking. First, different radar data representations are introduced, namely, the spectrogram and the cadence-velocity diagram (CVD). To further the understanding of micro-Doppler signatures of human gait, a detailed biomechanical interpretation is given. Then, a classification framework for discriminating five different

walking styles based on radar backscatterings in presented, where different feature sets are used. Finally, a radar-based gait asymmetry detector is developed and evaluated based on realistic radar measurements of four individuals with diagnosed gait disorders.

Going beyond discriminating between a finite number of distinct gait classes, Part III focuses on assessing the capabilities of RF sensing for gait analysis. In this context, a variety of discrete biomechanical gait parameters as well as time-varying gait kinematics are extracted from experimental radar data from treadmill walking. The performance of the developed signal processing methods is assessed by the use of simultaneously recorded motion capture (MoCap) data utilizing ground reaction forces (GRFs).

Finally, a summary and conclusions of the presented work as well as an outlook for future research are given in Part IV.

1.4 PUBLICATIONS

The following publications have been produced during the period of doctoral candidacy:

BOOK CHAPTER:

[SAZ17b] A.-K. Seifert, M. G. Amin, and A. M. Zoubir, "Radar monitoring of humans with asistive walking devices," in *Radar for Indoor Monitoring: Detection, Classification, and Assessment*, M. G. Amin, Ed., Boca Raton, FL, USA: CRC Press, 2017, ch. 12, pp. 271–300.

INTERNATIONALLY REFEREED JOURNAL ARTICLES:

[SAZ19] A.-K. Seifert, M. G. Amin, and A. M. Zoubir, "Toward unobtrusive in-home gait analysis based on radar micro-Doppler signatures," *IEEE Transactions on Biomedical Engineering*, vol. 66, no. 9, pp. 2629–2640, Sep. 2019. DOI: 10.1109/TBME.2019.2893528.

[SGZ20] A.-K. Seifert, M. Grimmer, and A. M. Zoubir, "Doppler radar for the extraction of biomechanical parameters in gait analysis," *IEEE Journal of Biomedical and Health Informatics*, 2020, (to be published). DOI: 10.1109/JBHI.2020.2994471.

INTERNATIONALLY REFEREED CONFERENCE PAPERS:

[SAZ17a] A.-K. Seifert, M. G. Amin, and A. M. Zoubir, "New analysis of radar micro-Doppler gait signatures for rehabilitation and assisted living," in *IEEE International Conference on Acoustics, Speech and Signal Processing*, 2017. DOI: 10.1109/ICASSP.2017.7952908.

[SZA17] A.-K. Seifert, A. M. Zoubir, and M. G. Amin, "Radar-based human gait recognition in cane-assisted walks," in *IEEE Radar Conference*, 2017. DOI: 10.1109/RADAR.2017.7944431.

[SAZ18] A.-K. Seifert, M. G. Amin, and A. M. Zoubir, "Radar classification of human gait abnormality based on sum-of-harmonics analysis," in *IEEE Radar Conference*, 2018. DOI: 10.1109/RADAR.2018.8378687.

[SSAZ18] A.-K. Seifert, L. Schäfer, M. G. Amin, and A. M. Zoubir, "Subspace classification of human gait using radar micro-Doppler signatures," in *European Signal Processing Conference*, 2018. DOI: 10.23919/EUSIPCO.2018.8553592.

[TSM+18] F. K. Teklehaymanot, A.-K. Seifert, M. Muma, M. G. Amin, and A. M. Zoubir, "Bayesian target enumeration and labeling using radar data of human gait," in *European Signal Processing Conference*, 2018. DOI: 10.23919/EUSIPCO.2018.8553444.

[DSMZ19] L. Dawel, A.-K. Seifert, M. Muma, and A. M. Zoubir, "A robust genetic algorithm for feature selection and parameter optimization in radar-based gait analysis," in *IEEE International Workshop on Computational Advances in Multi-Sensor Adaptive Processing*, 2019. DOI: 10.1109/CAMSAP45676.2019.9022515.

[SZA19] A.-K. Seifert, A. M. Zoubir, and M. G. Amin, "Detection of gait asymmetry using indoor Doppler radar," in *IEEE Radar Conference*, (Best Student Paper Award, 1st prize), 2019. DOI: 10.1109/RADAR.2019.8835611.

[SRZA19] A.-K. Seifert, D. Reinhard, A. M. Zoubir, and M. G. Amin, "A robust and sequential approach for detecting gait asymmetry based on radar micro-Doppler signatures," in *European Signal Processing Conference*, 2019. DOI: 10.23919/EUSIPCO.2019.8902343.

WORKSHOP CONTRIBUTION:

[ZS17] A. M. Zoubir and A.-K. Seifert, "Signal processing and time-frequency analysis of radar data for indoor human monitoring," in *European Radar Conference*, Oct. 2017.

OTHER PUBLICATION:

[ZS18] A. M. Zoubir and A.-K. Seifert, "Radar for diagnosis, rehabilitation, and assisted living," *SciTech Europe Quarterly*, pp. 64–65, Dec. 2018.

REFERENCES

[AAKS17] S. Abdulatif *et al.*, "Real-time capable micro-Doppler signature decomposition of walking human limbs," in *IEEE Radar Conference*, 2017. DOI: 10.1109/RADAR.2017.7944367 (cit. on p. 7).

[AZS19] M. G. Amin, Z. Zeng, and T. Shan, "Hand gesture recognition based on radar micro-Doppler signature envelopes," in *IEEE Radar Conference*, 2019. DOI: 10.1109/RADAR.2019.8835661 (cit. on p. 5).

[AAZB15a] M. G. Amin *et al.*, "Human gait recognition with cane assistive device using quadratic time-frequency distributions," *IET Radar, Sonar and Navigation*, vol. 9, no. 9, pp. 1224–1230, Dec. 2015. DOI: 10.1049/iet-rsn.2015.0119 (cit. on p. 6).

[AZAH16] M. G. Amin *et al.*, "Radar signal processing for elderly fall detection: The future for in-home monitoring," *IEEE Signal Processing Magazine*, vol. 33, no. 2, pp. 71–80, Mar. 2016. DOI: 10.1109/MSP.2015.2502784 (cit. on p. 4).

[Ami17] M. G. Amin, Ed., *Radar for Indoor Monitoring: Detection, Classification, and Assessment*. Boca Raton, FL, USA: CRC Press, 2017 (cit. on p. 4).

[AAZB15b] M. G. Amin *et al.*, "Micro-Dppler characteristics of elderly gait patterns with walking aids," in *SPIE Defense and Security*, 2015. DOI: 10.1117/12.2178398 (cit. on p. 6).

[BCW11] A. Balleri, K. Chetty, and K. Woodbridge, "Classification of personnel targets by acoustic micro-Doppler signatures," *IET Radar, Sonar and Navigation*, vol. 5, no. 9, pp. 943–951, Dec. 2011. DOI: 10.1049/iet-rsn.2011.0087 (cit. on p. 3).

[BWH06] Y. Barak, R. C. Wagenaar, and K. G. Holt, "Gait characteristics of elderly people with a history of falls: A dynamic approach," *Physical Therapy*, vol. 86, no. 11, pp. 1501–1510, Nov. 2006. DOI: 10.2522/ptj.20050387 (cit. on p. 2).

[BPH15] S. Björklund, H. Petersson, and G. Hendeby, "Features for micro-Doppler based activity classification," *IET Radar, Sonar and Navigation*, vol. 9, no. 9, pp. 1181–1187, Dec. 2015. DOI: 10.1049/iet-rsn.2015.0084 (cit. on pp. 4, 6).

[BMB+16] S. Blackman *et al.*, "Ambient assisted living technologies for aging well: A scoping review," *Journal of Intelligent Systems*, vol. 25, no. 1, pp. 55–69, Jan. 2016. DOI: 10.1515/jisys-2014-0136 (cit. on p. 1).

[BTT90] R. Boulic, N. M. Thalmann, and D. Thalmann, "A global human walking model with real-time kinematic personification," *The Visual Computer*, vol. 6, no. 6, pp. 344–358, Nov. 1990. DOI: 10.1007/BF01901021 (cit. on pp. 7, 8).

[CHSW17] X. Cai *et al.*, "Single-camera-based method for step length symmetry measurement in unconstrained elderly home monitoring," *IEEE Transactions on Biomedical Engineering*, vol. 64, no. 11, pp. 2618–2627, Nov. 2017. DOI: 10.1109/TBME.2017.2653246 (cit. on p. 3).

[CW11] J. B. Campbell and R. H. Wynne, *Introduction to Remote Sensing*, 5th ed. New York, NY, USA: Guilford Publications, 2011 (cit. on pp. 2–4).

[CLLY16] S. Chen *et al.*, "Toward pervasive gait analysis with wearable sensors: A systematic review," *IEEE Journal of Biomedical and Health Informatics*, vol. 20, no. 6, pp. 1521–1537, Sep. 2016. DOI: 10.1109/JBHI.2016.2608720 (cit. on p. 2).

[Che08] V. C. Chen, "Doppler signatures of radar backscattering from objects with micro-motions," *IET Signal Processing*, vol. 2, no. 3, pp. 291–300, Sep. 2008. DOI: 10.1049/iet-spr:20070137 (cit. on p. 6).

[CLHW06] V. C. Chen *et al.*, "Micro-Doppler effect in radar: Phenomenon, model, and simulation study," *IEEE Transactions on Aerospace and Electronic Systems*, vol. 42, no. 1, pp. 2–21, Jan. 2006. DOI: 10.1109/TAES.2006.1603402 (cit. on p. 6).

[Che19] V. C. Chen, *The Micro-Doppler Effect in Radar*, 2nd ed. Norwood, MA, USA: Artech House, 2019 (cit. on pp. 4, 7).

[CLFG18] Z. Chen *et al.*, "Personnel recognition and gait classification based on multistatic micro-Doppler signatures using deep convolutional neural networks," *IEEE Geoscience and Remote Sensing Letters*, vol. 15, no. 5, pp. 669–673, May 2018. DOI: 10.1109/LGRS.2018.2806940 (cit. on pp. 5, 6).

[CB09] M. Cheney and B. Borden, *Fundamentals of radar imaging*. Philadelphia, PA, USA: Society for Industrial and Applied Mathematics, 2009 (cit. on p. 4).

[CPM+15] C. Clemente *et al.*, "A novel algorithm for radar classification based on Doppler characteristics exploiting orthogonal pseudo-Zernike polynomials," *IEEE Transactions on Aerospace and Electronic Systems*, vol. 51, no. 1, pp. 417–430, Jan. 2015. DOI: 10.1109/TAES.2014.130762 (cit. on p. 6).

[CLVS20] J. Clemente *et al.*, "Smart seismic sensing for indoor fall detection, location, and notification," *IEEE Journal of Biomedical and Health Informatics*, vol. 24, no. 2, pp. 524–532, Feb. 2020. DOI: 10.1109/JBHI.2019.2907498 (cit. on p. 3).

[CECS18] S. L. Colyer *et al.*, "A review of the evolution of vision-based motion analysis and the integration of advanced computer vision methods towards developing a markerless system," *Sports Medicine - Open*, vol. 4, no. 24, pp. 1–15, Jun. 2018. DOI: 10.1186/s40798-018-0139-y (cit. on p. 3).

[DBMS13] T. Damarla *et al.*, "Classification of animals and people ultrasonic signatures," *IEEE Sensors Journal*, vol. 13, no. 5, pp. 1464–1472, May 2013. DOI: 10.1109/JSEN.2012.2236550 (cit. on p. 3).

[DMS+16] C. Debes *et al.*, "Monitoring activities of daily living in smart homes: Understanding human behavior," *IEEE Signal Processing Magazine*, vol. 33, no. 2, pp. 81–94, Mar. 2016. DOI: 10.1109/MSP.2015.2503881 (cit. on pp. 2–4).

[DMP+17] E. Dolatabadi *et al.*, "Mixture-model clustering of pathological gait patterns," *IEEE Journal of Biomedical and Health Informatics*, vol. 21, no. 5, pp. 1297–1305, Nov. 2017. DOI: 10.1109/JBHI.2016.2633000 (cit. on p. 3).

[Ell16] S. Ellingson, *Radio Systems Engineering*. Cambridge, UK: Cambridge University Press, 2016 (cit. on p. 4).

[EG15] B. Erol and S. Z. Gürbüz, "A Kinect-based human micro-Doppler simulator," *IEEE Aerospace and Electronics Systems Magazine*, vol. 30, no. 5, pp. 6–17, May 2015. DOI: 10.1109/MAES.2015.7119820 (cit. on p. 3).

[EGA20] B. Erol, S. Z. Gürbüz, and M. G. Amin, "Motion classification using kinematically sifted ACGAN-synthesized radar micro-Doppler signatures," *IEEE Transactions on Aerospace and Electronic Systems*, 2020, to be pusblished. DOI: 10.1109/TAES.2020.2969579 (cit. on p. 4).

[EA19] B. Erol and M. G. Amin, "Radar data cube processing for human activity recognition using multisubspace learning," *IEEE Transactions on Aerospace and Electronic Systems*, vol. 55, no. 6, pp. 3617–3628, Apr. 2019. DOI: 10.1109/TAES.2019.2910980 (cit. on p. 4).

[ELB+17] B. M. Eskofier *et al.*, "An overview of smart shoes in the internet of health things: Gait and mobility assessment in health promotion and disease monitoring," *Applied Sciences*, vol. 7, no. 10, p. 986, Sep. 2017. DOI: 10.3390/app7100986 (cit. on p. 2).

[FLS19] F. Fioranelli, J. Le Kernec, and S. A. Shah, "Radar for health care: Recognizing human activities and monitoring vital signs," *IEEE Potentials*, vol. 38, no. 4, pp. 16–23, Jul. 2019. DOI: 10.1109/MPOT.2019.2906977 (cit. on p. 4).

[FRG15] F. Fioranelli, M. Ritchie, and H. Griffiths, "Aspect angle dependence and multistatic data fusion for micro-Doppler classification of armed/unarmed personnel," *IET Radar, Sonar and Navigation*, vol. 9, no. 9, pp. 1231–1239, Dec. 2015. DOI: 10.1049/iet-rsn.2015.0058 (cit. on p. 6).

[GMG01] J. L. Geisheimer, W. S. Marshall, and E. Greneker, "A continuous-wave (CW) radar for gait analysis," in *IEEE Asilomar Asilomar Conference on Signals, Systems, and Computers*, 2001. DOI: 10.1109/ACSSC.2001.987041 (cit. on p. 6).

[GTK+17] F. Gholami *et al.*, "A Microsoft Kinect-based point-of-care gait assessment framework for multiple sclerosis patients," *IEEE Journal of Biomedical and Health Informatics*, vol. 21, no. 5, pp. 1376–1385, Sep. 2017. DOI: 10.1109/JBHI.2016.2593692 (cit. on pp. 2, 3).

[GZA09] U. Givon, G. Zeilig, and A. Achiron, "Gait analysis in multiple sclerosis: Characterization of temporal–spatial parameters using GAITRite functional ambulation system," *Gait & Posture*, vol. 29, no. 1, pp. 138–142, Jan. 2009. DOI: 10.1016/j.gaitpost.2008.07.011 (cit. on p. 3).

[GRWS19] M. Grimmer *et al.*, "Mobility related physical and functional losses due to aging and disease - a motivation for lower limb exoskeletons," *Journal of NeuroEngineering and Rehabilitation*, vol. 16, no. 2, pp. 1–21, Jan. 2019. DOI: 10.1186/s12984-018-0458-8 (cit. on p. 2).

[GL17] C. Gu and J. Lien, "A two-tone radar sensor for concurrent detection of absolute distance and relative movement for gesture sensing," *IEEE Sensors Letters*, vol. 1, no. 3, pp. 1–4, Jun. 2017. DOI: 10.1109/LSENS.2017.2696520 (cit. on p. 5).

[GA19] S. Z. Gürbüz and M. G. Amin, "Radar-based human-motion recognition with deep learning: Promising applications for indoor monitoring," *IEEE Signal Processing Magazine*, vol. 36, no. 4, pp. 16–28, Jul. 2019. DOI: 10.1109/MSP.2018.2890128 (cit. on pp. 4, 5).

[GCBS17] S. Z. Gürbüz *et al.*, "Micro-Doppler-based in-home aided and unaided walking recognition with multiple radar and sonar systems," *IET Radar, Sonar and Navigation*, vol. 11, no. 1, pp. 107–115, Apr. 2017. DOI: 10.1049/iet-rsn.2016.0055 (cit. on pp. 3, 6).

[HAH+10] S. Hagler *et al.*, "Unobtrusive and ubiquitous in-home monitoring: A methodology for continuous assessment of gait velocity in elders," *IEEE Transactions on Biomedical Engineering*, vol. 57, no. 4, pp. 813–820, Apr. 2010. DOI: 10.1109/TBME.2009.2036732 (cit. on p. 2).

[HSK+18] P. Held *et al.*, "Radar-based analysis of pedestrian micro-Doppler signatures using motion capture sensors," in *IEEE Intelligent Vehicles Symposium*, 2018, pp. 787–793. DOI: 10.1109/IVS.2018.8500656 (cit. on p. 7).

[HGB+14] M. Hofmann *et al.*, "The TUM gait from audio, image and depth (GAID) database: Multimodal recognition of subjects and traits," *Journal of Visual Communication and Image Representation*, vol. 25, no. 1, pp. 195–206, Jan. 2014. DOI: 10.1016/j.jvcir.2013.02.006 (cit. on p. 2).

[HZG+18] H. Hong *et al.*, "Noncontact sleep stage estimation using a CW Doppler radar," *IEEE Journal on Emerging and Selected Topics in Circuits and Systems*, vol. 8, no. 2, pp. 260–270, Jun. 2018. DOI: 10.1109/JETCAS.2017.2789278 (cit. on p. 4).

[HD08] C. Hornsteiner and J. Detlefsen, "Characterisation of human gait using a continuous–wave radar at 24 GHz," *Advances in Radio Science*, vol. 6, pp. 67–70, May 2008. DOI: 10.5194/ars-6-67-2008 (cit. on p. 6).

[JPL+18] D. Jarchi *et al.*, "A review on accelerometry-based gait analysis and emerging clinical applications," *IEEE Reviews in Biomedical Engineering*, vol. 11, pp. 177–194, Feb. 2018. DOI: 10.1109/RBME.2018.2807182 (cit. on pp. 2, 7).

[JCM+18] H. Jiang *et al.*, "Smart home based on WiFi sensing: A survey," *IEEE Access*, vol. 6, pp. 13 317–13 325, Mar. 2018. DOI: 10.1109/ACCESS.2018.2812887 (cit. on p. 4).

[JA18] B. Jokanović and M. Amin, "Fall detection using deep learning in range-Doppler radars," *IEEE Transactions on Aerospace and Electronic Systems*, vol. 54, no. 1, pp. 180–189, Feb. 2018. DOI: 10.1109/TAES.2017.2740098 (cit. on p. 4).

[JAA16] B. Jokanović, M. Amin, and F. Ahmad, "Radar fall motion detection using deep learning," in *IEEE Radar Conference*, 2016. DOI: 10.1109/RADAR.2016.7485147 (cit. on p. 4).

[JAE17] B. Jokanović, M. Amin, and B. Erol, "Multiple joint-variable domains recognition of human motion," in *IEEE Radar Conference*, 2017. DOI: 10.1109/RADAR.2017.7944340 (cit. on p. 4).

[KR07] K. Kalgaonkar and B. Raj, "Acoustic Doppler sonar for gait recogination," in *IEEE International Conference on Advanced Video and Signal Based Surveillance*, 2007. DOI: 10.1109/AVSS.2007.4425281 (cit. on p. 3).

[KGG+15] C. Karabacak *et al.*, "Knowledge exploitation for human micro-Doppler classification," *IEEE Geoscience and Remote Sensing Letters*, vol. 12, no. 10, pp. 2125–2129, Oct. 2015. DOI: 10.1109/LGRS.2015.2452311 (cit. on p. 7).

[KMD+12] J. Kaye *et al.*, "One walk a year to 1000 within a year: Continuous in-home unobtrusive gait assessment of older adults," *Gait & Posture*, vol. 35, no. 2, pp. 197–202, Feb. 2012. DOI: 10.1016/j.gaitpost.2011.09.006 (cit. on p. 2).

[KM16] Y. Kim and T. Moon, "Human detection and activity classification based on micro-Doppler signatures using deep convolutional neural networks," *IEEE Geoscience and Remote Sensing Letters*, vol. 13, no. 1, pp. 8–12, Jan. 2016. DOI: 10.1109/LGRS.2015.2491329 (cit. on p. 5).

[KHK15] Y. Kim, S. Ha, and J. Kwon, "Human detection using Doppler radar based on physical characteristics of targets," *IEEE Geoscience and Remote Sensing Letters*, vol. 12, no. 2, pp. 289–293, Feb. 2015. DOI: 10.1109/LGRS.2014.2336231 (cit. on p. 5).

[KL09] Y. Kim and H. Ling, "Human activity classification based on micro-Doppler signatures using a support vector machine," *IEEE Transactions on Geoscience and Remote Sensing*, vol. 47, no. 5, pp. 1328–1337, May 2009. DOI: 10.1109/TGRS.2009.2012849 (cit. on p. 4).

[Kir06] C. Kirtley, *Clinical Gait Analysis: Theory and Practice*. London, UK: Churchill Livingstone, 2006 (cit. on p. 3).

[LCAL19] J. Latorre *et al.*, "Gait analysis with the Kinect v2: Normative study with healthy individuals and comprehensive study of its sensitivity, validity, and reliability in individuals with stroke," *Journal of NeuroEngineering and Rehabilitation*, vol. 16, no. 97, pp. 1–11, Jul. 2019. DOI: 10.1186/s12984-019-0568-y (cit. on p. 3).

[LFD+19] J. Le Kernec *et al.*, "Radar signal processing for sensing in assisted living: The challenges associated with real-time implementation of emerging algorithms," *IEEE Signal Processing Magazine*, vol. 36, no. 4, pp. 29–41, Jul. 2019. DOI: 10.1109/MSP.2019.2903715 (cit. on p. 4).

[LRW12] D. Levine, J. Richards, and M. Whittle, Eds., *Whittle's Gait Analysis*. London, UK: Churchill Livingstone, 2012 (cit. on p. 1).

[LPH+17] C. Li *et al.*, "A review on recent progress of portable short-range noncontact microwave radar systems," *IEEE Transactions on Microwave Theory and Technique*, vol. 65, no. 5, pp. 1692–1706, Jan. 2017 (cit. on p. 4).

[LPTB12] J. Li *et al.*, "Automatic classification of human motions using doppler radar," in *International Joint Conference on Neural Networks*, 2012. DOI: 10.1109/IJCNN.2012.6252625 (cit. on p. 6).

[LTP18] W. Li, B. Tan, and R. Piechocki, "Passive radar for opportunistic monitoring in e-health applications," *IEEE Journal of Translational Engineering in Health and Medicine*, vol. 6, pp. 1–10, Jan. 2018. DOI: 10.1109/JTEHM.2018.2791609 (cit. on p. 4).

[LZS+17] F. Lin *et al.*, "SleepSense: A noncontact and cost-effective sleep monitoring system," *IEEE Transactions on Biomedical Circuits and Systems*, vol. 11, no. 1, pp. 189–202, Feb. 2017. DOI: 10.1109/TBCAS.2016.2541680 (cit. on p. 4).

[LIA10] B. Lyonnet, C. Ioana, and M. G. Amin, "Human gait classification using micro-Doppler time-frequency signal representations," in *IEEE Radar Conference*, 2010. DOI: 10.1109/RADAR.2010.5494489 (cit. on p. 6).

[MPP+05] K. D. Marek *et al.*, "Clinical outcomes of aging in place," *Nursing Research*, vol. 54, no. 3, pp. 202–211, May 2005. DOI: 10.1097/00006199-200505000-00008 (cit. on p. 1).

[MSBE10] A. Mehmood *et al.*, "Extraction of the velocity of walking human's body segments using ultrasonic Doppler," *Journal of the Acoustical Society of America*, vol. 128, no. 5, EL316–EL322, Nov. 2010. DOI: 10.1121/1.3501115 (cit. on p. 3).

[MA09] B. G. Mobasseri and M. G. Amin, "A time-frequency classifier for human gait recognition," in *SPIE Defense, Security, and Sensing*, 2009. DOI: 10.1117/12.819060 (cit. on p. 6).

[MPGL17] J. Munoz-Ferreras *et al.*, "Review on advanced short-range multimode continuous-wave radar architectures for healthcare applications," *IEEE Journal of Electromagnetics, RF and Microwaves in Medicine and Biology*, vol. 1, no. 1, pp. 14–25, Jun. 2017. DOI: 10.1109/JERM.2017.2735241 (cit. on p. 4).

[MGM14] A. Muro-de-la-Herran, B. Garcia-Zapirain, and A. Mendez-Zorrilla, "Gait analysis methods: An overview of wearable and non-wearable systems, highlighting clinical applications," *Sensors*, vol. 14, no. 2, pp. 3362–3394, Feb. 2014. DOI: 10.3390/s140203362 (cit. on pp. 2, 3).

[OSA11] I. Orović, S. Stanković, and M. Amin, "A new approach for classification of human gait based on time-frequency feature representations," *Signal Processing*, vol. 91, no. 6, pp. 1448–1456, Jun. 2011. DOI: 10.1016/j.sigpro.2010.08.013 (cit. on p. 6).

[Ote05] M. Otero, "Application of a continuous wave radar for human gait recognition," in *SPIE Defense and Security*, 2005. DOI: 10.1117/12.607176 (cit. on p. 6).

[PWBN14] A. Pfister *et al.*, "Comparative abilities of Microsoft Kinect and Vicon 3D motion capture for gait analysis," *Journal of Medical Engineering & Technology*, vol. 38, no. 5, pp. 274–280, Jul. 2014. DOI: 10.3109/03091902.2014.909540 (cit. on p. 3).

[PK17] W. Pirker and R. Katzenschlager, "Gait disorders in adults and the elderly," *Wiener Klinische Wochenschrift*, vol. 129, no. 3-4, pp. 81–95, Oct. 2017. DOI: 10.1007/s00508-016-1096-4 (cit. on p. 2).

[RGC17] S. S. Ram, S. Z. Gürbüz, and V. C. Chen, "Modeling and simulation of human motions for micro-Doppler signatures," in *Radar for Indoor Monitoring: Detection, Classification, and Assessment*, M. G. Amin, Ed., Boca Raton, FL, USA: CRC Press, 2017, ch. 3, pp. 39–69 (cit. on p. 7).

[RAJ+16] R. Rana *et al.*, "Gait velocity estimation using time-interleaved between consecutive passive IR sensor activations," *IEEE Sensors Journal*, vol. 16, no. 16, pp. 6351–6358, Aug. 2016. DOI: 10.1109/JSEN.2016.2577708 (cit. on p. 2).

[RB15] R. Ricci and A. Balleri, "Recognition of humans based on radar micro-Doppler shape spectrum features," *IET Radar, Sonar and Navigation*, vol. 9, no. 9, pp. 1216–1223, Dec. 2015. DOI: 10.1049/iet-rsn.2014.0551 (cit. on pp. 5, 6).

[SUSM19] K. Saho *et al.*, "Using micro-Doppler radar to measure gait features associated with cognitive functions in elderly adults," *IEEE Access*, vol. 7, pp. 24 122–24 131, Feb. 2019. DOI: 10.1109/ACCESS.2019.2900303 (cit. on p. 7).

[SIT+16] T. Sakamoto *et al.*, "Feature-based correlation and topological similarity for interbeat interval estimation using ultrawideband radar," *IEEE Transactions on Biomedical Engineering*, vol. 63, no. 4, pp. 747–757, Apr. 2016. DOI: 10.1109/TBME.2015.2470077 (cit. on p. 4).

[SCC+19] M. Serrao *et al.*, "Prediction of responsiveness of gait variables to rehabilitation training in Parkinson's disease," *Frontiers in Neurology*, vol. 10, no. 826, pp. 1–12, Aug. 2019. DOI: 10.3389/fneur.2019.00826 (cit. on p. 7).

[SMF+17] G. Severini *et al.*, "Evaluation of clinical gait analysis parameters in patients affected by multiple sclerosis: Analysis of kinematics," *Clinical Biomechanics*, vol. 45, pp. 1–8, Jun. 2017. DOI: 10.1016/j.clinbiomech.2017.04.001 (cit. on p. 7).

[SÖG18] M. S. Seyfioğlu, A. M. Özbaygglu, and S. Z. Gürbüz, "Deep convolutional autoencoder for radar-based classification of similar aided and unaided human activities," *IEEE Transactions on Aerospace and Electronic Systems*, vol. 54, no. 4, pp. 1709–1723, Aug. 2018. DOI: 10.1109/TAES.2018.2799758 (cit. on pp. 4, 6).

[SF19] S. A. Shah and F. Fioranelli, "RF sensing technologies for assisted daily living in healthcare: A comprehensive review," *IEEE Aerospace and Electronics Systems Magazine*, vol. 34, no. 11, pp. 26–44, Nov. 2019. DOI: 10.1109/MAES.2019.2933971 (cit. on p. 4).

[Sim04] S. R. Simon, "Quantification of human motion: Gait analysis - benefits and limitations to its application to clinical problems," *Journal of Biomechanics*, vol. 37, no. 12, pp. 1869–1880, Dec. 2004. DOI: 10.1016/j.jbiomech.2004.02.047 (cit. on p. 2).

[SS13] E. E. Stone and M. Skubic, "Unobtrusive, continuous, in-home gait measurement using the Microsoft Kinect," *IEEE Transactions on Biomedical Engineering*, vol. 60, no. 10, pp. 2925–2932, Oct. 2013. DOI: 10.1109/TBME.2013.2266341 (cit. on p. 3).

[SHRS15] B. Y. Su *et al.*, "Doppler radar fall activity detection using the wavelet transform," *IEEE Transactions on Biomedical Engineering*, vol. 62, no. 3, pp. 865–875, Mar. 2015. DOI: 10.1109/TBME.2014.2367038 (cit. on p. 4).

[TS09] D. Tahmoush and J. Silvious, "Radar micro-Doppler for long range front-view gait recognition," in *IEEE International Conference on Biometrics: Theory Applications and Systems*, 2009. DOI: 10.1109/BTAS.2009.5339049 (cit. on p. 6).

[TLZF12] W. Tao *et al.*, "Gait analysis using wearable sensors," *Sensors*, vol. 12, no. 2, pp. 2255–2283, Feb. 2012. DOI: 10.3390/s120202255 (cit. on p. 2).

[TBA10] F. H. C. Tivive, A. Bouzerdoum, and M. G. Amin, "A human gait classification method based on radar Doppler spectrograms," *EURASIP Journal on Advances in Signal Processing*, vol. 2010, pp. 1–12, Jul. 2010 (cit. on p. 6).

[TPB15] F. H. C. Tivive, S. L. Phung, and A. Bouzerdoum, "Classification of micro-Doppler signatures of human motions using log-gabor filters," *IET Radar, Sonar and Navigation*, vol. 9, no. 9, pp. 1188–1195, Dec. 2015. DOI: 10.1049/iet-rsn.2015.0113 (cit. on p. 6).

[UBJ15] M. Umair Bin Altaf, T. Butko, and B. Juang, "Acoustic gaits: Gait analysis with footstep sounds," *IEEE Transactions on Biomedical Engineering*, vol. 62, no. 8, pp. 2001–2011, Aug. 2015. DOI: 10.1109/TBME.2015.2410142 (cit. on p. 2).

[Uni19a] United Nations, Department of Economic and Social Affairs, Population Division. (Aug. 2019). Probabilistic population projections rev. 1 based on the world population prospects 2019 rev. 1, [Online]. Available: http://population.un.org/wpp/ (cit. on p. 1).

[Uni19b] United Nations, Department of Economic and Social Affairs, Population Division. (Aug. 2019). World population prospects 2019 rev. 1, [Online]. Available: http://population.un.org/wpp/ (cit. on p. 1).

[vDG03] P. van Dorp and F. C. A. Groen, "Human walking estimation with radar," *IEE Proceedings Radar, Sonar and Navigation*, vol. 150, no. 5, pp. 356–365, Oct. 2003. DOI: 10.1049/ip-rsn:20030568 (cit. on p. 8).

[vDG08] P. van Dorp and F. C. A. Groen, "Feature-based human motion parameter estimation with radar," *IET Radar, Sonar and Navigation*, vol. 2, pp. 135–145, Apr. 2008. DOI: 10.1049/iet-rsn:20070086 (cit. on p. 8).

[VKJ+18] B. Vandersmissen *et al.*, "Indoor person identification using a low-power FMCW radar," *IEEE Transactions on Geoscience and Remote Sensing*, vol. 56, no. 7, pp. 3941–3952, Jul. 2018. DOI: 10.1109/TGRS.2018.2816812 (cit. on p. 5).

[WBH+15] F. Wahid *et al.*, "Classification of Parkinson's disease gait using spatial-temporal gait features," *IEEE Journal of Biomedical and Health Informatics*, vol. 19, no. 6, pp. 1794–1802, Nov. 2015. DOI: 10.1109/JBHI.2015.2450232 (cit. on pp. 2, 7).

[WSS+13] F. Wang *et al.*, "Toward a passive low-cost in-home gait assessment system for older adults," *IEEE Journal of Biomedical and Health Informatics*, vol. 17, no. 2, pp. 346–355, Mar. 2013. DOI: 10.1109/JBHI.2012.2233745 (cit. on p. 3).

[WSRC14] F. Wang *et al.*, "Quantitative gait measurement with pulse-Doppler radar for passive in-home gait assessment," *IEEE Transactions on Biomedical Engineering*, vol. 61, no. 9, pp. 2434–2443, Sep. 2014. DOI: 10.1109/TBME.2014.2319333 (cit. on pp. 4, 6, 7).

[WF11] Y. Wang and A. E. Fathy, "Micro-Doppler signatures for intelligent human gait recognition using a UWB impulse radar," in *IEEE Antennas and Propagation Society International Symposium*, 2011. DOI: 10.1109/APS.2011.5996925 (cit. on p. 6).

[Wor08] World Health Organization. (May 2008). Integrated health services - what and why? [Online]. Available: https://www.who.int/healthsystems/technical_brief_final.pdf (cit. on p. 1).

[Wor18] World Health Organization. (Feb. 2018). Ageing and health, [Online]. Available: https://www.who.int/news-room/fact-sheets/detail/ageing-and-health (cit. on p. 1).

[XMC+15] X. Xu *et al.*, "Accuracy of the Microsoft Kinect for measuring gait parameters during treadmill walking," *Gait & Posture*, vol. 42, no. 2, pp. 145–151, Jul. 2015. DOI: 10.1016/j.gaitpost.2015.05.002 (cit. on p. 3).

[XMS+10] Z. Xue *et al.*, "Infrared gait recognition based on wavelet transform and support vector machine," *Pattern Recognition*, vol. 43, no. 8, pp. 2904–2910, Mar. 2010. DOI: 10.1016/j.patcog.2010.03.011 (cit. on p. 3).

[YNC04] C. Yam, M. S. Nixon, and J. N. Carter, "Automated person recognition by walking and running via model-based approaches," *Pattern Recognition*, vol. 37, no. 5, pp. 1057–1072, May 2004. DOI: 10.1016/j.patcog.2003.09.012 (cit. on p. 8).

[ZAS20] Z. Zeng, M. G. Amin, and T. Shan, "Arm motion classification using time-series analysis of the spectrogram frequency envelopes," *Remote Sensing*, vol. 12, no. 3, p. 454, Feb. 2020. DOI: 10.3390/rs12030454 (cit. on p. 5).

[ZHM+18] H. Zhao *et al.*, "A noncontact breathing disorder recognition system using 2.4-GHz digital-IF Doppler radar," *IEEE Journal of Biomedical and Health Informatics*, vol. 23, no. 1, pp. 208–217, Jan. 2018. DOI: 10.1109/JBHI.2018.2817258 (cit. on p. 4).

Part I

FUNDAMENTALS

„Einerlei, welche Form die Theorie
der elektromagnetischen Prozesse auch annehmen sollte,
das Doppler-Prinzip wird in jedem Fall erhalten bleiben.“

— *Albert Einstein, 1906.*

2 RADAR MICRO-DOPPLER SIGNATURES

This chapter introduces the fundamental principles for radar-based micro-Doppler analysis. Section 2.1 gives the radar signal model for backscatterings of electromagnetic (EM) waves that are subject to the Doppler effect, while Section 2.2 introduces the spectrogram as a tool to represent micro-Doppler signatures in the joint time-frequency domain.

2.1 RADAR SIGNAL MODEL AND DOPPLER EFFECT

Due to the Doppler effect, moving targets induce a frequency shift in the backscattered radar signals. Considering a mono-static radar system that transmits a sinusoidal signal [Che19]

$$s_t(t) = \sin\left(2\pi f_c t\right) \tag{2.1}$$

with carrier frequency f_c, the received radar return signal from a moving target is an attenuated and phase-shifted version of the transmitted signal, i.e.,

$$s_r(t) = 2\rho \sin\left(2\pi f_c t - 2\pi f_c \tau(t)\right) = 2\rho \sin\left(2\pi f_c t + \phi(t)\right). \tag{2.2}$$

Here, ρ denotes the path loss, $\tau(t)$ is the time-varying delay of the EM wave at the receiver due to target's motion, and $\phi(t)$ is the induced phase shift due to the Doppler effect. After quadrature demodulation at the receiver, we obtain the baseband representation of the radar return signal s_r as

$$s(t) = \rho e^{-j2\pi f_c \tau(t)} = \rho e^{j\phi(t)}. \tag{2.3}$$

From the induced phase difference between the transmitted and received signal, the Doppler shift can be obtained as [Che19]

instantaneous frequency

$$f^{\mathrm{D}}(t) = \frac{1}{2\pi}\frac{\mathrm{d}\phi(t)}{\mathrm{d}t} = -f_c \frac{\mathrm{d}\tau(t)}{\mathrm{d}t}. \tag{2.4}$$

We note that Eq. (2.4) describes the instantaneous frequency (IF) as the derivative of the instantaneous phase of the signal. The concept of the IF is only valid for mono-component signals, but is generally not applicable to multi-component signals unless their components are decomposed first [Che19].

Assuming that the radial velocity of the target is small enough such that the motion of the target during the wave's traveling time can be neglected (*stop and go approximation*), we find $\tau(t) \approx 2r(t)/c_0$. Here, $r(t)$ is the distance of the target to the radar, and $c_0 \approx 3 \times 10^8$ m/s denotes the propagation speed of the EM wave in free space, i.e., the speed of light. Using Eq. (2.4) and $\frac{\mathrm{d}}{\mathrm{d}t}\tau(t) \approx 2v(t)/c_0$, the Doppler shift can be expressed as

Doppler shift

$$f^{\mathrm{D}}(t) \approx -f_c \frac{2v(t)}{c_0} = -\frac{2v(t)}{\lambda_c}, \quad \text{for } v \ll c_0. \tag{2.5}$$

Here, $\lambda_c = c_0/f_c$ is the wavelength of the EM wave, and $v(t)$ assumes positive values when the target is moving away from the radar system.

2.2 MICRO-DOPPLER SIGNATURES OF HUMAN GAIT

In the case of non-rigid targets, e.g., humans and animals, each moving part induces its own Doppler shift. Since these movements are generally much smaller compared to the overall motion of the target, they are referred to as micro motions [Che19]. These micro motions induce additional Doppler shifts to the back-scattered radar signal, which are referred to as micro-Doppler components. Thus, for non-rigid targets, the signal model in (2.3) changes to

$$s(t) = \sum_i \rho_i e^{j\phi_i(t)}, \tag{2.6}$$

where ρ_i and ϕ_i is the path loss and the observed phase shift of the ith scatter component, respectively. Thus, the radar return signal contains multiple time-varying Doppler shifted versions of the transmitted signal.

The human walk is periodic by nature, i.e., after taking two steps the course of motions is repeated, which constitutes a gait cycle [Che19]. Thus, one would expect the time-domain radar return signal from a walking person to be periodic with each gait cycle. As an example, the top plot in Fig. 2.1 shows the real part of $s(n)$ for a person walking toward the radar. In the following, $s(t)$ is assumed to be sampled at an interval of $\Delta t = 1/f_s$, such that $s(n) = s(t)|_{t=n\Delta t}$ for $n = 0, \ldots, N-1$, where f_s is the sampling frequency and $N \in \mathbb{N}$ is the total number of discrete time samples. Further, the mean of the radar return is removed to discard signal components of non-moving targets. From Fig. 2.1, it can be seen that the amplitude increases while the person is approaching the radar, but periodicities are not apparent. The periodicity information cannot be directly accessed in time-domain, because it is *hidden* in the phase of the receive signal as given by Eq. (2.6).

A classical tool to reveal periodicities in a signal is the Fourier transform (FT). However, the FT does not depict the local frequency behavior. The left bottom plot of Fig. 2.1 depicts the Doppler spectrum of the receive signal for a person walking toward the radar. While the maximum of the Doppler spectrum indicates the overall velocity of the body in this case, the time information is neglected. In fact the Doppler components are periodic with each gait cycle, i.e., we observe a sum of periodically frequency-modulated signals. As such, the FT is not the proper analysis tool for studying the IF of the time-dependent Doppler and micro-Doppler signal components.

The individual components and their energy distributions over time and frequency become visible when utilizing a joint time-frequency representation (TFR). The spectrogram, which is the energetic representation of the signal's short-time Fourier transform (STFT), is the most common TFR used for analyzing radar micro-Doppler signatures. For a discrete-time signal $s(n)$, the spectrogram is given by the squared magnitude of the STFT [OSB99]

spectrogram

$$\mathrm{S}(n,k) = \left| \sum_{m=0}^{K-1} w(m)s(n+m) \exp\left(-j2\pi \frac{mk}{K}\right) \right|^2, \tag{2.7}$$

for $n = 0, \ldots, N-1$, where M is the length of the smoothing window $w(\cdot)$, k is the discrete frequency index with $k = 0, \ldots, K-1$, and $M, K \in \mathbb{N}$. Typically, K is chosen larger than M to increase the granularity of the spectral estimate, which is also referred to as zero-padding. The choice of the window function trades off the time and frequency resolutions in the spectrogram. A longer window length will degrade the time resolution, as signal components with of short duration

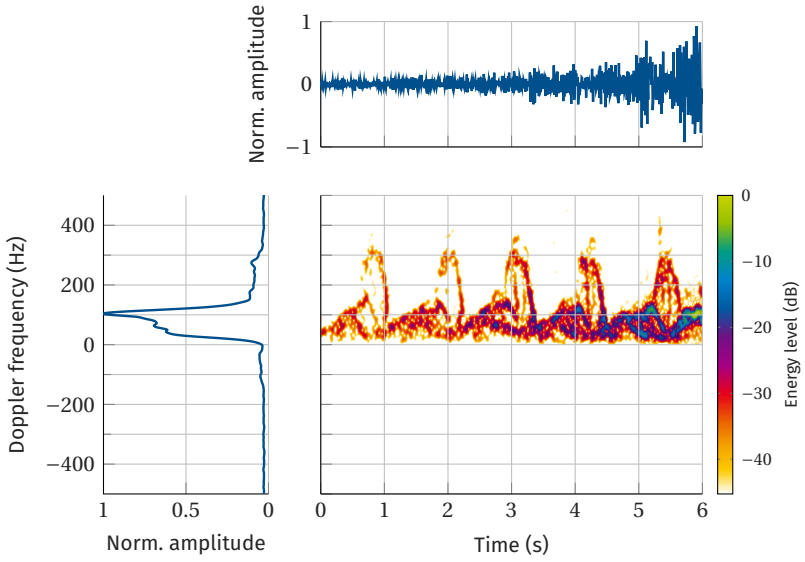

Figure 2.1: Example of micro-Doppler signatures of a person walking toward the radar system. They are revealed in the joint TFR (bottom right), while the time-domain signal (top) and the Doppler spectrum (bottom left) do not capture the time-dependent Doppler and micro-Doppler signal components.

cannot accurately be localized along the time axis. However, in the frequency domain, a smaller window length amounts to a convolution with a wideband signal, which limits the frequency resolution. Besides the spectrogram, other quadratic time-frequency distributions defined within Cohen's class [Coh89; Coh95] may be used.[1]

An example of a spectrogram of a person walking toward the radar is given in the right bottom plot of Fig. 2.1. Here, the TFR of the radar backscatterings depicts the main Doppler shift due to the torso's motion (between 0 Hz to 100 Hz) along with the micro-Doppler components due to swinging arms and legs. The swinging feet cause the highest Doppler shifts with up to 350 Hz) in this case, which relates to a radial velocity of 2.2 m/s. During the 6 s measurement the person took five steps. A detailed biomechanical interpretation of micro-Doppler gait signatures will be given in Section 5.1.1.

In the spectrogram in Fig. 2.1, the background noise has already been suppressed. Here, an adaptive thresholding technique is employed [KL09]. For each measurement, the noise level is estimated based on a Doppler frequency band without signal components. Then, the amplitudes in the spectrogram are lower bounded by this noise threshold. Details on the estimation of the noise threshold are given in Section A.1.1. In general, other noise removal techniques can be used, e.g., the eCLEAN algorithm [EA19; EGA20]. In the remainder of this thesis, unless stated otherwise, it is assumed that the noise in the spectrogam has been removed.

1 examples of high-resolution TFR of radar micro-Doppler signatures of human gait are given in, e.g., [SAZ17]

3

GAIT ANALYSIS

In this chapter basic gait terminology is introduced for describing biomechanical mechanisms during walking. Section 3.1 defines important gait cycle phases and events, which are the basis for gait analysis. In Section 3.2, the parameters describing the lower limb joint kinematics are outlined.

3.1 SPATIOTEMPORAL PARAMETERS

gait cycle

Due to its periodic nature, the human gait is typically analyzed in terms of a gait cycle [LRW12; Lip06]. The time interval between two successive occurrences of the same event during walking defines the gait cycle. Figure 3.1 illustrates a gait cycle with selected characteristic phases and events for the right leg. The left leg undergoes the same phases and events with an offset of half a gait cycle. Typically, the heel strike events of one foot are used to define a gait cycle. This is convenient since it coincides with the definition of a stride, which is defined from one heel strike to the next one of the same leg. Thus, one stride or two steps constitute a gait cycle.

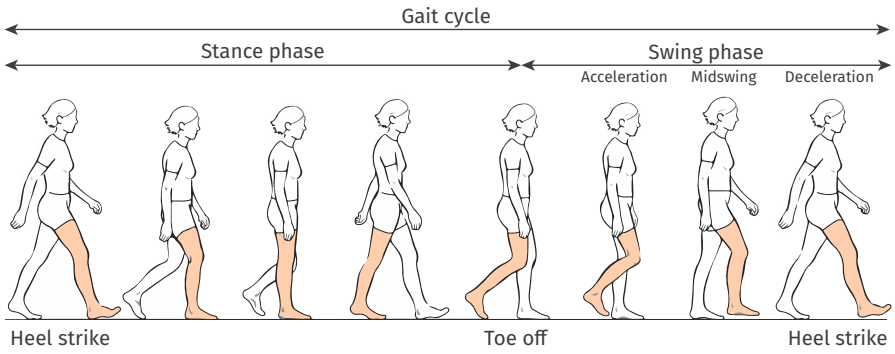

Figure 3.1: A gait cycle is composed of a stance and a swing phase. The swing phase is initiated by the toe-off event and terminated by the heel-strike event of the same leg, and compromises an acceleration, midswing and deceleration phase. (illustrations adapted from [Lip06], labels modified)

stance and flight time

A stride consists of a stance phase and a swing phase, whose durations are given by the stance and flight time, respectively [LRW12; Lip06]. During the stance phase the foot is on the ground, while the body is moved forward. The swing phase is characterized by the forward motion of the leg, which is initiated by the toe-off event and terminated by a heel-strike event, as indicated in Fig. 3.1. The stance phase accounts for approximately 60 % of the gait cycle, while the remainder is occupied by the swing phase. The latter can be further decomposed into three parts: the acceleration, where the foot is lifted from the ground and the leg's swing motion is initiated, the midswing, when the foot passes below the body with highest velocity, and the deceleration prior to the next heel strike [Lip06].

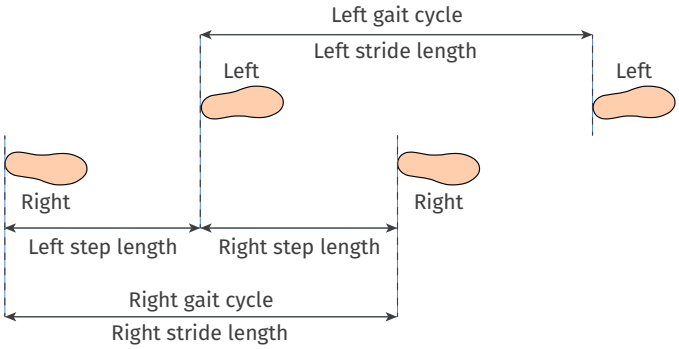

Figure 3.2: A right and left step constitute a stride, which defines the gait cycle. (illustrations adapted from [Lip06], labels modified)

stride and step length

The placement of the feet on the ground are described by the stride and step lengths [LRW12; Lip06]. As shown in Fig. 3.2, the stride length is defined as the distance from one heel strike to the next one of the same leg. It can be calculated from the product of walking speed and stride time. The stride length consists of the not necessarily equal step lengths of the left and right legs. The step length defines the distance that a leg moves forward in front of the other one, as indicated in Fig. 3.2.

cadence

The number of steps taken per minute is measured by the cadence [Lip06]. It typically depends on the walking speed: in slow walking the cadence can be as low as 70 steps per minute, while in fast walking the cadence can assume values around 130 steps per minute. A natural cadence is about 120 steps per minute, i.e., approximately one stride per second [Kir06]. In this thesis, we also utilize the term *cadence frequency* (in Hz), which is less common in clinical gait analysis but helpful for studying gait patterns. In this context, the cadence frequency is used more generally by quantifying the number of *movements* per second, e.g., number of steps per second.

3.2 KINEMATIC PARAMETERS

The study of kinematics involves the measurement of displacement, velocity, acceleration, and angles of (usually lower limbs) joints over time [KA12; Che19]. During walking, the lower body parts undergo translational as well as rotational motions simultaneously. In translational motions, any two points on the body move in the same direction, i.e., the connecting line keeps the same orientation. When rotating, all the points along a body part change their position around an axis of rotation. Thus, their linear velocities are generally not the same.

planar motion analysis

In this thesis, the gait motions are analyzed in a 2D space, namely, the sagittal plane. It is spanned by the y- and z-axis as depicted in Fig. 3.4. Hence, for the position, velocity, and acceleration of individual body parts, only the y- and z-components are considered. Figure 3.3 shows examples of respective trajectories for one individual walking at 1.1 m/s on a treadmill. Here, the solid lines indicate the mean obtained by averaging all strides in a 100 s measurement, and the shaded areas mark one standard deviation to each side of the mean. Individual strides were identified utilizing GRFs.[1] The displacement of the body parts is measured w.r.t. a reference coordinate system. In this case, the origin of this coordinate system was positioned approximately 0.6 m behind the test

1 details on the data collection are given in Chapter 9

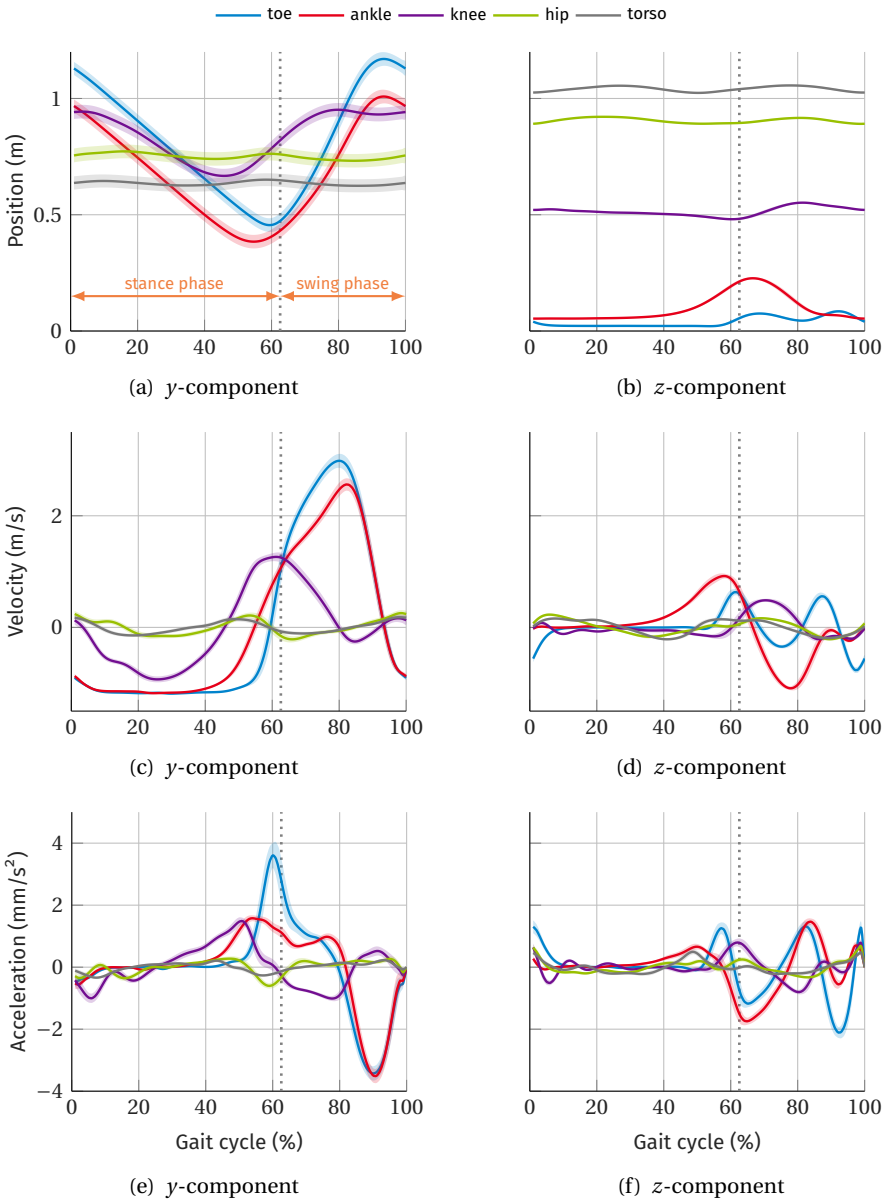

Figure 3.3: Examples of position, velocity, and acceleration trajectories for different body parts. Shaded areas indicate one standard deviation from the mean. The dotted lines separate the gait cycle phases, i.e., stance and swing phase (see Fig. 3.3a).

subject (compare torso position in Fig. 3.3a), and on the surface of the treadmill (compare toe position in Fig. 3.3b). The velocity trajectories are obtained by the derivative of the displacement w.r.t. time. Similarly, the accelerations are calculated by the time derivative of the respective velocity components.

Besides displacement, velocity, and acceleration, the lower limbs' angular kinematics are of interest for gait analysis. Here, the hip and knee angles are defined as shown in Fig. 3.4. The hip angle is measured w.r.t. the vertical axis, and assumes positive and negative values for flexion and extension of the hip joint, respectively. The knee angle is measure relative to the thigh rotation. Since the knee joint can only be flexed, the knee angle has negative values throughout the entire gait cycle.

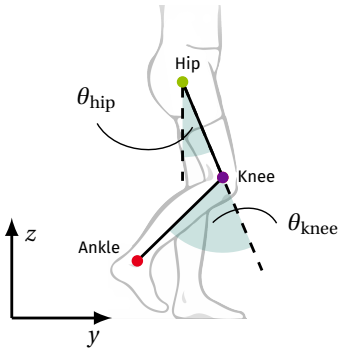

Figure 3.4: Definition of the hip and knee angles. The colored circles represent the markers for motion capturing of the hip (green), knee (purple), and ankle (red) joints. (illustration partly adapted from [Lip06], own labels)

Figure 3.5 shows examples of hip and knee angle trajectories obtained via marker-based motion capturing, where individual strides were identified utilizing GRFs.[1] The solid lines indicate the mean obtained by averaging all strides in a 100 s measurement, and the shaded areas mark one standard deviation to each side of the mean.

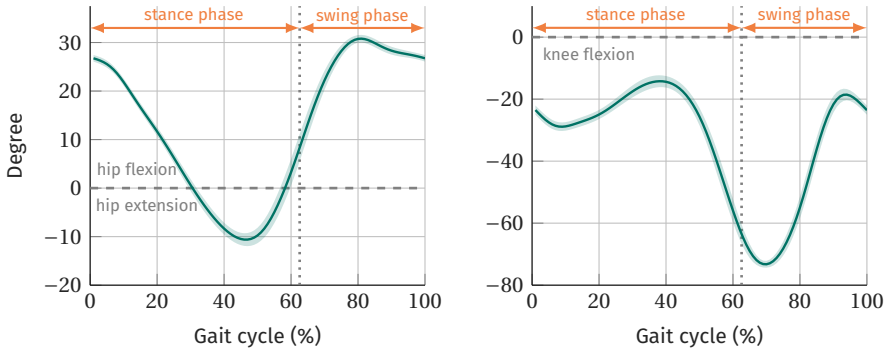

(a) hip angle

(b) knee angle

Figure 3.5: Examples of hip and knee angle trajectories during walking. While the hip joint can be flexed and extended (positive and negative angles), the knee joint can only be flexed (negative angles).

hip-knee cyclogram

A combined analysis of the hip and knee joint angles is provided by the so-called hip-knee cyclogram [Gos98; Che19]. It is obtained by plotting the hip angles vs. the knee angle for all time instants in a gait cycle, which results in an angle-angle diagram. Using the measurements shown in Fig. 3.5, an example of a hip-knee cyclogram is given in Fig. 3.6. In this thesis, only the hip-knee cyclogram is considered, and hereafter often referred to as cyclogram for short. However, for gait analysis also the knee-ankle cyclogram or the combined hip-knee-ankle cyclogram are employed [FSE+18; Gos98].

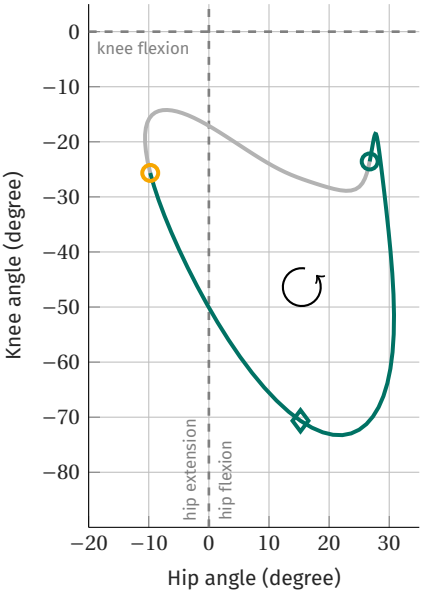

Figure 3.6: Example of a hip-knee cyclogram obtained by plotting the angle trajectories of Fig. 3.5 against each other for all time instants in the gait cycle. Circles mark heel-strike times of the right (turquoise) and left (yellow) leg. The latter marks the beginning of the right step. The diamond marks the toe-off time of the right leg, which initiates the swing phase.

REFERENCES

[Che19] V. C. Chen, *The Micro-Doppler Effect in Radar*, 2nd ed. Norwood, MA, USA: Artech House, 2019 (cit. on pp. 23, 24, 28, 30).

[Coh89] L. Cohen, "Time-frequency distributions – A review," *Proceedings of the IEEE*, vol. 77, no. 7, pp. 941–981, Jul. 1989. DOI: 10.1109/5.30749 (cit. on p. 25).

[Coh95] L. Cohen, *Time-frequency analysis*. Englewood Cliffs, NJ, USA: Prentice-Hall, 1995 (cit. on p. 25).

[EGA20] B. Erol, S. Z. Gürbüz, and M. G. Amin, "Motion classification using kinematically sifted ACGAN-synthesized radar micro-Doppler signatures," *IEEE Transactions on Aerospace and Electronic Systems*, 2020, to be pusblished. DOI: 10.1109/TAES.2020.2969579 (cit. on p. 25).

[EA19] B. Erol and M. G. Amin, "Radar data cube processing for human activity recognition using multisubspace learning," *IEEE Transactions on Aerospace and Electronic Systems*, vol. 55, no. 6, pp. 3617–3628, Apr. 2019. DOI: 10.1109/TAES.2019.2910980 (cit. on p. 25).

[FSE+18] L. Filli *et al.*, "Profiling walking dysfunction in multiple sclerosis: Characterisation, classification and progression over time," *Scientific Reports*, vol. 8, no. 1, pp. 1–13, Mar. 2018. DOI: 10.1038/s41598-018-22676-0 (cit. on p. 30).

[Gos98] A. Goswami, "A new gait parameterization technique by means of cyclogram moments: Application to human slope walking," *Gait & Posture*, vol. 8, no. 1, pp. 15–36, Aug. 1998. DOI: 10.1016/S0966-6362(98)00014-9 (cit. on p. 30).

[KA12] K. R. Kaufman and K.-N. An, in *Kelley's Textbook of Rheumatology*, G. S. Firestein *et al.*, Eds., 9th ed., Philadelphia, PA, USA: Elsevier Health Sciences, 2012, ch. Biomechanics, pp. 79–89 (cit. on p. 28).

[KL09] Y. Kim and H. Ling, "Human activity classification based on micro-Doppler signatures using a support vector machine," *IEEE Transactions on Geoscience and Remote Sensing*, vol. 47, no. 5, pp. 1328–1337, May 2009. DOI: 10.1109/TGRS.2009.2012849 (cit. on p. 25).

[Kir06] C. Kirtley, *Clinical Gait Analysis: Theory and Practice*. London, UK: Churchill Livingstone, 2006 (cit. on p. 28).

[LRW12] D. Levine, J. Richards, and M. Whittle, Eds., *Whittle's Gait Analysis*. London, UK: Churchill Livingstone, 2012 (cit. on pp. 27, 28).

[Lip06] L. Lippert, "Gait," in *Clinical Kinesiology and Anatomy*, 4th ed., Philadelphia, PA, USA: F. A. Davis, 2006, ch. 21 (cit. on pp. 27, 28, 30).

[OSB99] A. V. Oppenheim, R. W. Schafer, and J. R. Buck, *Discrete-Time Signal Processing*. Upper Saddle River, NJ, USA: Prentice-Hall, Inc., 1999 (cit. on p. 24).

[SAZ17] A.-K. Seifert, M. G. Amin, and A. M. Zoubir, "Radar monitoring of humans with asistive walking devices," in *Radar for Indoor Monitoring: Detection, Classification, and Assessment*, M. G. Amin, Ed., Boca Raton, FL, USA: CRC Press, 2017, ch. 12, pp. 271–300 (cit. on p. 25).

Part II

RADAR-BASED GAIT CLASSIFICATION

"Learning is more than absorbing facts,
it is acquiring understanding."

— *William A. Ward.*

4

SYSTEM DESCRIPTION AND DATA COLLECTION

All methods presented in this part of the thesis are based on the same data set presented in this chapter. Section 4.1 introduces the experimental setup for recording the radar data, and Section 4.2 outlines the subject information along with the experimental protocol.

The material presented in this chapter is partly taken from [SAZ19].

4.1 EXPERIMENTAL SETUP

Figure 4.1 shows a photo and a schematic of the experimental setup for data collection in an office environment at Technische Universität Darmstadt, Germany. The radar data were collected using a continuous-wave radar (SDRKIT 2400AD, Ancortek, Fairfax, VA, USA) [Anc20] with a transmitting frequency of 24 GHz. There were no absorbers on the walls for reducing multipath propagation of the electromagnetic (EM) waves. The horn antennas, one transmitting and one receiving, were placed at 1.15 m above the floor, which represents a nominal hip height. The radar system was positioned such that the test subjects walked in a 0° angle relative to the radar's line-of-sight (LOS).

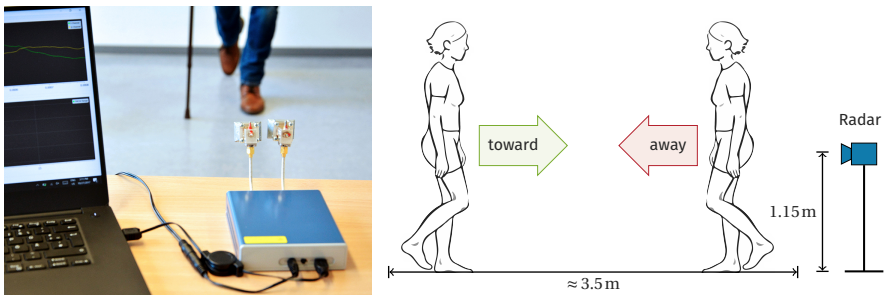

(a) (b)

Figure 4.1: Experimental setup for radar data collection, where a) shows the radar device and a laptop for recording the radar data of a walking person (at Technische Universität Darmstadt), and b) illustrates the geometry of the scene. (illustration of person adapted from [Lip06])

4.2 SUBJECT INFORMATION AND EXPERIMENTAL PROTOCOL

Ten volunteers (2 females and 8 males, aged 23.8 ± 2.6 years) were asked to walk slowly and without arm swinging toward and away from the radar system, between approximately 4.5 m and 1 m from the antenna feed point, as illustrated in Fig. 4.1b. There was only one person in front of the radar at a time. All participants provided informed consent prior to participation in the experiments. Five different walking styles are considered:

- normal walking (NW),
- limping with one leg (L1),

- limping with both legs (L2),
- walking with a cane in sync with one leg (CW),
- walking with a cane out of sync with any leg (CW/OOS).

Here, a limping leg is simulated by a knee that cannot be bent such that the stride motion is performed in a semicircular manner. In the case of limping with both legs neither of the knees can be bent. For each walking style, 10 measurements per subject and motion direction are considered, i.e., 100 measurements per person. In total, the data set contains 1000 measurements, where the number of samples per class and walking direction are equal among the test subjects.

Using the same experimental setup as described in Section 4.1, radar data of four additional subjects (all female) with different diagnosed gait disorders were collected in a semi-controlled lab environment at the Radar Imaging Lab at Villanova University, PA, USA (see Fig. 4.2). All volunteers provided written consent prior to participation in the experiments. The additional data set contains 13, 20, 28 (16 thereof with a cane in sync with one leg), and 26 measurements for person K, L, M, and N, respectively, i.e., 87 measurements in total.

As a result of a stroke at young age, Person K suffers from generalized dystonia affecting multiple muscle groups on one side of the body. Person L also experienced a stroke which caused a gait anomaly. Person M suffers from a Duchenne muscular dystrophy and experiences a relative weakness of the right side of the body. The fourth volunteer with gait abnormalities, Person N, has a congenital hip dislocation and suffers from a hip osteoarthritis on one body side due to it.

Figure 4.2: Experimental radar setup at the Radar Imaging Lab at Villanova University, PA, USA. Walls are covered with absorbers, though not optimized to absorb EM waves of 24 GHz. The radar system is positioned next to the camera and is not in the photo.

5 RADAR DATA REPRESENTATIONS

Gait characteristics manifest themselves differently depending on the data representation and the transforms adopted. In this chapter, different representations of radar data for analyzing micro-Doppler signatures are introduced. Section 5.1 focuses on the time-frequency representation (TFR) of the radar data, i.e., the spectogram, whereas Section 5.2 introduces another two-dimensional (2D) signal representation, the so-called cadence-velocity diagram (CVD). While the former depicts the Doppler and micro-Doppler signatures which correspond to velocities and their time-varying natures, the latter accentuates periodicities and better describes the harmonic components of the limbs.

The material presented in this chapter is partly taken from [SAZ17; SZA17; SAZ18; SAZ19].

5.1 SPECTROGRAM

For analyzing the highly non-stationary radar signals of human motions, the spectrogram as introduced in Section 2.2 is typically utilized. Based on the spectrogram, Section 5.1.1 gives a detailed biomechanical interpretation of micro-Doppler gait signatures, and elaborates on the differences when the radar has a front view on the target compared to monitoring the gait from behind. In Section 5.1.2, we introduce signals that can be derived from the spectrogram to be used for feature extractions.

5.1.1 *Biomechanical Interpretation*

Based on the spectrogram, this section gives a detailed biomechanical interpretation of micro-Doppler gait signatures. First, we analyze the differences in micro-Doppler signatures that appear when monitoring the gait from the front compared to from behind the subject. Figure 5.1a shows a typical spectrogram of a person walking toward the radar system. The micro-Doppler signatures of the feet show a sinusoidal shape, representing five steps here. Note that the walk is rather slow, mimicking an elderly person, and there is no arm swinging involved. In contrast, a typical signature of a person walking away from the radar is shown in Fig. 5.1b. Clearly, the micro-Doppler signatures of the steps are different compared to the toward-radar measurement. This difference has been overlooked in other works and has not been reported in any experimental or simulated micro-Doppler signatures.

To gain insights on the above differences, Fig. 5.1c shows an excerpt of the spectrogram in Fig. 5.1b corresponding to the step time of one leg during the gait cycle. It contains the swing phase consists of an acceleration, midswing and deceleration phase (see Fig. 3.1). In the acceleration phase, marked with (I) in Fig. 5.1c, the heel comes off the ground and the upper leg swings forward. As the latter is considered a pendulum-like motion, it reveals a sinusoidal-shaped micro-Doppler signature in the spectrogram, which can be seen between 0.2 s and 0.5 s with a maximum Doppler frequency of 200 Hz. In the mid-swing

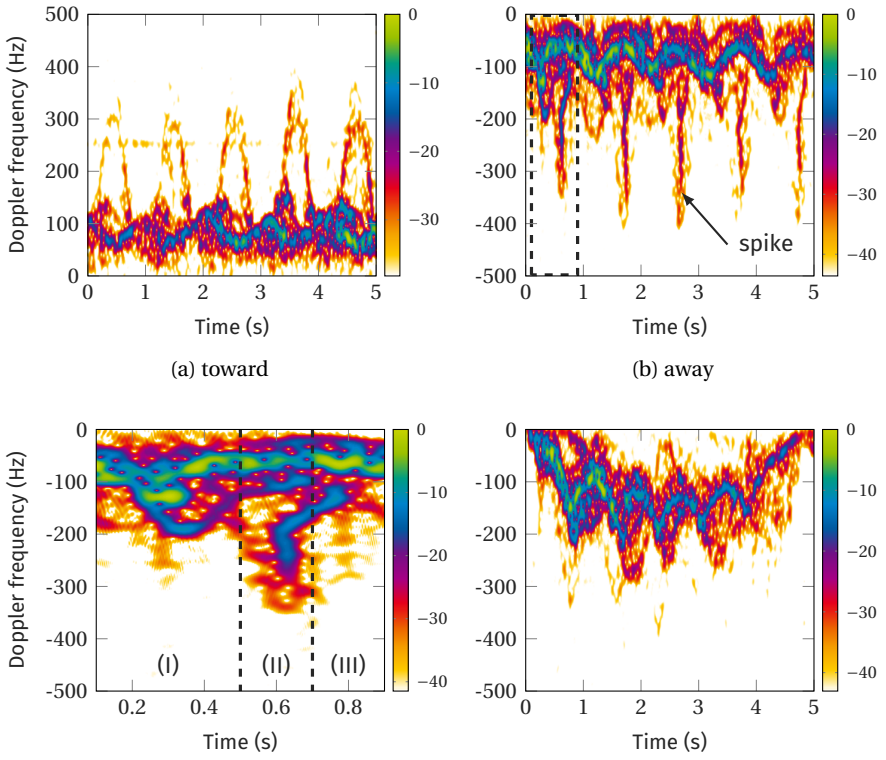

(a) toward (b) away

(c) micro-Doppler step signature (from (b)) (d) away (with absorbers on lower legs)

Figure 5.1: Spectrograms of the same person walking slowly (a) toward and (b) away from the radar system. (c) Extracted micro-Doppler signature from the spectrogram in (b) that corresponds to one step and shows a spike. (d) Spectrogram of a person walking away from radar while absorbers cover the lower legs, which is why the spike signatures are missing. The color indicates the received energy level in dB.

phase, (II), the swinging of the foot causes the highest Doppler frequency, i.e., it has the highest velocity, here up to 350 Hz between 0.5 s and 0.7 s. Again, due to its pendulum-like motion the micro-Doppler signature has a sinusoidal shape. Embraced in the foot signature, the lower leg signature becomes visible in the form of a spike, i.e., an impulse-like behavior in the time-frequency domain at 0.6 s. Accordingly, there are two dominant signatures that constitute the lower leg's micro-Doppler signature when the radar is facing the back of the human. However, due to the larger cross-section area in comparison to the foot, the calf reveals a higher energy in the time-frequency representation and is eclipsing the foot signature. The spike appears during the mid-swing phase when the swinging foot causes the highest Doppler shift corresponding to its highest velocity. Progressing in time, the spike passes into a half sinusoidal-shaped micro-Doppler signature, see between 0.6 s and 0.8 s. This phase represents the straight leg swinging to the front of the body during the deceleration phase, (III). This part of the signature is attributed to the reflections from the upper calf. It experiences the same deceleration as the foot, for which reason the signature is in parallel with the foot's signature. However, the calf's motion leads to a smaller Doppler frequency as the swinging angle with respect to the knee joint is smaller compared to that of the foot.

In order to support the previous observations we conducted an experiment where a person was walking away from the radar, while the lower legs up to the knee area were covered by absorbers. The resulting micro-Doppler signature is shown in Fig. 5.1d. Obviously, the characteristic spike signatures are absent, underscoring the fact that they are due to EM wave reflections from the lower legs. The spectrogram reveals the torso's motion, which can be identified by the maximum power, as well as the micro-Doppler signature of the upper legs. The latter appears shortly after the maximum torso Doppler frequency and is typically of sinusoidal shape due to its pendulum-like motion.

To study the contribution of individual body parts to the overall micro-Doppler gait signature, it is inevitable to resort to simulations based on mathematical or empirical models. A widely used empirically developed model to generate micro-Doppler gait signatures is the global human walking model by Boulic, Magnenat-Thalman and Thalman [BTT90]. The signatures are generated by utilizing a global human walk model describing the position and orientation of 12 human body parts. A simulated micro-Doppler signature of a human walking away from the radar is shown in Fig. 5.2, using the implementation given in [Che19]. We observe that it is fundamentally different from that of a real measurement as shown in Fig. 5.1b. In particular, the simulated micro-Doppler step signatures do not show the impulsive-like signature of the lower leg, i.e., the spike signature.

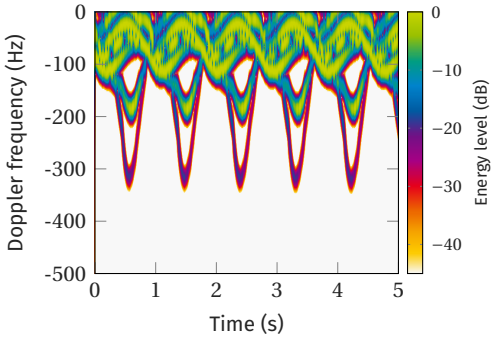

Figure 5.2: Simulated micro-Doppler signature of a person walking away from the radar system using the global human walking model by Boulic *et al.* [BTT90].

Next, we show examples of micro-Doppler signatures of different walking styles, which were recorded according to the experimental protocol outlined in Section 4.1. The resulting spectrograms for the analyzed gaits and directions relative to the radar system are shown in Figs. 5.3 and 5.4.

NORMAL WALK (NW) The micro-Doppler signatures of a person walking normally toward and away from the radar system are shown in Figs. 5.3a and 5.4a, respectively. In the spectrogram, the torso's motion can be identified by the highest energy due to its large radar cross section (RCS) and consequently strongest reflections. The torso's Doppler frequency periodically varies between approximately 30 Hz and 100 Hz, representing the acceleration and deceleration phases during the human walking cycle [Che19]. Here, the highest Doppler shift is observed in the double support phases, i.e., when both feet are in contact with the ground. In Fig. 5.3a, the time-frequency signature of the swinging foot shows a clear sinusoidal shape with up to about 370 Hz Doppler shift. Here, the spectrogram reveals six step signatures during the 6 s measurement. The micro-Doppler signature of a person walking away from the radar system is shown in Fig. 5.4a. Again, we observe six steps in the 6 s measurement. However, as discussed before, the micro-Doppler step signatures are

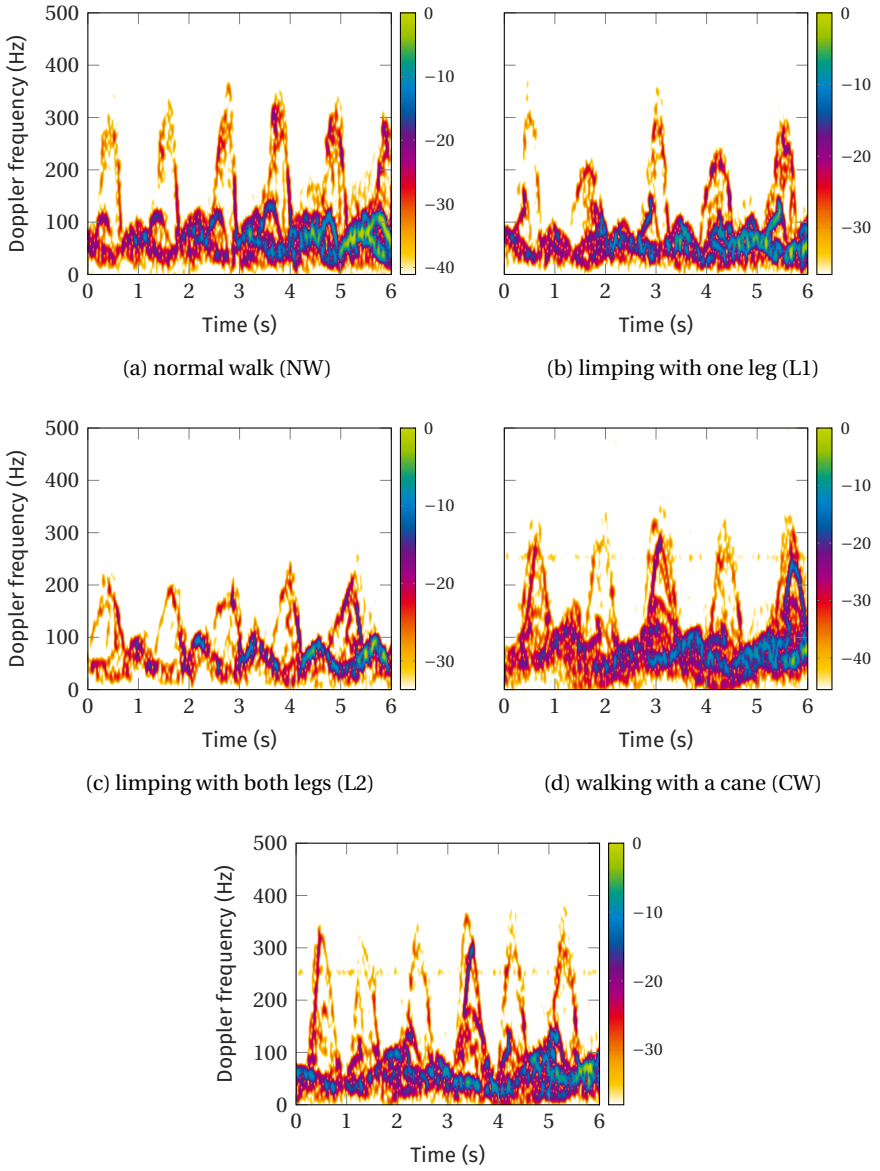

(a) normal walk (NW)

(b) limping with one leg (L1)

(c) limping with both legs (L2)

(d) walking with a cane (CW)

(e) walking with a cane out of sync (CW/oos)

Figure 5.3: Examples of spectrograms for different walking styles toward the radar system. The color indicates the energy level in dB.

clearly different compared to the toward-radar measurement and reveal the characteristic spike signature.

LIMPING WITH ONE LEG (L1) Figures 5.3b and 5.4b show the spectrograms of individuals limping toward and away from the radar system, respectively. Here, limping was simulated by the inability to bend one of the knees properly. Thus, every other step signature in Figs. 5.3b and 5.4b is different from that of a normal step. That is, in the toward-radar case, the second and fourth micro-Doppler step signatures are due to a limping leg, where in the away-from-radar measurement additionally the sixth step signature is abnormal. For both measurements, we observe that the abnormal step signatures have a smaller maximum Doppler shift (up to 250 Hz) compared to a normal step

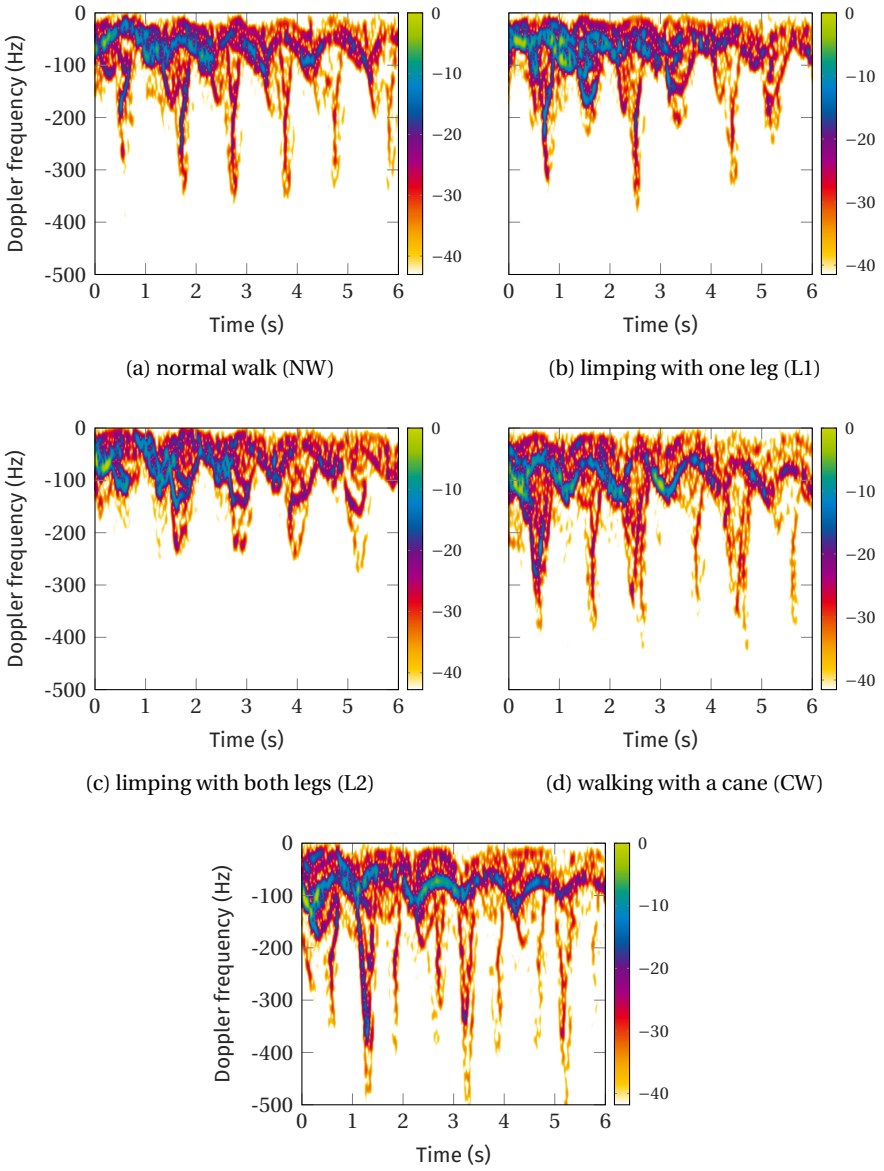

(a) normal walk (NW)

(b) limping with one leg (L1)

(c) limping with both legs (L2)

(d) walking with a cane (CW)

(e) walking with a cane out of sync (CW/oos)

Figure 5.4: Examples of spectrograms for different walking styles away from the radar system. The color indicates the energy level in dB.

signature (larger than 300 Hz). Further, due to the straight leg's swinging, the micro-Doppler stride signature has a sinusoidal shape. This is particularly recognizable when the radar has a back-view on the person, because the salient spiky characteristic of a normal step is absent (compare first and second step signatures in Fig. 5.4b).

LIMPING WITH BOTH LEGS (L2) Accordingly, when both legs cannot be fully bent during walking, each micro-Doppler step signature appears abnormal, as shown in Figs. 5.3c and 5.4c. As such the gait is periodic like a normal walk; also referred to as a symmetric gait. However, for this gait, the maximal observed Doppler shift is significantly lower than for normal walking. For away-

from-radar motions, we again observe the lack of the spike signature, which would indicate a normally swinging leg.

WALKING WITH A CANE (CW) The influence of using a cane on the micro-Doppler gait signatures is shown in Figs. 5.3d and 5.4d for walking toward and away from radar motions, respectively. In each case, the first, third and fifth step signatures are altered by the cane's micro-Doppler shifts, i.e., the leg's and the cane's micro-Doppler signatures are overlaying. Consequently, the energy of these micro-Doppler signatures are higher compared to those of normal strides. In case the radar has a back-view on the person, the spike signature is eclipsed by the overlaying cane signature. However, due the comparably smaller RCS of the cane, the spike is still visible in each step signature.

WALKING WITH A CANE - OUT OF SYNC (CW/OOS) In order to obtain isolated micro-Doppler signatures of a swinging cane, Figs. 5.3e and 5.4e show the spectrograms of a person walking with a cane, where the cane is moved independently of both legs. The resulting micro-Doppler signature pattern consists of an isolated cane signature followed by two step signatures. This pattern is repeated twice during the measurement shown in Fig. 5.3e. The away-from-radar measurement in Fig. 5.4e reveals the cane's signature at second, fifth and eighth position. Here, the cane's movement also exhibits a higher Doppler shift compared to the normal stride signatures. This is typically observed whenever the cane is actually used in order to relieve pressure on one of the legs. In so doing, the cane is moved faster, which results in a higher Doppler shift.

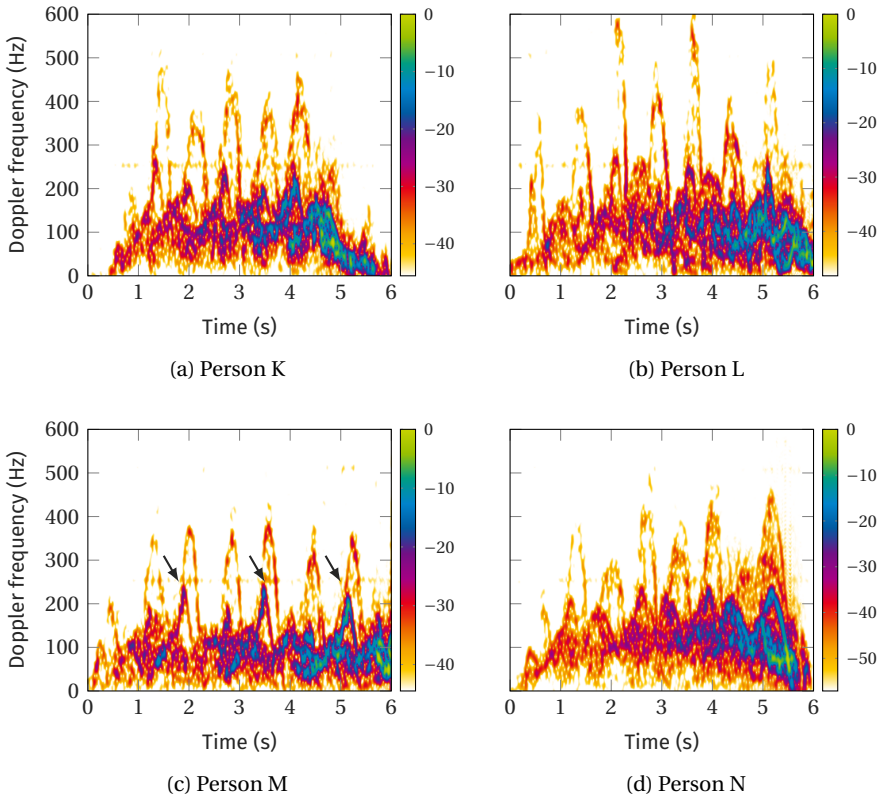

(a) Person K (b) Person L

(c) Person M (d) Person N

Figure 5.5: Example micro-Doppler signatures of individuals with diagnosed gait disorders walking toward the radar. The color indicates the energy level in dB.

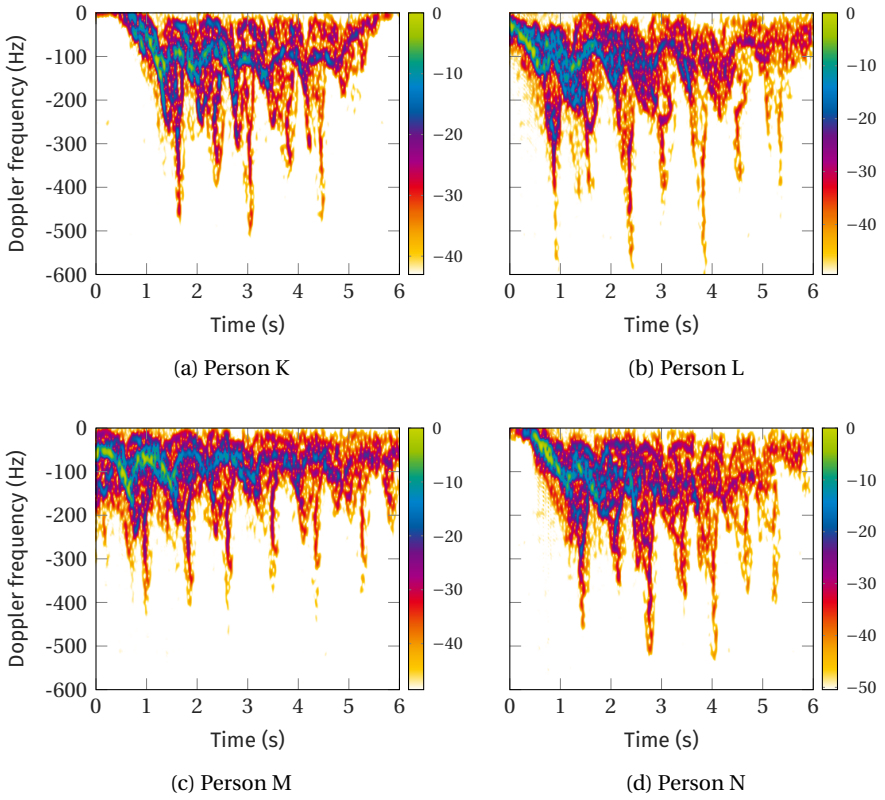

(a) Person K (b) Person L

(c) Person M (d) Person N

Figure 5.6: Example micro-Doppler signatures of individuals with diagnosed gait disorders walking away from the radar. The color indicates the energy level in dB.

CLINICAL DATA To underscore the relevance of the acquired radar data, we also conducted experiments for radar data acquisition involving four test subjects with diagnosed gait disorders due to different medical conditions as described in Section 4.2. Examples of spectrograms for these subjects are shown in Figs. 5.5 and 5.6 for toward and away from radar motions, respectively.

The micro-Doppler signatures in Fig. 5.5 expose the asymmetry in the gait, since every other micro-Doppler step signature is different. Typically, one of the swinging legs reveals a lower Doppler shift, meaning it swings with a lower radial velocity. This behavior can result from a decreased stance phase for one leg, e.g., in an attempt to keep the load to a minimum, which is compensated by a longer swing phase. This behavior is the same as for the simulated abnormal walking in Fig. 5.3b. However, in the case of Person M the gait asymmetry reveals itself in the knee's motions (see arrows in Fig. 5.5c), rather than in varying maximal Doppler shifts of the feet. This indicates that different gait disorders lead to distinct radar micro-Doppler signatures.

Examples of micro-Doppler signatures of the four individuals with diagnosed gait disorders walking away from the radar are shown in Fig. 5.6. As for the toward-radar motions, the gait asymmetry of Persons K, L, and N is clearly observable from the micro-Doppler signatures due to the alternating maximal Doppler shift per leg. However, as can be seen in Fig. 5.6c, identifying the gait asymmetry of Person M from behind is particularly challenging, since the maximal Doppler shift of both legs is approximately the same.

Figure 5.7 shows a spectrogram of Person M walking with a cane toward the radar system, where the cane's signatures is overlapping with every other

stride signature. Here, the second and fourth micro-Doppler step signatures are intensified by the cane's signature. A correct usage of the cane implies, that the cane's micro-Doppler signatures overlay those of the injured or weakened leg. However, the characteristic knee signatures of Person M remain visible (see arrows in Fig. 5.7).

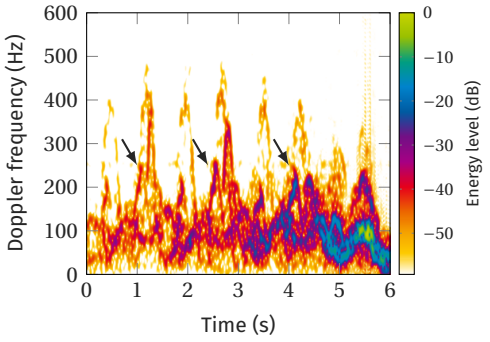

Figure 5.7: Example micro-Doppler signature of Person M walking with a cane toward the radar system.

5.1.2 *Signals Derived From the Spectrogram*

From the spectrogram, two other signals can be found: the envelope signal of the micro-Doppler signatures and the short-time energy signal of the radar return. Both signals are obtained from the noise-reduced spectrogram as described in Section A.1.1.

For the calculation of the spectrogram based on Eq. (2.7), a Hamming window of length $M = 256$ is used with an overlap of 255 samples, and zero-padding is applied to obtain $K = 2048$ discrete frequency points. The radar data are recorded at a sampling frequency of 12.8 kHz and sub-sampled to 2.56 kHz prior to the calculation of the spectrogram. Thus, we obtain a frequency resolution of 40 Hz and a time resolution of 0.1 s.

micro-Doppler envelope signal

To extract the micro-Doppler envelope signal, a series of morphological operations are applied to the spectrogram. First, the spectrogram, as given by Eq. (2.7), is converted to a binary image, where values below the estimated noise threshold are set to zero. Next, the binary image is dilated using a rectangular structuring element of size 16×32, where 16 pixels correspond to approximately 20 Hz along the Doppler frequency axis and 32 pixels represent 12.5 ms along the time axis. After filling holes in the resulting image, unconnected components with less than 40 000 pixels are removed. Finally, the image is eroded twice using a diamond-shaped structuring element with an extension of 8 pixels in each dimension and afterwards unconnected components with less than 500 pixels are removed. Using this image, the first index where signal energy occurs is stored for each time instant, which results in the micro-Doppler envelope signal as shown in Fig. 5.8 by the solid black line. One can see that while the signatures from the leg's or cane's motion are detected, unconnected noise components are ignored. Thus, the micro-Doppler envelope signal captures the varying maximal Doppler shifts throughout a gait cycle, irrespective of whether it corresponds to, e.g., a leg or a cane motion.

short-time energy signal

In contrast, the short-time energy signal accounts for the inherent pattern of individual micro-Doppler signatures by summing over K' Doppler bins in the spectrogram as

$$E(n) = \frac{1}{K'} \sum_{k=0}^{K'-1} \mathrm{S}(n,k), \quad n = 0,\ldots,N-1, \tag{5.1}$$

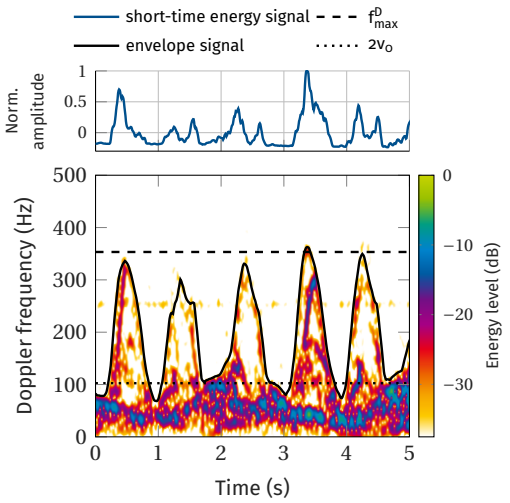

Figure 5.8: Micro-Doppler envelope signal, overlaid on the spectrogram (bottom), and short-time energy signal obtained from the spectrogram (top).

where S is the noise-reduced spectrogram, and $K' < K$ is the number of relevant frequency bins corresponding to micro-Doppler shifts excluding the torso's signature. Thus, the TFR is converted into a train of pulses along the time variable as indicated in Fig. 5.8. In this example, the relevant frequency bins were chosen such that they account for the Doppler components between twice the base velocity v_0 (dotted black line in Fig. 5.8) and the maximal Doppler shift of the measurement $f^{\mathrm{D}}_{\max}$ (dashed black line in Fig. 5.8).[1] The resulting energy signal reveals the difference in reflected energy over time for the cane's motion (between 0 s and 1 s and 3 s and 4 s) and a leg's motion (e.g. between 1 s and 2 s and 2 s and 3 s).

5.2 CADENCE-VELOCITY DIAGRAM

Since the spectrogram is a windowed Fourier transform (FT), a periodic signal will remain periodic in its TFR, with each frequency component exhibiting the same periodicity. Therefore, the periodic structure of the cyclic motion articulations of human gait persist in the time-frequency domain, with a sparser and higher power concentration compared to the time-domain description of the signals. With this property, by taking the FT along the time variable for each frequency bin in the spectrogram, we can assess how often certain Doppler shifts appear over time. The result is known as the cadence-velocity diagram (CVD) [CPM+15; BPH15; RB15; Ote05], where velocity is proportional to the observed Doppler shifts. For a normal gait, the fundamental frequency in the CVD represents the stride rate or cadence.

The CVD is obtained by taking the FT of the spectrogram along each Doppler frequency bin as [CPM+15]

cadence-velocity diagram

$$\mathrm{C}(\epsilon, k) = \left| \sum_{n=0}^{N-1} \mathrm{S}(n, k) \exp\left(-j2\pi \frac{n\epsilon}{L}\right) \right|, \tag{5.2}$$

where $\epsilon = 0, \cdots, L-1$ is the cadence frequency, S is the noise-reduced spectrogram, and $L \in \mathbb{N}$. Here, the velocity is directly proportional to the observed Doppler frequency as given by Eq. (2.5). Note that, in contrast to TFRs, the CVD does not depend on the initial phase of the gait cycle, i.e., it is a time-invariant analysis method.

1 The estimation of v_0 and $f^{\mathrm{D}}_{\max}$ will be explained in Section 6.1.

5.2.1 *Signals Derived From the Cadence-Velocity Diagram*

From the CVD, the mean cadence spectrum (MCS) can be obtained. It depicts how often certain Doppler components appear throughout a gait, independent of the components' velocities. The MCS is calculated by summing over all Doppler frequencies in the CVD, i.e., [BPH15; RB15]

mean cadence spectrum

$$\bar{\zeta}(\epsilon) = \frac{1}{K}\sum_{k=0}^{K-1} \mathrm{C}(\epsilon, k), \quad \epsilon = 0, \ldots, L-1. \tag{5.3}$$

The highest peak of the MCS typically represents the stride rate. For example, Fig. 5.9a reveals a stride rate of 0.9 Hz, which is consistent with almost six strides in the 6 s, data measurement (see Fig. 5.3a). The stride rate is an important characteristic of a walk and belongs to the group of physical features, which are easily interpretable. Note that, in medical terminology of gait analysis, the cadence is defined as the number of steps per unit time, and thus serves as a measure of the step rate. Here, however, we draw a distinction between the cadence frequency, as a measure of the periodicity of micro-Doppler signatures, and the stride rate, which describes the number of strides per second. Therefore, the repetition frequency of micro-Doppler signatures, hereafter, is referred to as f_{mD}, which does not necessarily relate to the stride rate in assisted or pathological gait. This will become clear from the examples presented later in this section.

mean Doppler spectrum

Similarly, we can find the mean Doppler spectrum by summing over all cadence frequencies for each Doppler frequency bin in the CVD, i.e.,

$$\bar{\Gamma}(k) = \frac{1}{L}\sum_{\epsilon=0}^{L-1} \mathrm{C}(\epsilon, k), \quad k = 0, \ldots, K-1. \tag{5.4}$$

From the mean Doppler spectrum, features such as the average walking speed of a person v_0, or the maximal Doppler shift $f^{\mathrm{D}}_{\mathrm{max}}$, can be extracted [RB15; BJP12]. Details on the extraction of these features will be given in Section 6.1.1.

Figures 5.9 and 5.10 show the corresponding CVDs of the measurements depicted in Figs. 5.3 and 5.4, respectively. Further, the MCS are depicted along with the CVDs. For the five considered gait classes, an interpretation of the CVDs and MCS is given in the following.

NORMAL WALK (NW) As shown in Figs. 5.9a and 5.10a, the CVD and the MCS for normal walking reveal a fundamental cadence frequency of approximately 1 Hz for both motion directions. In particular, for absolute Doppler frequencies larger than 150 Hz the CVD shows the periodicity of the micro-Doppler components, i.e., the step signatures. In addition to the stride rate the mean cadence spectrum shows harmonics, i.e., peaks at integer multiples of the cadence frequency.

LIMPING WITH ONE LEG (L1) The corresponding CVDs and MCS of simulated limping toward and away from the radar are depicted in Figs. 5.9b and 5.10b, respectively. The step rates for these walks are found as 0.8 Hz and 1.1 Hz, respectively, by detecting the highest peak in the mean cadence spectrum, whereby the first peak due to the torso's motion is ignored. Additionally, we observe a peak at half of this cadence frequency, which represents the periodicity of every other micro-Doppler signature. That hints at the fact that the alteration of every other stride signature can be revealed by utilizing the CVD.

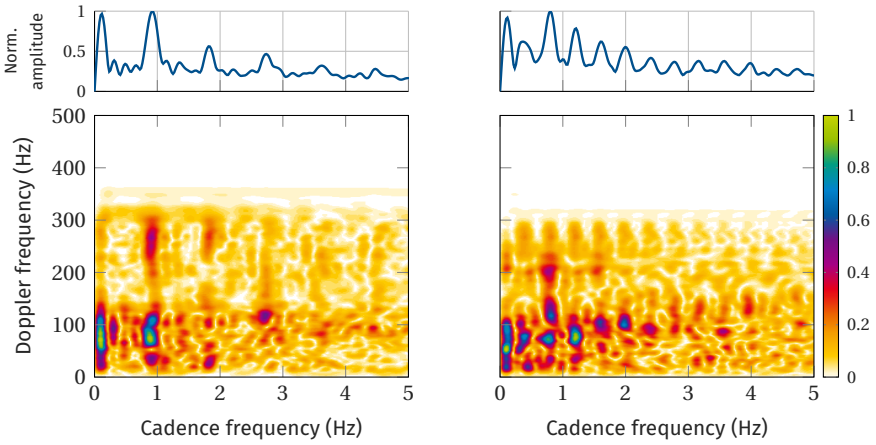

(a) normal walk (NW)

(b) limping with one leg (L1)

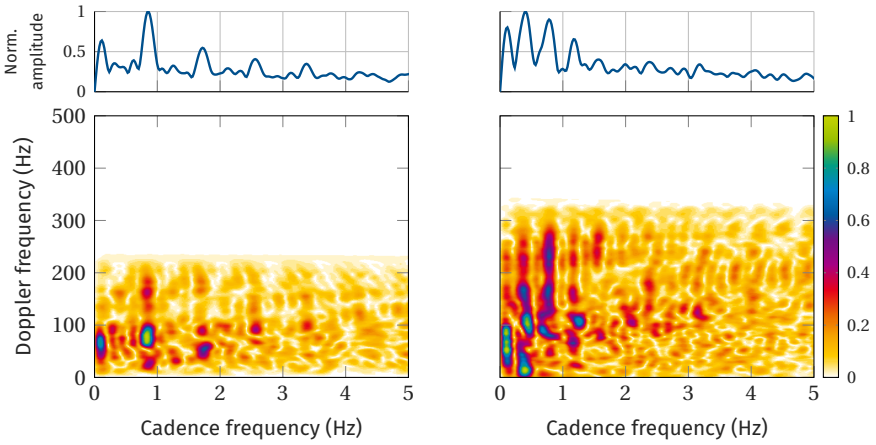

(c) limping with both legs (L2)

(d) walking with a cane (CW)

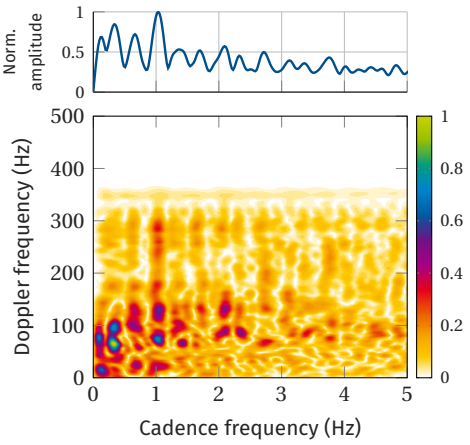

(e) walking with a cane out of sync (CW/oos)

Figure 5.9: Examples of cadence-velocity diagrams (CVDs) and mean cadence spectra (MCS) for walking toward the radar system. In the CVD, the color indicates normalized amplitudes. The CVDs are obtained from the spectrograms in Fig. 5.3.

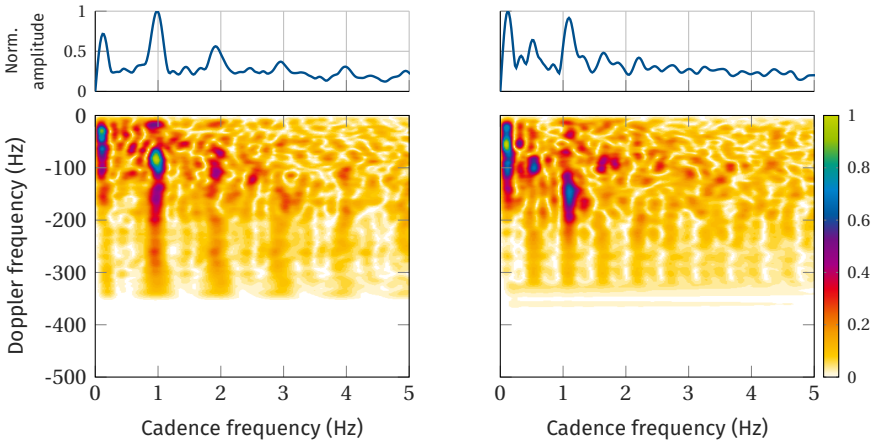

(a) normal walk (NW)

(b) limping with one leg (L1)

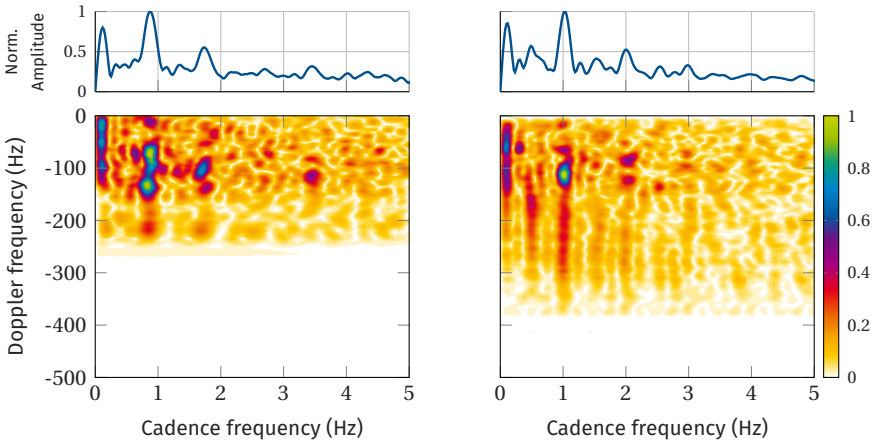

(c) limping with both legs (L2)

(d) walking with a cane (CW)

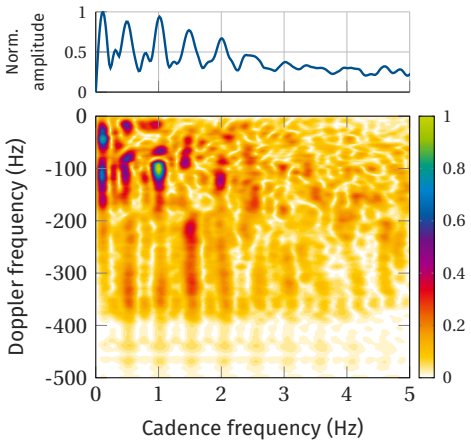

(e) walking with a cane out of sync (CW/oos)

Figure 5.10: Examples of cadence-velocity diagrams (CVDs) and mean cadence spectra (MCS) for walking away from the radar system. In the CVD, the color indicates normalized amplitudes. The CVDs are obtained from the spectrograms in Fig. 5.4.

The remaining peaks in the mean cadence spectrum correspond to harmonics of the stride rate and harmonics of half of the stride rate.

LIMPING WITH BOTH LEGS (L2) The CVDs and MCS for walks, where both legs were not fully bent are shown in Figs. 5.9b and 5.10b. From the MCS it is very difficult to discern these measurements from those of a normal gait. However, in the cadence-velocity domain the appearing patterns are distinctive, not least because the maximal Doppler shift of limping with both legs is lower compared to that of a normal gait.

WALKING WITH A CANE (CW) In order to analyze the periodicity of the gait when walking with a cane, the corresponding CVDs along with the MCS are shown in Figs. 5.9d and 5.10d. We note, that the CVD as well as the MCS for walking with a cane are very similar to those for an abnormal walk. This is due to the fact that in both cases every other micro-Doppler stride signature is altered.

WALKING WITH A CANE - OUT OF SYNC (CW/OOS) The CVDs and MCS for walking with a cane out of sync are shown in Figs. 5.9e and 5.10e. They reveal a very characteristic gait pattern: this walking style is irregular as compared to the previous walks, such that the stride rate is not defined in this case. However, from the CVD and MCS, we find a fundamental cadence frequency of 1Hz and 1.4Hz for toward and away from radar walking, respectively. These represent the periodicity of adjacent micro-Doppler stride/cane signatures. Additionally, a peak at one third of this fundamental cadence frequency is observed, which relates to the periodicity of every third micro-Doppler signature, i.e., either cane or stride signatures. The MCS shows additional peaks at integer multiples of both, the fundamental cadence frequency and one third of it.

CLINICAL DATA The CVDs and MCS of the four individuals with diagnosed gait disorders are given and described in Section A.2.1.

6

CLASSIFICATION OF ABNORMAL AND CANE-ASSISTED GAIT

Gait disorders can have various causes. In the elderly, neurological conditions, osteoarthritis and skeletal deformities of the lower limbs are the most common reasons for gait abnormalities [PK17]. Often only one side of the body is affect, e.g., in hemiparesis after suffering from a stroke. The resulting gait disturbances often appear asymmetrical or lead to limping, e.g., in an attempt to avoid weight-bearing on one leg [PK17]. Other medical conditions, such as Parkinson's disease, affect both sides of the body, cause symmetrical but altered gait motions, e.g., taking slow little steps.

gait abnormalities

In addition, a great number of seniors resort to assistive walking devices, such as a cane or a walker, to compensate for decrements in balance, gain mobility and to overcome the fear of falling [GWL+15]. In 2011, 8.5 million U.S. seniors aged 65 and older reported having an assistive walking aid, with the most commonly device being a cane used by two thirds of the elderly [GWL+15]. The correct use of mobility devices is essential to guarantee optimal support and avoid postural deformities. This becomes important in both cases of elderly gaining mobility, and patients recovering from injuries or physical impairment. However, assessing proper handling of walking aids is often difficult for healthcare providers and nursing staff. The information provided by monitoring the elderly's use of a cane inside his/her home can be valuable in designing proper treatment and charting a recovery course. In addition, knowledge of the presence of mobility aids can help in detecting the transition from walking to falling, which will enable keeping the false alarm rate of fall detection systems to a minimum. After all, the latter should be more sensitive in these cases, as mobility device users with a history of falls are more likely to fall again and have an increased fear of falling compared to those who do not use a mobility device [GWL+15]. In particular, cane-only users reported a 30 % higher worry about falls compared to non-device users [GWL+15]. Obviously, the performance of gait monitoring systems should not be impaired by the use of walking aids.

assistive walking devices

Thus, this chapter focuses on the classification of gait abnormalities and cane-assisted walks based on radar micro-Doppler signatures. In Section 6.1, state-of-the-art and new feature extraction methods are introduced, and Section 6.2 presents the experimental results based on real radar data.

The material presented in this chapter is partly taken from [SAZ19; SSAZ18; SAZ18; SZA17].

6.1 FEATURE EXTRACTION

Figure 6.1 gives an overview of the employed feature extraction processes. Based on the radar data representations introduced in Chapter 5, i.e., the spectrogram and the cadence-velocity diagram (CVD), physical features and subspace-based features are extracted. The proposed feature sets will be compared to state-of-the-art features that have been used for human motion classification. The respective feature extraction methods are detailed in the following.

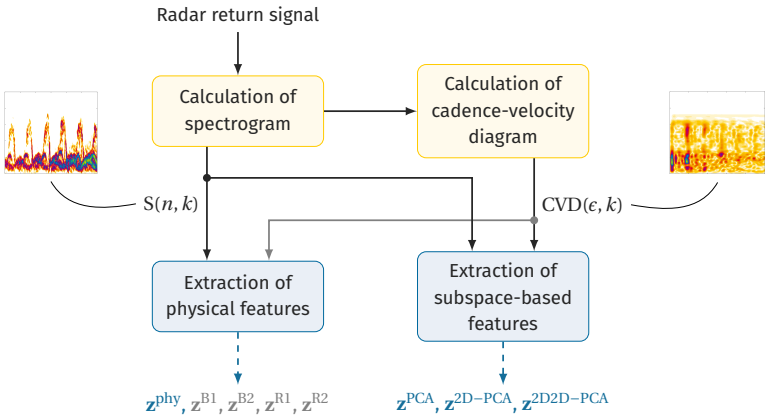

Figure 6.1: Overview of feature extraction processes. After calculating the spectrogram and the cadence-velocity diagram (CVD) (yellow), physical and subspace-based features are extracted (blue). Newly introduced feature sets are highlighted in blue, while state-of-the-art ones are shown in gray.

6.1.1 *Physical Features*

Physical features are generally inter-related and depend on data preprocessing, e.g., noise reduction in the spectrogram, type of radar used, environment, and target characteristics [BPH15; GECT15]. Since the features play an important role in classification problems, they should be chosen to be relevant to the considered classification problem, and accurately estimated or extracted from the micro-Doppler signature or its transforms [GECT15]. Features of physical interpretations have been widely used for radar-based human activity recognition and include, but are not limited to [KL09; Ote05]:

- torso's Doppler frequency or radial velocity,
- total Doppler bandwidth,
- offset of the total Doppler,
- Doppler bandwidth without micro-Doppler effects,
- normalized standard deviation of Doppler signal strength,
- period of the limb motion or stride rate,
- stride length,
- RCS of some moving body components (gait amplitude ratio).

In the following, the offerings of these features for gait recognition are examined.

base velocity

In order to estimate the average radial velocity of a person, often referred to as base velocity v_0, the mean Doppler spectrum is calculated as given by Eq. (5.4). Here, the mean Doppler spectrum is smoothed to minimize the influence of noise by applying a moving average filter with a span corresponding to approximately 11Hz in Doppler frequency or 0.07m/s. Next, the maximum value of the mean Doppler spectrum is determined, and the corresponding Doppler frequency serves as an estimate of v_0 by using Eq. (2.5).

An important characteristic of a person's walk is the gait periodicity, which corresponds to the stride rate for a normal walk. However, in the case of cane-assisted walks, the strides may not be periodic due to the additional cane movements (see Fig. 5.3e and Fig. 5.4e). Hence, we introduce the micro-Doppler repetition frequency f_{mD}, which captures the periodicity of the micro-Doppler signatures irrespective of being due to leg or cane movements. For extracting f_{mD}, the upper and lower envelopes of the micro-Doppler signatures are used for toward and away from radar motions, respectively. Since a swinging foot or a cane motion assumes the highest Doppler shifts during walking, they lead to maxima in the absolute value of the envelope signal (see Fig. 5.8). Taking the FT of the envelope signal, we find f_{mD} by determining the frequency with the maximal amplitude.

micro-Doppler repetition frequency

Next, we consider the maximal observed Doppler shift in the measurement as a feature. This is motivated by the observation that a limping leg has a lower radial velocity, and thus causes smaller maximal Doppler shifts. The maximal Doppler shift $f_{\mathrm{max}}^{\mathrm{D}}$ is estimated utilizing the maximal values of the envelope signal. Here, the mean of the highest 10 % of values is used to be less sensitive to variations between different micro-Doppler step signatures.

maximal Doppler shift

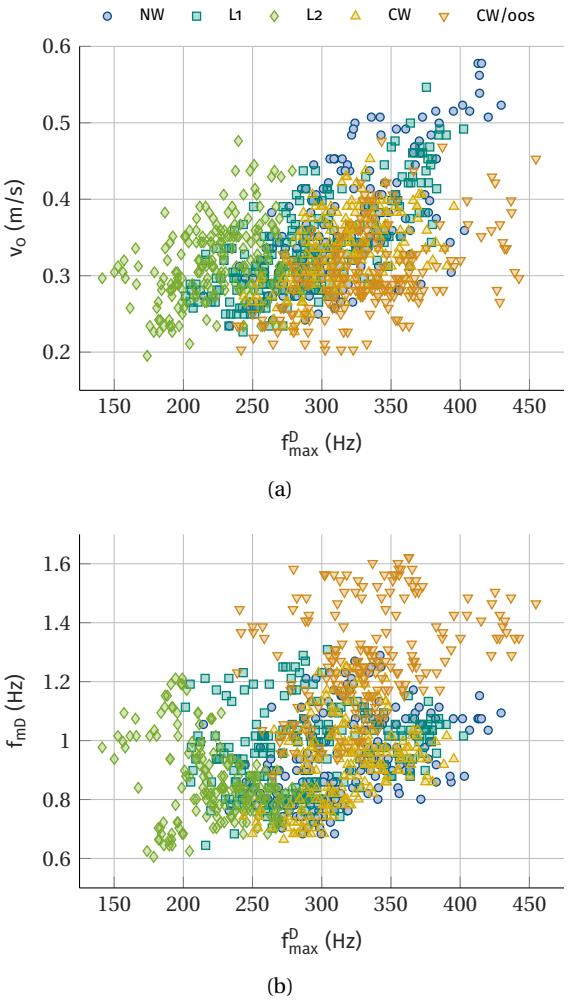

Figure 6.2: Scatter plots of physical features. (a) Base velocity v_0 vs. maximal Doppler shift $f_{\mathrm{max}}^{\mathrm{D}}$, and (b) micro-Doppler repetition frequency f_{mD} vs. maximal Doppler shift $f_{\mathrm{max}}^{\mathrm{D}}$.

In order to show relevance, Fig. 6.2 presents scatter plots of the three described features, namely the base velocity v_0, the micro-Doppler repetition frequency f_{mD}, and the maximal Doppler shift $f^{\mathrm{D}}_{\mathrm{max}}$, for the five considered gait classes. From Fig. 6.2a, it can be seen that the base velocity is not discriminative of the walks, because the walking speed of a person is not (necessarily) influenced by the use of an assistive walking device or gait impairments. However, the scatter plot in Fig. 6.2b reveals that the micro-Doppler repetition frequency increases when walking with a cane. In particular, we remark that if the cane is moved out of sync (CW/OOS), f_{mD} becomes notably higher compared to the other four classes. Further, we note that limping with both legs (L2) has clearly the lowest maximal Doppler shift among the considered classes.

However, except for limping with both legs (L2), the maximal Doppler shift does not help in discriminating between the remaining gait classes. In this respect, we note that some walking styles exhibit different maximum Doppler shifts per leg or cane motion. In particular, from Figs. 5.3b and 5.4b, we observe that limping with one leg leads to a characteristic pattern of alternating high and low maximal Doppler shifts. For capturing this oscillatory behavior, we find the peaks of the envelope signal and approximate the envelope's envelope using spline interpolation. In order to quantify the variation in maximal Doppler shifts, we proceed to calculate the coefficient of variation as $c_v = \frac{\sigma}{\mu}$, where σ is the standard deviation and μ is the mean of the interpolated signal. The coefficient of variation is expected to be particularly high for limping with one leg (L1) and thus serves as an indicator of abnormality.

coefficient of variation

6.1.1.1 *Physical Features Utilizing Sum-of-Harmonics Analysis*

From Fig. 6.2b, we observe that the gait classes of normal walking (NW), limping with one leg (L1), and walking with a cane in sync with one leg (CW) are not well separated in the feature space spanned by f_{mD} and $f^{\mathrm{D}}_{\mathrm{max}}$. That is, the micro-Doppler repetition frequency f_{mD} by itself, does not capture the underlying regularity or irregularity of the walk. For this, we calculate the gait harmonic frequency ratio as [Alz13]

gait harmonic frequency ratio

$$\beta_0 = \frac{f_0}{f_{\mathrm{mD}}}, \tag{6.1}$$

where f_0 is the fundamental frequency (FF) of the gait. For the considered gait classes, we expect the values of β_0 to be:

- 1 for NW and L2 as each micro-Doppler stride signature assumes the same pattern,
- 1/2 for L1 and CW as every other micro-Doppler signature appears the same,
- 1/3 for CW/OOS as a set of two strides and one cane movement constitutes one period.

In order to find f_0, we use the short-time energy signal defined in Eq. (5.1) and model it as a sum-of-harmonics (SOH), i.e.,

sum-of-harmonics model

$$\begin{aligned} x(n) &= \sum_{i=1}^{q} u_i \cos(2\pi i f_0 n) + v_i \sin(2\pi i f_0 n) \\ &= \sum_{i=1}^{q} a_i \cos(2\pi i f_0 n + \phi_i), \end{aligned} \tag{6.2}$$

where f_0 is the FF in Hz, q is the number of harmonics (NOH), and the harmonic amplitudes and phases are a_i and ϕ_i, respectively. Here, we use the algorithm proposed in [Whi03] to estimate the FF, the NOH, and harmonic amplitudes and phases. Assuming the energy signal $E(n)$ is composed of an SOH signal $x(n)$ and an additive white Gaussian noise component $u(n)$, i.e.,

$$E(n) = x(n) + u(n), \quad n = 0, \ldots, N-1, \tag{6.3}$$

the parameters can be found by minimizing the squared-error between the data and the model, i.e.,

$$\xi = \sum_{n=0}^{N-1} |x(n) - E(n)|^2, \tag{6.4}$$

and utilizing the nonlinear least squares (NLS) method for estimating f_0, which is augmented by a model order selection method for detecting q [Whi03]. For this, Eq. (6.4) is jointly optimized over candidate FFs and candidate orders. We use f_{mD} as an initial estimate of the FF. In a first step of the SOH algorithm, this estimate is refined by minimizing Eq. (6.4) using an optimization technique. Next, candidate FFs are determined from the refined f_0 estimate for which the cost function defined by the NLS method is evaluated. At this point, we incorporate prior knowledge to limit computational costs in the joint-optimization for finding f_0 and q, and avoid overfitting. As described earlier, we expect f_0 to be $1/3 \cdot f_{\mathrm{mD}}$, $1/2 \cdot f_{\mathrm{mD}}$ or $1 \cdot f_{\mathrm{mD}}$ given the initial FF estimate f_{mD} is correct. Thus, the candidate FFs assume only the aforementioned values. Given the estimates for the FF and the NOH, the SOH model in Eq. (6.2) is linear in the parameters u_i and v_i. Thus, using the linear least squares (LLS) solution, the harmonic amplitudes a_i and phases ϕ_i, $i = 1, \ldots, q$, can be computed in a closed-form as a function of f_0 and q. The set of estimated parameters is given by $\{f_0, q, a_1 \cdots a_q, \phi_1 \cdots \phi_q\}$.

Given the FF f_0, we proceed to calculate the gait harmonic frequency ratio β_0 using Eq. (6.1). Table 6.1 shows the classification results for all considered walking styles using solely the β_0 feature. The confusion matrix shows that 69.5 %, 73.75 % and 89.5 % of the respective measurements show the expected gait harmonic frequency ratios 1, 1/2 and 1/3, respectively. As such, the gait harmonic frequency ratio is proving to be an important feature to characterize the analyzed walking patterns.

Table 6.1: Confusion matrix for classifying three different gait patterns using the gait harmonic feature β_0. Numbers are given in %.

		Predicted		
		{ NW, L2 }	{ CW, L1 }	CW/OOS
True	{ NW, L2 }	**69.50**	26.75	3.75
	{ CW, L1 }	21.75	**73.75**	4.50
	CW/OOS	5.00	5.50	**89.5**

proposed physical features

Based on the above results and the contributions of the various parameters, we form a physical feature vector as

$$\mathbf{z}^{\text{phy}} = \left[f_{\text{mD}}\ f_{\text{max}}^{\text{D}}\ c_v\ \beta_0\ a_1 \cdots a_{q_{\text{max}}} \right], \tag{6.5}$$

where again f_{mD} is the micro-Doppler repetition frequency, $f_{\text{max}}^{\text{D}}$ is the maximal observed Doppler shift in the measurement, c_v is the coefficient of variation of maximal micro-Doppler shifts, and β_0 is the gait harmonic frequency ratio. The harmonic amplitudes a_i relate to the height of the peaks in the MCS and help to discriminate different articulations of abnormality. Here, $q_{\text{max}} = 5$ is the maximal order of the SOH model and $a_i = 0\ \forall\ i > q$. Note that we do not include the base velocity v_0, as it was found not to be an appropriate discriminative feature for the motions considered.

6.1.1.2 *State-of-the-Art Feature Sets*

We desire to compare the classification performance using the above features with those used by recent works in this field.Here, we limit our comparison to classification techniques that employ the CVD.

Björklund *et al.* [BPH15] used a 77 GHz radar system to discriminate between the motions crawl, creep, walk, jog and run, which were performed by three test subjects. For classification they used features from the cadence-velocity domain and a support vector machine (SVM). By taking the average over all velocities in the CVD, they form the MCS, from which the three highest peaks are identified. At the corresponding cadence frequencies, denoted as f_1, f_2, and f_3, the velocity profiles Γ_1, Γ_2, and Γ_3 are extracted from the CVD, i.e., the energy distribution in the CVD for the given cadence frequencies as a function of the Doppler frequency. The velocity profiles are resampled to have 100 samples each. Further, the base velocity v_0 is extracted by finding the maximum in the mean Doppler spectrum. The corresponding feature vector is given by

features by Björklund et al.

$$\mathbf{z}^{\text{B1}} = [f_1\ f_2\ f_3\ \Gamma_1\ \Gamma_2\ \Gamma_3\ v_0], \tag{6.6}$$

where Γ_i denotes the resampled velocity profile at cadence frequency f_i, $i = 1, \ldots, 3$, and v_0 is the base velocity. Additionally, they define a reduced feature vector as $\mathbf{z}^{\text{B2}} = [f_1\ f_2\ f_3\ |v_0|]$, where the velocity profiles are not considered. Note that they drop the sign of the base velocity by taking the absolute value, i.e., they do take the direction of motion into account.

Ricci and Balleri [RB15] extracted features from the cadence-velocity domain for target recognition and identification. For that, four different subjects were walking on a treadmill in front of a 10 GHz radar at constant speed. For discriminating the targets performing the same motion, the following features were extracted. From the MCS, they obtain an estimate of the person's stride rate. In our work, we resort to f_{mD}, which is more reliably estimated from the envelope of the micro-Doppler signatures. Next, a mean Doppler spectrum $\bar{\Gamma}_{\text{mD}}$ is formed around f_{mD} by averaging over $\delta = 5$ neighboring cadence frequencies corresponding to 0.825 Hz cadence bandwidth. The second and third feature, $f_{\text{mD,min}}^{\text{D}}$ and $f_{\text{mD,max}}^{\text{D}}$, are found by determining the minimum and maximum Doppler frequencies in $\bar{\Gamma}_{\text{mD}}$ exceeding a predefined threshold $\gamma = 0.05$. Thus, the first feature vector is defined as

features by Ricci and Balleri

$$\mathbf{z}^{\text{R1}} = [f_{\text{mD}}\ f_{\text{mD,min}}^{\text{D}}\ f_{\text{mD,max}}^{\text{D}}]. \tag{6.7}$$

Second, the mean Doppler spectrum around f_{mD} is used to define the feature vector $\mathbf{z}^{\text{R2}} = \bar{\Gamma}_{\text{mD}}$.

6.1.2 *Subspace-Based Features*

For feature extraction, both 2D signal representations from Chapter 5, i.e., the spectrogram and the CVD, are considered as images. Principal component analysis (PCA) can be used to learn intrinsic characteristics of data by finding a set of orthonormal basis that can be used to reconstruct the data by appropriate weighting. Using only a subset of the obtained basis, the high-dimensional data can efficiently be represented in a lower dimensional subspace. We note that subspace-based features do not necessarily bear one-to-one correspondence to human motion kinematics.

6.1.2.1 *Principal Components Analysis*

For PCA-based feature learning, the 2D signal representations are considered as images denoted by $\mathbf{X} \in \mathbb{R}^{N_x \times N_y}$, where N_x and N_y are the dimensions of the image. First, the input images are vectorized row-wise, i.e., $\mathbf{x} = \text{vec}\{\mathbf{X}^\text{T}\} \in \mathbb{R}^{Q\times 1}$, and stacked column-wise to form a data matrix $\mathbf{Y}$, such that

$$\mathbf{Y} = [\mathbf{x}_1\ \mathbf{x}_2\ \cdots\ \mathbf{x}_P] \in \mathbb{R}^{Q\times P}, \tag{6.8}$$

where $Q = N_x \times N_y$ is the total number of image pixels, and P is the number of training images. The principal components are then given by the eigenvectors of the covariance matrix of $\mathbf{Y}$ that correspond to the largest eigenvalues. There are various methods to compute the principal components [Shl14]. We apply singular value decomposition (SVD) to decompose the data matrix such that $\mathbf{Y} = \mathbf{UDV}^\text{T}$, where the columns of $\mathbf{U}$ and $\mathbf{V}$ are the left and right eigenvectors, respectively, and the diagonal entries of the diagonal matrix $\mathbf{D}$ are the singular values. The eigenvalues are related to the singular values by $\Lambda = 1/(P-1)\mathbf{D}^2$ [Koc13]. The left eigenvector that has the largest eigenvalue, i.e., explains most of the variance in the data, is the first principal component. Using λ principal components, which span a λ-dimensional subspace of the originally P-dimensional data space, each vectorized training and test image, is projected onto that subspace by

$$\mathbf{p} = \tilde{\mathbf{U}}^\text{T}\mathbf{x}, \tag{6.9}$$

where $\tilde{\mathbf{U}} \in \mathbb{R}^{Q\times\lambda}$ are the eigenvectors, or eigenimages, corresponding to the first λ eigenvalues. The resulting projections $\mathbf{p} \in \mathbb{R}^{\lambda\times 1}$ form the feature vector used for classification, i.e.,

PCA-based features

$$\mathbf{z}^\text{PCA} := \mathbf{p} = [p_1\ p_2\ \cdots\ p_\lambda]^\text{T}, \quad \lambda \le P \in \mathbb{N}. \tag{6.10}$$

6.1.2.2 *Two-Dimensional Principal Components Analysis*

Contrary to PCA, two-dimensional principal component analysis (2D-PCA) operates on the image directly without prior vectorization [YZFY04]. From the image covariance matrix given by

$$\mathbf{H} = \frac{1}{P}\sum_{i=1}^{P}\left(\mathbf{X}_i - \bar{\mathbf{X}}\right)^\text{T}\left(\mathbf{X}_i - \bar{\mathbf{X}}\right), \tag{6.11}$$

where $\bar{\mathbf{X}} = \frac{1}{P}\sum_{i=1}^{P}\mathbf{X}_i$ is the average training image, the optimal projection axes are found by maximizing the generalized total scatter criterion $J(\mathbf{\Phi}) = \mathbf{\Phi}^\text{T}\mathbf{H}\mathbf{\Phi}$. The unitary vector that maximizes $J(\mathbf{\Phi})$, i.e., the eigenvector of $\mathbf{H}$ corresponding to the largest eigenvalue, gives the optimal projection axis. Let $\mathbf{\Phi}$ be the

optimal projection matrix whose columns contain β optimal projection axes, i.e., $\boldsymbol{\phi}_1, \ldots, \boldsymbol{\phi}_\beta, \beta \leq N_y \in \mathbb{N}$, an image $\mathbf{X}$ is projected by

$$\mathbf{P} = \mathbf{X}\boldsymbol{\Phi}. \tag{6.12}$$

2D-PCA-based features

The obtained feature matrix $\mathbf{P} \in \mathbb{R}^{N_x \times \beta}$ is vectorized prior to classification, i.e., $\mathbf{z}^{\text{2D-PCA}} := \text{vec}\{\mathbf{P}\}$.

6.1.2.3 *Two-Directional Two-Dimensional Principal Components Analysis*

The 2D-PCA operates along the row direction of the input images [ZZ05]. In order to take the information along the image columns into account, we utilize two-directional two-dimensional principal component analysis (2D2D-PCA). To this end, we calculate the image covariance matrix

$$\mathbf{V} = \frac{1}{P} \sum_{i=1}^{P} \left(\mathbf{X}_i - \bar{\mathbf{X}}\right) \left(\mathbf{X}_i - \bar{\mathbf{X}}\right)^{\mathrm{T}}, \tag{6.13}$$

where $\bar{\mathbf{X}} = \frac{1}{P} \sum_{i=1}^{P} \mathbf{X}_i$ is again the average training image. Maximizing the following generalized total scatter criterion $J(\boldsymbol{\Omega}) = \boldsymbol{\Omega}^{\mathrm{T}} \mathbf{V} \boldsymbol{\Omega}$, the optimal projection axes are given by the eigenvectors of $\mathbf{V}$. Using γ eigenvectors corresponding to the largest eigenvalues, we obtain γ optimal projection axes $\boldsymbol{\omega}_1, \ldots, \boldsymbol{\omega}_\gamma$, where $\gamma \leq N_x \in \mathbb{N}$. Let $\boldsymbol{\Omega}$ be the optimal projection matrix whose columns are given by $\boldsymbol{\omega}_1, \ldots, \boldsymbol{\omega}_\gamma$, the subspace representation of an image $\mathbf{X}$ is obtained by

$$\mathbf{P} = \boldsymbol{\Omega}^{\mathrm{T}} \mathbf{X} \boldsymbol{\Phi}. \tag{6.14}$$

2D2D-PCA-based features

The 2D2D-PCA feature matrix $\mathbf{P} \in \mathbb{R}^{\gamma \times \beta}$ is vectorized prior to classification, i.e., $\mathbf{z}^{\text{2D2D-PCA}} := \text{vec}\{\mathbf{P}\}$.

6.2 EXPERIMENTAL RESULTS

6.2.1 *Methodology*

RADAR DATA REPRESENTATIONS The investigated radar data representations and their dimension are summarized in Table 6.2.

Using measurements of 6 s duration sampled at 2.56 kHz, we calculate the spectrogram using Eq. (2.7), where a Hamming window of approximately 0.1 s length ($M = 256$) is applied and the STFT is evaluated at $K = 2048$ frequency points. An excerpt of the spectrogram is used with Doppler components smaller than 500 Hz, and its amplitude is normalized to the range of [0,1]. To further reduce the dimensionality of the spectrogram, it is sub-sampled in the time-domain by a factor of 20 and image binning is applied, where groups of 4×4 pixel are averaged. Thus, the spectrogram has $101 \times 192 = 19392$ entries.

spectrogram

In order to compensate for the time dependence of the spectrogram, we automatically extract four step signatures per measurement and limit the Doppler axis to the maximal observed Doppler shift. This representation will be referred to as aligned spectrogram in the following. We note that some gait spectrograms still show different initial stride types, e.g., the first step can be normal or abnormal.

aligned spectrogram

Next, the CVD is calculated according to Eq. (5.2), where zero-padding is used to obtain a cadence frequency granularity of approximately 0.04 Hz. Again, the relevant part of the CVD images is extracted. In this regard, cadence frequencies up to 5 Hz and Doppler frequencies from 0 Hz and 500 Hz and −500 Hz

Table 6.2: Radar data representations and their dimensions.

Representation	Dimension $N_x \times N_y$	Number of entries Q
Spectrogram	101 × 192	19392
Aligned spectrogram	101 × 129	130129
(Preprocessed) cadence-velocity diagram (CVD)	101 × 129	13029
(Preprocessed) mean cadence spectrum (MCS)	1 × 129	129
FT of filtered time-domain signal	1 × 129	129

and 0 Hz are considered for toward and away from radar measurements, respectively. Further, the resulting CVD image is downsampled in the Doppler domain to yield an image of dimensions 101 × 129 pixels, and is normalized to have values in the range of [0,1]. From this excerpt of the CVD, the MCS is obtained via Eq. (5.3).

cadence-velocity diagram

As we are particularly interested in the characteristic pattern in the CVD image, different stride rates and different maximal Doppler shifts among the measurements are compensated so as to align the CVD images. From Figs. 5.9 and 5.10, we observe that along the Doppler frequency axis, the CVDs contain information up to the maximal observed Doppler shift. Hence, it is natural to consider the CVD images only up to this limit. Further, walks vary in micro-Doppler repetition frequency f_{mD}, where the amplitudes of the harmonic components decrease with increasing cadence frequency and the gait pattern is diminished beyond approximately 5 Hz. In order to assess the relevance of compensating for different maximal observed Doppler shifts $f^{\mathrm{D}}_{\max}$ and micro-Doppler repetition frequencies f_{mD}, we analyze the classification performance using the following preprocessed CVDs:

preprocessed cadence-velocity diagram

- CVD: considered up to ±500 Hz Doppler frequency and 5 Hz cadence frequency,
- CVD($f^{\mathrm{D}}_{\max}$): considered up to $f^{\mathrm{D}}_{\max}$ and 5 Hz cadence frequency,
- CVD(f_{mD}): considered up to ±500 Hz Doppler frequency and $5 \cdot f_{\mathrm{mD}}$ (Hz) cadence frequency
- CVD($f^{\mathrm{D}}_{\max}$,f_{mD}): considered up to $f^{\mathrm{D}}_{\max}$ and $5 \cdot f_{\mathrm{mD}}$ (Hz) cadence frequency,

where $f^{\mathrm{D}}_{\max}$ and f_{mD} are extracted from the spectrogram as described in Section 6.1.1. Examples of preprocessed CVDs are given in Section A.2.3. Hereafter, these CVDs will be referred to as preprocessed CVDs with an image dimension of 101 × 129 pixels. As for the raw CVD images, we can find the preprocessed MCS from CVD(f_{mD}) using Eq. (5.3).

Finally, one can utilize the time-domain signal itself, where the lower Doppler components due to the torso's motion are removed by high-pass filtering the signal with a cut-off frequency corresponding to $2v_0$. Taking the FT of this high-pass filtered signal, we obtain a similar representation as the MCS with peaks at the fundamental cadence and its harmonics.

FT of filtered time-domain signal

CLASSIFICATION In order to demonstrate the importance of choosing appropriate data representations for PCA-based feature extraction, we evaluate their respective classification performance w.r.t. the number of principal

components, i.e., number of features, used. Here, a very simple classifier is considered, namely the nearest neighbor (NN) classifier. Final classification results are obtained utilizing 10-fold cross-validation (10FCV), where stratified sampling is applied to preserve the original distribution of the classes in the training and test set. Where appropriate, the confidence interval is indicated for the estimated score, e.g., the classification accuracy. The confidence interval describes a range of values that contains the true value with a given probability, i.e., confidence level. For a score x, the confidence interval is calculated as

$$\left[\bar{x}_{\mathrm{CV}} - t^*_{\alpha,\nu}\frac{\sigma_{\mathrm{CV}}}{\sqrt{N_{\mathrm{CV}}}};\quad \bar{x}_{\mathrm{CV}} + t^*_{\alpha,\nu}\frac{\sigma_{\mathrm{CV}}}{\sqrt{N_{\mathrm{CV}}}}\right], \tag{6.15}$$

where $\bar{x}_{\mathrm{CV}}$ and σ_{CV} are, respectively, the estimated mean and standard deviation of the score based on N_{CV} cross-validation results [JWHT13]. For a confidence level of 95 % (confidence coefficient α=0.05) and $N_{\mathrm{CV}} = 10$, we use $t^*_{0.05,9} \approx 2.26$ based on Student's t-distribution with $\nu = N_{\mathrm{CV}} - 1$ degrees of freedom [Cra99]. Besides classification accuracy, the false positive rate (FPR), false negative rate (FNR), and true positive rate (TPR) are used to assess a classifier's performance. Here, false positives are normal walks that are wrongly classified as abnormal or assisted, and false negatives refer to abnormal or assisted walks that are misclassified as normal walk. Finally, the proposed methods are also evaluated using leave-one-subject-out cross-validation (LOSOCV), where the test set contains data of only one individual at a time. It is noted that in this case also $N_{\mathrm{CV}} = 10$, since ten test subjects participated in the experiments.

6.2.2 *Physical Features*

Table 6.3a shows the classification results using the feature vector as defined in Eq. (6.5) and an NN classifier. In the confusion matrix, the main diagonal elements refer to correct classification rates and off-diagonal entries indicate misclassifications. Thus, the average correct classification rates assume 82.0 %, 88.0 %, 95.0 %, 80.0 %, and 88.0 % for NW, L1, L2, CW and CW/OOS, respectively. The overall accuracy is 86.6 %, with an FPR of 18.0 % and an FNR of 4.4 %. We note that normal walks (NW) are mostly confused with walking with a cane (CW), and vice versa. This is expected in the sense that the underlying motion of walking with a cane is a normal walk, where the cane's micro-Doppler signatures superimpose every other leg micro-Doppler signature.

Next, Table 6.3b presents the classification results using the feature vector $\mathbf{z}^{\mathrm{B1}}$ proposed by Björklund *et al.* [BPH15]. For comparison, we use the same classifier as for the physical features, namely, the NN classifier. Using the first feature vector ($\mathbf{z}^{\mathrm{B1}}$), the overall correct classification rate assumes 79.4 %, with an FPR of 6.0 % and an FNR of 7.1 %. Despite the increased number of features, the average correct classification rate is lower compared to using $\mathbf{z}^{\mathrm{phy}}$. Removing the velocity profiles from the feature vector, i.e., using $\mathbf{z}^{\mathrm{B2}}$, the classification accuracy decreases to only 40.4 %, which shows that the cadence frequencies f_1, f_2 and f_3 along with the base velocity v_0 are not key in discriminating the considered gait classes.

Using the feature vectors $\mathbf{z}^{\mathrm{R1}}$ and $\mathbf{z}^{\mathrm{R2}}$ defined by Ricci and Balleri [RB15], the results are given in Tables 6.3c and 6.3d, respectively. In the first case, the parameters Δm and γ were optimized as to achieve the highest accuracy. The overall accuracy is found as 60.7 % with an FPR of 56.6 % and an FNR of 13.6 %. We again observe that normal walking (NW) is mostly confused with cane-assisted walks (CW) and vice versa. Using the mean Doppler spectrum around

Table 6.3: Confusion matrices for different physical feature sets. Results are obtained using an NN classifier and 10FCV. Numbers are given in %.

(a) Proposed physical features ($\mathbf{z}^{\text{phy}}$)

		Predicted				
		NW	L1	L2	CW	CW/OOS
True	NW	**82.0**	1.5	5.0	9.0	2.5
	L1	3.5	**88.0**	2.0	3.5	3.0
	L2	2.5	1.5	**95.0**	1.0	0.5
	CW	9.5	5.5	3.0	**80.0**	2.0
	CW/OOS	2.0	6.0	2.0	2.0	**88.0**

(b) Björklund *et al.* [BPH15] ($\mathbf{z}^{\text{B1}}$)

		Predicted				
		NW	L1	L2	CW	CW/OOS
True	NW	**94.0**	1.5	1.5	2.5	0.5
	L1	8.5	**78.0**	5.5	5.0	3.0
	L2	1.5	3.0	**90.5**	2.5	2.5
	CW	13.0	6.5	5.5	**69.5**	5.5
	CW/OOS	5.5	7.0	5.0	17.5	**65.0**

(c) Ricci and Balleri [RB15] ($\mathbf{z}^{\text{R1}}$)

		Predicted				
		NW	L1	L2	CW	CW/OOS
True	NW	**43.5**	15.5	11.0	21.0	9.0
	L1	14.5	**49.0**	15.0	15.0	6.5
	L2	10.5	10.0	**77.0**	2.0	0.5
	CW	21.5	11.0	2.5	**57.5**	7.5
	CW/OOS	8.0	5.0	-	10.5	**76.5**

(d) Ricci and Balleri [RB15] ($\mathbf{z}^{\text{R2}}$)

		Predicted				
		NW	L1	L2	CW	CW/OOS
True	NW	**78.5**	5.0	5.0	9.5	2.0
	L1	9.5	**73.0**	9.0	4.0	4.5
	L2	4.5	7.0	**83.5**	4.0	1.0
	CW	9.0	4.5	3.5	**75.5**	7.5
	CW/OOS	11.0	5.0	1.5	18.0	**64.5**

f_{mD} as a feature, i.e., $\mathbf{z}^{\mathrm{R2}}$, the overall accuracy is 75.0 %, where the FPR and FNR assume 21.5 % and 8.5 %, respectively. Again, we note that the mean Doppler spectrum comprises more information for classification of the considered motions than single Doppler or cadence frequencies.

6.2.3 *Subspace-Based Features*

Considering the different radar data representations listed in Table 6.2, we first asses their general suitability for the gait classification problem. In addition, we aim to find the optimal dimension of the PCA-based feature vectors, which depends on the number of principal components used to span a subspace for data representation. Here, we choose the number of principal components such that the average classification accuracy is maximized. Toward this end, we analyze the achieved accuracies as a function of the number of principal components.

choice of preprocessed CVD

Before comparing different radar data representations, we focus on the CVD and investigate the effect of preprocessing of the CVDs on the classification accuracy. The classification accuracy for using the aforementioned versions of preprocessed CVDs and PCA-based features is shown in Fig. 6.3. It can be seen that compensating for different $f_{\mathrm{max}}^{\mathrm{D}}$ does not significantly affect the classification performance. However, aligning the CVDs along the cadence frequency axis, i.e., using CVD(f_{mD}) or CVD($f_{\mathrm{max}}^{\mathrm{D}}, f_{\mathrm{mD}}$), the average classification accuracy is improved by 5 % to 10 % depending of the number of principal components. Thus, for further analysis, we use CVD($f_{\mathrm{max}}^{\mathrm{D}}, f_{\mathrm{mD}}$). Examples of eigenimages of the latter are given in Section A.2.2.

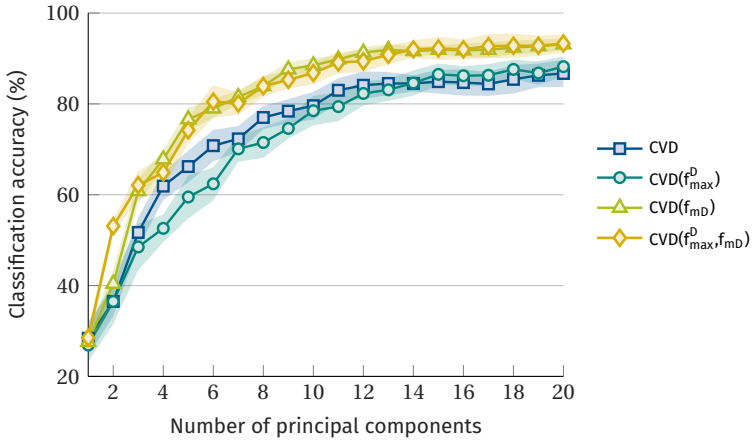

Figure 6.3: Average classification accuracy as a function of the number of principal components used for PCA-based feature extraction based on differently preprocessed CVDs. The shaded areas depict the 95 % confidence intervals for the mean.

choice of radar signal representation

Next, we assess the offerings of different radar signal representations. Figure 6.4 shows the average classification accuracy using the radar data representations listed in Table 6.2, where only the preprocessed CVD and MCS are considered. We find that the spectrogram is inferior to the other representations for extracting descriptive subspace-based features. One reason for the poor classification performance is that the spectrogram is a time-dependent representation of the gait. When aligning the spectrogram, i.e., using only four step signatures per measurement and limit the Doppler axis to the maximal observed Doppler shift, the classification accuracy increases by more than

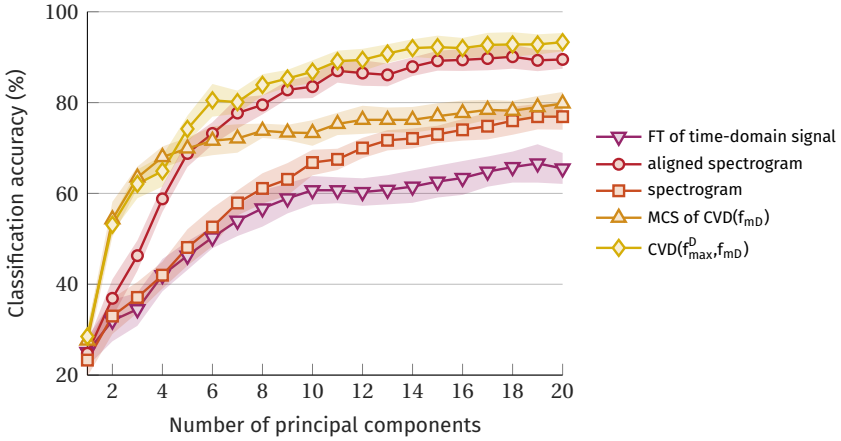

Figure 6.4: Average classification accuracy as a function of the number of principal components used for PCA-based feature extraction based on different radar data representations. The shaded areas depict the 95 % confidence intervals for the mean.

10 %. The preprocessed CVD yields the highest classification rate, which indicates that the CVD contains key information relevant to classification. This information is lost when calculating the MCS, which results in a significant drop in classification performance compared to the CVD when using more than five principal components. The FT of the high-pass filtered time-domain signal yields the poorest classification results. Based on these analysis, the preprocessed CVD is used as a reference in the follow-on comparison below.

classifier parameter optimization

In general, the NN classifier can be easily extended to the κ-NN classifier, which considers a number of κ neighbors in the decision process. Similarly, the parameter κ can be optimized such that the classifier achieves the highest average correct classification rate over all gait classes. Fig. 6.5 illustrates the joint optimization of the parameters λ and κ using preprocessed CVDs, where the color indicates the average correct classification rate. Note that the results for $\lambda < 10$ are omitted for visual clarity, as the corresponding classification rates are significantly lower. We find that the highest accuracy is achieved by using the NN classifier ($\kappa = 1$). Using more than $\lambda = 22$ principal components in the PCA-based feature extraction process does not significantly increase the accuracy. In general, larger values of κ or λ increase computation time.

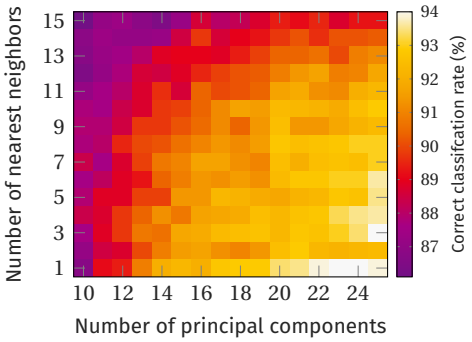

Figure 6.5: Average classification accuracy for different numbers of neighbors κ for the classification process and different numbers of principal components λ used for PCA-based feature extraction based on preprocessed CVDs.

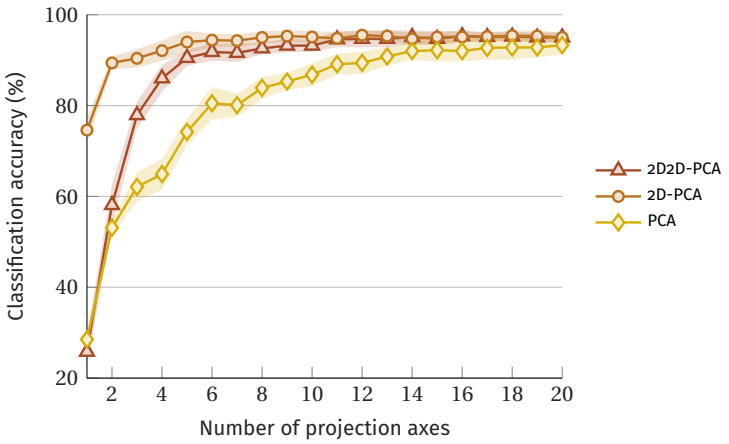

Figure 6.6: Average classification accuracy as a function of the number of principal components used in different PCA-based feature extraction methods based on the preprocessed CVD. The shaded areas depict the 95% confidence intervals for the mean.

choice of feature learning method

Finally, we evaluate the classification performance using PCA, 2D-PCA, and 2D2D-PCA for feature extractions. Figure 6.6 shows the classification results using the aforementioned methods and the preprocessed CVD, i.e., CVD($f^{\mathrm{D}}_{\max}$,f_{mD}). It can be seen that 2D-PCA outperforms PCA and 2D2D-PCA in terms of accuracy, when using only a small number of projection axes for feature extraction. Note that β is chosen equal to γ for 2D2D-PCA. The highest classification rate of 94 % is achieved by using 2D-PCA and $\beta = 5$ projection axes. Using more projection axes does not significantly increase the classification accuracy.

In [SSAZ18] it was shown that the computation times for of 2D-PCA and 2D2D-PCA are similar, while the classification accuracy is slightly higher in the case of 2D-PCA. Further, the rows of the joint-variable signal representation contains more information for discriminating different gait classes than its columns. Thus, because of the special pattern in the images at hand, 2D2D-PCA does not outperform 2D-PCA in this case.

Detailed classification results using subspace-based features are presented by means of confusion matrices. Table 6.4a shows the classification results utilizing PCA-based features of CVDs and the NN classifier. Here, $\lambda = 22$ principal components are used. The overall accuracy assumes 93.8 %, where the FPR is 6.5 % and the FNR is 2.1 %. The highest classification rates are achieved for walking with a cane out of sync (98.5 %). The gait class CW shows the lowest classification rate (88.5 %) as this motion is again confused with normal walking (NW), and vice versa. Applying 2D-PCA for feature extraction on the preprocessed CVDs, we obtain the confusion matrix shown in Table 6.4b. Using only five principal components, the 2D-PCA-based features outperform those obtain via standard PCA. The overall accuracy assumes 94.0 %, where the FPR is 5.5 % and the FNR is 2.3 %. As such, the results are comparable to those using PCA-based features, while the number of principal components and the computational complexity is reduced. From Table 6.4c we see that using 2D2D-PCA as a feature extraction technique, the results do not further improve compared to using 2D-PCA. Based on five principal components for both dimensions, the overall classification accuracy reduces to 90.5 %, where the FPR is 8.5 % and the FNR is 2.6 %.

Table 6.4: Confusion matrices for PCA-based feature sets of preprocessed CVDs. Results are obtained using an NN classifier and 10FCV. Numbers are given in %.

(a) PCA-based features ($\mathbf{z}^{\text{PCA}}$)

		Predicted				
		NW	L1	L2	CW	CW/OOS
True	NW	**93.5**	1.0	0.5	4.5	0.5
	L1	-	**95.5**	-	4.5	-
	L2	1.5	1.5	**93.0**	4.0	-
	CW	6.5	4.0	0.5	**88.5**	0.5
	CW/OOS	0.5	0.5	-	0.5	**98.5**

(b) 2D-PCA-based features ($\mathbf{z}^{\text{2D-PCA}}$)

		Predicted				
		NW	L1	L2	CW	CW/OOS
True	NW	**94.5**	1.0	-	4.0	0.5
	L1	-	**94.0**	0.5	5.5	-
	L2	2.0	3.0	**93.0**	2.0	-
	CW	7.0	2.5	-	**90.0**	0.5
	CW/OOS	-	0.5	0.5	0.5	**98.5**

(c) 2D2D-PCA-based features ($\mathbf{z}^{\text{2D2D-PCA}}$)

		Predicted				
		NW	L1	L2	CW	CW/OOS
True	NW	**91.5**	0.5	-	6.5	1.5
	L1	-	**90.5**	-	7.5	2.0
	L2	2.0	1.5	**91.5**	5.0	-
	CW	7.0	7.0	-	**83.0**	3.0
	CW/OOS	1.5	1.5	-	1.0	**96.0**

Table 6.5: Confusion matrices for PCA-based features of preprocessed CVDs. Results are obtained using an NN classifier and LOSOCV. Numbers are given in %.

		Predicted				
		NW	L1	L2	CW	CW/OOS
True	NW	**76.5**	0.5	2.5	20.5	-
	L1	0.5	**83.5**	0.5	15.5	-
	L2	9.0	1.5	**83.0**	6.5	-
	CW	17.0	18.0	3.0	**61.5**	0.5
	CW/OOS	-	2.0	-	0.5	**97.5**

LOSOCV

Table 6.5 shows the confusion matrix obtained using PCA-based features of CVDs and LOSOCV opposed to 10FCV. The overall accuracy decreases to 80.4 ± 5.6 % (FPR 23.5 ± 17.9 %, FNR 6.6 ± 3.9 %). Here, $\lambda = 10$ principal components are used and a κ-NN classifier is applied, where $\kappa = 24$. Again, CW/OOS shows the highest accuracy (97.5 %), while most of the confusion appears between normal (NW) and cane-assisted walks (CW). Since each person has its own walking style, the results are promising even though data of more persons are needed for generalization.

clinical data

Lastly, we evaluate the performance of using PCA-based features of preprocessed CVDs and the NN classifier on experimental data of individuals with diagnosed gait disorders. Here, the classifier was trained based on the data of ten healthy individuals performing five different walking styles and evaluated using the data of the four individuals with pathological gait. We can correctly identify the gait as abnormal in 92 % (12/13), 100 % (20/20),75 % (9/12), and 100 % (26/26) of the cases for Person K, L, M, and N, respectively. The cane is correctly detected for Person M in 81 % (13/16) of the cases. Even though the observation time is only 6 s per measurement, we can detect the asymmetry of the gait with very high sensitivity.

6.2.4 *Discussion*

We used radar measurements that contain a representative portion of the gait to classify five different walking styles, including abnormal and assisted gait. Table 6.6 summarizes the results of all presented gait classification methods.

Table 6.6: Comparison of different gait classification algorithms based on their classification accuracy (ACC), false positive rate (FPR) and false negative rate (FNR).

Method	ACC (%)	FPR (%)	FNR (%)
Phy	86.6 ± 1.6	18.0 ± 5.4	4.4 ± 1.5
B1 [BPH15]	79.4 ± 3.1	6.0 ± 4.1	7.1 ± 1.4
R1 [RB15]	60.7 ± 3.2	56.6 ± 6.8	13.6 ± 3.1
R2 [RB15]	75.0 ± 3.6	21.5 ± 8.3	8.5 ± 1.8
PCA	93.8 ± 1.8	6.5 ± 2.4	2.1 ± 0.9
2D-PCA	94.0 ± 2.5	5.5 ± 3.1	2.3 ± 1.5
2D2D-PCA	90.5 ± 1.8	8.5 ± 3.8	2.6 ± 0.8

We find that physical features, such as the base velocity, the micro-Doppler repetition frequency or the maximal Doppler shift in a measurement, are on their own not suited to discriminate all the considered gait classes. While the overall accuracy using a set of carefully chosen physical features (Phy) reaches 86.6 % the FPR is relatively high. State-of-the-art methods utilizing physical features obtained from the cadence-velocity domain (B1, R1, R2) are of limited use for gait recognition, since classification accuracies do not exceed 80 %.

Subspace-based feature extraction methods using the CVD outperforms the use of physical features in terms of classification accuracy, while at the same time reducing the FPR and FNR. Utilizing 2D-PCA for feature extraction and CVD images achieves the highest correct classification rate (94 %), while the FPR (5.5 %) and the FNR (2.3 %) are kept low. The results demonstrate the suitability of the CVD and the effectiveness of PCA for feature extraction.

Even though we only consider one motion class, i.e., gait, and a single signal domain, i.e., the CVD, the proposed method classifies the gaits with a high accuracy. Thus, we conclude that subspace-based features are superior to pre-defined physical features in classifying different gaits, and that the CVD comprises more information on the gait than, e.g., the spectrogram. Despite of the relatively small number of 1000 measurements of ten individuals, it was shown that using automatically learned subspace-based features of CVDs works reasonably good for all gait classes. This is one benefit over popular deep learning approaches, which require a very large (training) data set and are computationally costly [SÖG18; KM16].

7 DETECTION OF GAIT ASYMMETRY

For medical gait analysis, an important domain to be analyzed is the asymmetry of the gait, which refers to the differences between the left and right leg's motions [GM17; LBAN14]. Many pathologies lead to gait asymmetry with various degrees. On the other hand, in rehabilitation, professionals work toward re-establishing a symmetric gait of the patient. Thus, detecting gait asymmetry provides useful information to clinicians and can help in identifying the onsets of many pathological disorders or assess the state of rehabilitation.

To this end, this chapter focuses on detecting gait asymmetry based on radar micro-Doppler signatures. Section 7.1 outlines the proposed framework while Section 7.2 presents the experimental results obtained using real radar data of different persons; including four individuals with diagnosed gait disorders.

The material presented in this chapter is partly taken from [SZA19].

7.1 PROPOSED FRAMEWORK

Figure 7.1 provides an overview of the proposed framework. The figure shows the processing steps to obtain salient features for gait asymmetry detection from a radar return signal. The obtained features are then used to model the probability of observing an asymmetric gait. The individual processing steps are described in more detail in the following sections.

7.1.1 *Preprocessing*

The complex zero-mean radar return signal $s(n)$ is processed to obtain the spectrogram according to Eq. (2.7), where a Hamming window of length $M = 256$ and $K = 2048$ discrete frequency bins are used. The signal length assumes $N = f_s \cdot T = 15360$ samples, where $f_s = 2.56\,\text{kHz}$ is the sampling frequency and $T = 6\,\text{s}$ is the measurement duration. After generating the spectrogram, an adaptive thresholding method is applied to suppress the background noise in the time-frequency domain (see Section A.1.1). From the noise-reduced spectrogram $\mathrm{S}(n,k)$, we calculate the envelope of the micro-Doppler signatures, as explained in Section 5.1.2. The envelope signal $e(n)$ is used to estimate the average Doppler shift of the torso $f^{\mathrm{D}}_{\mathrm{torso}}$, the maximal Doppler shift $f^{\mathrm{D}}_{\mathrm{max}}$, and the step rate f_{step}, as described in Section 6.1.1. Since we do not consider cane-assisted walks in this chapter, f_{mD} corresponds to the step rate, which is refer to it as f_{step} here.

7.1.2 *Extraction of Micro-Doppler Step Signatures*

Utilizing the above information, we automatically extract a representative portion of the spectrogram of four micro-Doppler step signatures $f(x,y)$ of size $M_x \times M_y$, as indicated by the dashed box in Fig. 7.2. In order to calculate an average micro-Doppler step signature of the left and right leg separately, we first estimate the time locations of the steps in $f(x,y)$ by finding the maxima in the envelope signal. Then, four individual step signatures of size $N_x \times N_y$ are

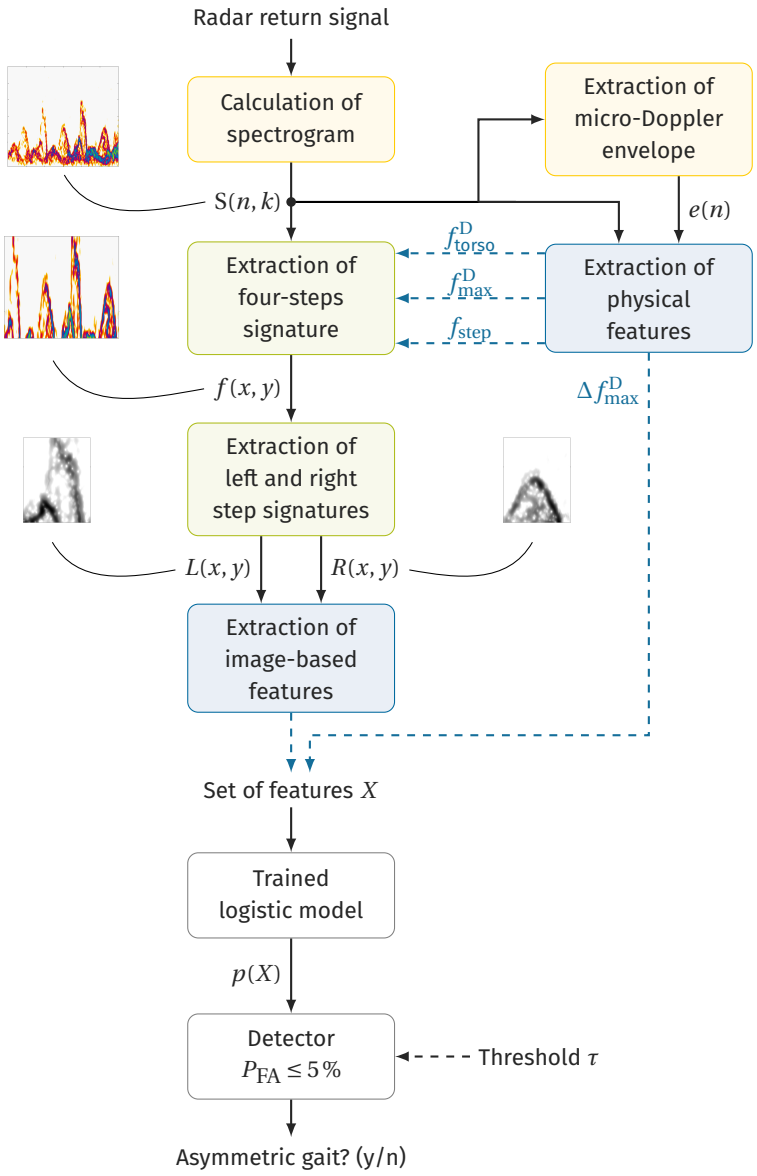

Figure 7.1: Overview of processing steps to detect asymmetric gait from a radar return signal: preprocessing (yellow), micro-Doppler step signature extraction (green), feature extraction (blue), and detection (white).

extracted, where $N_x = \frac{2}{3} \cdot f_s / f_{\text{step}} < M_x$ and $N_y = M_y$. The latter relates to the number of frequency bins that correspond to the range between $1.5 \cdot f^{\text{D}}_{\text{torso}}$ and $f^{\text{D}}_{\text{max}}$. Next, every second step signature is averaged to yield a pair of average micro-Doppler step signatures. Since the envelope's peaks are susceptible to background noise, we refine the initial step time estimates by using an image registration technique. For this, the normalized 2D cross-correlation is calculated as

$$\gamma(u,v) = \frac{\sum_{x,y}\left[f(x,y) - \bar{f}_{u,v}\right]\left[t(x-u,y-v) - \bar{t}\,\right]}{\sqrt{\sum_{x,y}\left[f(x,y) - \bar{f}_{u,v}\right]^2 \sum_{x,y}\left[t(x-u,y-v) - \bar{t}\,\right]^2}}, \tag{7.1}$$

where $f(x,y)$ is the spectrogram of four strides, $t(x,y)$ is an average micro-Doppler step signature positioned at (u,v), $\bar{f}_{u,v}$ is the mean of $f(x,y)$ in the region under t, and $\bar{t}$ is the mean of t [Lew95]. Since we are determined to find

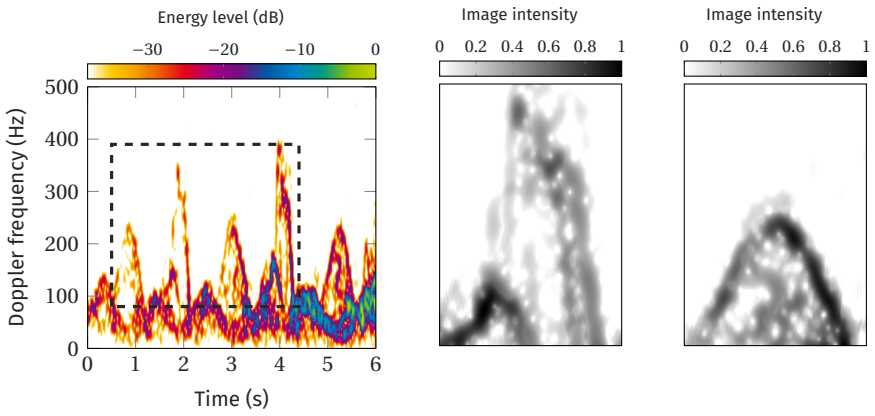

(a) Four steps signature extraction (b) $L(x, y)$ (c) $R(x, y)$

Figure 7.2: Extraction of micro-Doppler step signatures. (a) The dashed box marks the four-steps signature $f(x, y)$ detected utilizing the step rate f_{step}, the maximal Doppler shift $f^{\text{D}}_{\text{max}}$, and the torso's average Doppler shift $f^{\text{D}}_{\text{torso}}$. From $f(x, y)$, average (b) left and (c) right micro-Doppler step signatures are extracted.

the maximal correlation in x-direction, $u = 0, \ldots, M_x - N_x$ and $v = 0$, i.e., t is not shifted in y-direction. The locations in x-direction that maximize γ determine the new time instants of the steps. We perform this procedure for the left and right steps individually, and average the newly obtained signatures again. For easier notation, we hereafter use $R(x, y)$ and $L(x, y)$ to refer to the right and left leg's micro-Doppler signature, respectively. Note, however, that without any prior knowledge, we cannot infer which signature belongs to which leg. For further processing, the step signatures are converted to gray-scale images with amplitudes in the range $[0, 1]$. Examples of average micro-Doppler step signatures are shown in Figs. 7.2b and 7.2c.

7.1.3 *Feature Extraction*

Given the micro-Doppler step signatures $R(x, y)$ and $L(x, y)$ of size $N_x \times N_y$, we aim to quantify the (dis)similarity between them. The intuition being that the more similar $R(x, y)$ and $L(x, y)$ are, the more symmetric the gait. To this end, the features listed in Table 7.1 are extracted.

Table 7.1: Image-based and physical features of micro-Doppler step signatures used for gait asymmetry detection.

Feature	Symbol
correlation coefficient	r
– at high Doppler frequencies	r_H
– at medium Doppler frequencies	r_M
– at low Doppler frequencies	r_L
mean squared error	MSE
mean absolute error	MAE
mean structural similarity index	MSSIM
difference of maximal Doppler shifts	$\Delta f^{\text{D}}_{\text{max}}$

CORRELATION COEFFICIENT The correlation coefficient is calculated as [Mit10]

$$r = \frac{\sum_{x,y}\left[L(x,y)-\bar{L}\,\right]\left[R(x,y)-\bar{R}\,\right]}{\sqrt{\sum_{x,y}\left[L(x,y)-\bar{L}\,\right]^2\sum_{x,y}\left[R(x,y)-\bar{R}\,\right]^2}}, \tag{7.2}$$

where $\bar{L}$ and $\bar{R}$ are the mean of $L(x,y)$ and $R(x,y)$, respectively.

MEAN SQUARED ERROR (MSE) The mean square error (MSE) is given by [Mit10]

$$\mathrm{MSE} = \frac{1}{N_x N_y}\sum_{x,y}\left[L(x,y)-R(x,y)\right]^2. \tag{7.3}$$

MEAN ABSOLUTE ERROR (MAE) The mean absolute error (MAE) is calculated as [Mit10]

$$\mathrm{MAE} = \frac{1}{N_x N_y}\sum_{x,y}\left|L(x,y)-R(x,y)\right| \tag{7.4}$$

MEAN STRUCTURAL SIMILARITY INDEX (MSSIM) The structural similarity (SSIM) index is defined as [WBSS04]

$$\mathrm{SSIM}(R,L) = [l(R,L)]^{\alpha}\cdot[c(R,L)]^{\beta}\cdot[s(R,L)]^{\gamma}, \tag{7.5}$$

where $l(R,L)$, $c(R,L)$, and $s(R,L)$ refer to luminance, contrast and structural measures, and $\alpha=\beta=\gamma=1$. To obtain a single overall quality score of the images, we calculate the mean structural similarity index (MSSIM) given by

$$\mathrm{MSSIM} = \frac{1}{N_x N_y}\sum_{x,y}\mathrm{SSIM}(R,L). \tag{7.6}$$

OFFSET IN MAXIMAL DOPPLER SHIFTS Finally, we also consider a physical feature, i.e., a characteristic that can easily be interpreted. As explained in Section 5.1.1, most asymmetric gaits can be identified by different maximal Doppler shifts of the step signatures. As such, we expect an asymmetric gait to have alternating high and low maximal Doppler shifts due to the steps. Thus, we calculate the average difference between the maximal Doppler shifts of the two legs, $\Delta f^{\mathrm{D}}_{\max}$. This is done by utilizing the detected peaks in the envelope signal, calculating the absolute differences in Doppler frequency of consecutive peaks, and averaging the result.

7.1.4 *Model for Gait Asymmetry Detection*

We seek to model the probability of observing an asymmetric gait based on the extracted features from the previous section. That is, we attempt to answer the question: given a new measurement, how likely is it that we are observing an asymmetric gait? We model the probability of asymmetric gait $p(X) = \Pr(\textit{asymmetric gait}|X)$ using a logistic function given by [JWHT13]

$$p(X) = \frac{e^{b_0+b_1X_1+\cdots+b_dX_d}}{1+e^{b_0+b_1X_1+\cdots+b_dX_d}}, \tag{7.7}$$

where $X=(X_1,\ldots,X_d)$ are the d features or predictors, and $b_0,\ldots,b_d$ are the regression coefficients. The latter are estimated based on the training data using maximum likelihood estimation [JWHT13]. The final decision is based on comparing the probability of asymmetric gait against a threshold τ, i.e., if $p(X)\geq\tau$ we decide for an asymmetric gait.

7.2 EXPERIMENTAL RESULTS

7.2.1 *Experimental Data Set*

The following results are based on a subset of the experimental data outlined in Chapter 4. Here, we consider measurements of ten healthy individuals walking normally and simulating a limping gait by not fully bending one of their knees. Further, the data of four individuals with diagnosed gait disorders is used (see Section 4.2). In total, 471 samples are considered, out of which 271 measurements correspond to (simulated) asymmetric gait. The statistics of the participants and the number of measurements per person and walking direction are given in Table 7.2.

Table 7.2: Overview of the experimental data set for gait asymmetry detection. Persons A–J are able-bodied subjects walking normally and simulating abnormal gait. Persons K–N have different diagnosed gait disorders.

Person	Sex	Age (mean ± SD)	Gait disorder	Number of measurements (toward / away)
A–J	8 male, 2 female	23.8 ± 2.6	no	10 / 10 (each)
			simulated	10 / 10 (each)
K	female	n.a.	yes	7 / 6
L	female	n.a.	yes	11 / 9
M	female	n.a.	yes	7 / 5
N	female	n.a.	yes	13 / 13
A–N	8 male, 6 female	-	-	238 / 233

7.2.2 *Model Selection*

In order to compare models with different numbers of predictors, the Bayesian information criterion (BIC) [Sch78] is utilized. Figure 7.3 shows the lowest BIC values for each model order, i.e., models with d predictors, $d = 1,\dots,8$, where all feature combinations were tested. For each scenario (*both*, *toward*, and *away*), the model which minimizes the BIC is chosen as the final model. The BIC is evaluated based on all available data excluding data of one of the four diagnosed test subjects at a time. As mentioned in Section 5.1.1, Person M shows a slightly different gait asymmetry than the remaining subjects in the data set. Hence, excluding Person M from the model selection process, the BIC decreases for the scenarios *both* and *away*, which indicates a better model fit. In particular, the BIC assumes significantly smaller values for all model orders compared to excluding the other three subjects when considering the *away* scenario. This can be explained by the fact that identifying the gait asymmetry of Person M from behind is challenging (see Fig. 5.6c). In general, Fig. 7.3 suggests to model gait asymmetry separately for toward and away from radar motions, since the BIC curves for both, the separate *toward* and *away* scenario, lie below the curves of *both*.

Table 7.3 lists the models which minimize the BIC for different training sets. Excluding data of one person at a time, the coefficient values along with the

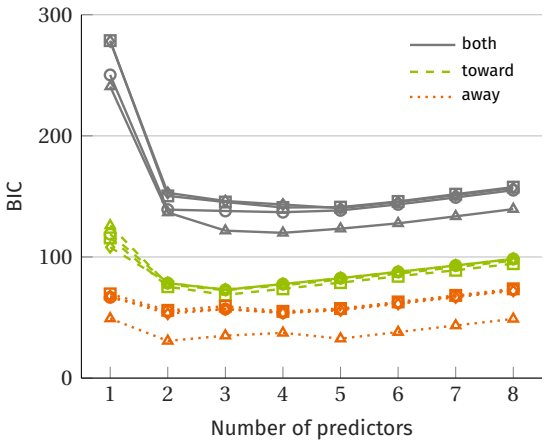

Figure 7.3: Bayesian information criterion (BIC) for model order selection based on the available data excluding Person K (□), Person L (◇), Person M (△), and Person N (○), respectively.

standard error and p-value for the corresponding model are given. The standard error describes how much the coefficient estimate on average deviates from the actual value. In this experiment, standard errors can be large due to the limited number of observations. A small p-value (typically ≤ 0.05) indicates that the predictor is associated with the response. We note that the included predictors are r, r_L, r_H, $\Delta f^{\mathrm{D}}_{\max}$ and MSSIM, while r_M, MSE and MAE are never selected. Remarkably, all models in the *toward* scenario utilize the same predictors (r_H, r_L, $\Delta f^{\mathrm{D}}_{\max}$). For the *away* scenario, the same models are obtained when excluding Person K or N (r, r_L, $\Delta f^{\mathrm{D}}_{\max}$, MSSIM), and Person L or M ($\Delta f^{\mathrm{D}}_{\max}$, MSSIM).

7.2.3 *Gait Asymmetry Prediction*

Using the models given in Table 7.3, we calculate the probabilities of asymmetric gait $p(X)$ for Persons K–N. The threshold τ for deciding for or against asymmetric gait is chosen based on the training data such that the false alarm rate does not exceed 5 %, i.e., $P_{\mathrm{FA}} \leq 5\%$. As an example, Fig. 7.4 shows the receiver operating characteristic (ROC) of the regression model, which is trained on all available data except for data of Person M (see Table 7.4c). Observing the gait from the back (*away*) results in very high detection rates even for small false alarm rates, whereas the scenarios *toward* and *both* are inferior. The ROCs for all cases, i.e., excluding persons K–N individually from the training set, are given in Section A.2.4.

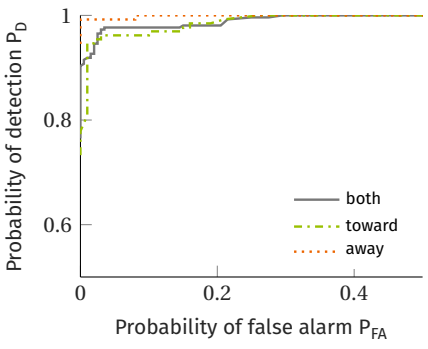

Figure 7.4: Receiver operating characteristic (ROC) for the best model per motion direction. In this case, Person M was excluded from the training set (see Table 7.4c).

Table 7.3: Selected predictors and estimated coefficients of the best logistic regression models for predicting the probability of asymmetric gait. Intercept refers to b_0 in Eq. (7.7).

	Predictor	Coefficient	Std. error	p-value
Toward	intercept	4.5905	1.5588	0.0032
	r_H	−7.9980	2.4388	0.0011
	r_L	−11.8010	2.3603	< 0.0001
	$\Delta f_{\max}^{\mathrm{D}}$	0.0588	0.0236	0.0127
Away	intercept	3.2862	5.4349	0.5454
	r	29.6620	11.3080	0.0087
	r_L	−20.8820	7.6164	0.0061
	$\Delta f_{\max}^{\mathrm{D}}$	0.2147	0.0601	0.0004
	MSSIM	−39.3310	13.6330	0.0039

(a) Excluding Person K

	Predictor	Coefficient	Std. error	p-value
Toward	intercept	3.7248	1.3379	0.0054
	r_H	−6.8083	2.1841	0.0018
	r_L	−10.9560	2.0824	< 0.0001
	$\Delta f_{\max}^{\mathrm{D}}$	0.0689	0.0235	0.0034
Away	intercept	10.5560	5.0276	0.0358
	$\Delta f_{\max}^{\mathrm{D}}$	0.1578	0.0350	< 0.0001
	MSSIM	−32.4720	10.141	0.0014

(b) Excluding Person L

	Predictor	Coefficient	Std. error	p-value
Toward	intercept	3.3993	1.3488	0.0117
	r_H	−6.9438	2.1610	0.0013
	r_L	−10.4210	2.1297	< 0.0001
	$\Delta f_{\max}^{\mathrm{D}}$	0.0729	0.0231	0.0016
Away	intercept	24.1940	13.3100	0.0691
	$\Delta f_{\max}^{\mathrm{D}}$	0.32045	0.1236	0.0095
	MSSIM	−72.8930	33.7520	0.0308

(c) Excluding Person M

	Predictor	Coefficient	Std. error	p-value
Toward	intercept	3.6100	1.3407	0.0071
	r_H	−6.7969	2.1803	0.0018
	r_L	−10.8120	2.0826	< 0.0001
	$\Delta f_{\max}^{\mathrm{D}}$	0.0704	0.0234	0.0026
Away	intercept	2.2173	5.6481	0.6946
	r	28.3000	11.3790	0.0129
	r_L	−21.2280	7.8985	0.0072
	$\Delta f_{\max}^{\mathrm{D}}$	0.2161	0.0601	0.0003
	MSSIM	−35.5050	13.6080	0.0090

(d) Excluding Person N

Table 7.4 shows the probability of correctly detecting the asymmetric gait, $P_{\mathrm{D,test}}$, of the four individuals with gait disorders. Additionally, the decision threshold τ and probability of detection on the training set, $P_{\mathrm{D,train}}$, are given. In general, we can observe that the decision thresholds are lower for the *away* scenario, which indicates that symmetric gait can more reliably be detected from behind (low false alarm rate). Thus, small values of τ can be chosen which increases $P_{\mathrm{D,train}}$. Concerning $P_{\mathrm{D,test}}$, we achieve very high rates in most of the cases, i.e., we can detect asymmetric gait with high probabilities. Although $P_{\mathrm{D,train}}$ assumes higher values for the *away* scenario throughout, we note that for some individuals, it is beneficial to monitor the gait from the front (see Persons L and M), whereas for Person K the *away* scenario yields higher detection rates. Identifying the asymmetric gait of Person M in away-from-radar motions remains challenging, and $P_{\mathrm{D,test}}$ assumes only 40 %.

Table 7.4: Probability of detecting the asymmetric gait ($P_{\mathrm{D,test}}$) of Persons K–N. The decision threshold τ is chosen based on the training data such that $P_{\mathrm{FA}} \leq 5\,\%$. $P_{\mathrm{D,train}}$ gives the detection probability on the training set.

Person	Toward			Away		
	τ	$P_{\mathrm{D,train}}$	$P_{\mathrm{D,test}}$	τ	$P_{\mathrm{D,train}}$	$P_{\mathrm{D,test}}$
K	0.36	96.95 %	85.71 %	0.18	99.21 %	**100.00** %
L	0.36	96.06 %	**100.00** %	0.38	97.58 %	88.89 %
M	0.34	96.18 %	**100.00** %	0.15	99.22 %	40.00 %
N	0.35	96.00 %	**100.00** %	0.17	99.17 %	**100.00** %

7.2.4 *Discussion*

For in-home gait monitoring systems, the observation time is often limited owing to the inherent problem of short motion translation periods associated with household activities. Despite short observation times and using only four steps of the observed gait motion, we were able to detect the gait asymmetry of four diagnosed persons with high accuracy for at least one of the considered motion directions. Since the features are designed to detect differences *between* the two leg motions, this is achieved irrespective of the degree of gait abnormality. Hence, the presented features are considered invariant to the actual appearance of the micro-Doppler step signatures, and thus, to different disorders. Clearly, data of more individuals is needed for a generalization of the obtained results.

8

SUMMARY

This part of the thesis was concerned with solving the intra-motion class classification problem of gait recognition based on Doppler radar measurements.

Using experimental data of 14 volunteers, including four persons with diagnosed gait disorders, we investigated the use of different radar data representations for distinguishing between five gaits, including abnormal and cane-assisted walks. Starting with the often employed spectrogram, a detailed bio-mechanical interpretation of the arising micro-Doppler signatures was given in Chapter 5. From the TFR additional signals can be extracted, e.g., the micro-Doppler envelope signal, which enable the extraction of salient features for gait classification. Next, another 2D signal representation, namely, the CVD, was introduced. It accentuates the periodicity of the monitored walking motions, while retaining the information along the Doppler frequency axis. As for the spectrogram, additional signals are derived from this representation, which were utilized for feature extractions.

The experimental results present in Chapter 6 showed that state-of-the-art physical feature sets are only of limited use, since the classification accuracy does not exceed 80 %. Newly introduced physical features lead to an average correct classification rate of nearly 87 %. Using automated feature learning methods based on PCA, it was demonstrated that the classification accuracy can reach up to 94 % across the five considered gait classes. Here, it was shown that it is important to choose an appropriate signal representation for feature learning. In this case, preprocessed CVDs were found most useful. In order to reduce the computational complexity of the feature extraction process, 2D-PCA can be employed without a loss in classification performance.

In practical in-home scenarios, we might not be interested in distinguishing between a finite number of predefined gait classes, but one would like to monitor the gait over a longer time span and produce an alert whenever the gait patterns become abnormal. A possible measure of gait abnormality is to determine the asymmetry of the gait, which is defined as the difference between the left and right leg's motion. In Chapter 7, we presented a framework to detect gait asymmetry with high probability based on short radar observations and limited experimental data. Here, the gait abnormality of four individuals was correctly detected with high accuracy for at least one motion direction.

In practice, however, gait classes are often neither known nor distinct. For these reasons, the next part ot the thesis focuses on extracting medically relevant gait parameters from radar-micro Doppler signatures in order to assess the use of radar for a more general gait analysis.

REFERENCES

[Alz13] A. Alzogaiby, "Using micro-Doppler radar signals for human gait detection," PhD thesis, Stellenbosch University, Department of Electrical and Electronic Engineering, Dec. 2013 (cit. on p. 56).

[Anc20] Ancortek Inc. (Jun. 2020). SDR-KIT 2400AD, [Online]. Available: http://ancortek.com/sdr-kit-2400ad (cit. on p. 37).

[BJP12] S. Björklund, T. Johansson, and H. Petersson, "Evaluation of a micro-Doppler classification method on mm-wave data," in *IEEE Radar Conference*, 2012. DOI: 10.1109/RADAR.2012.6212271 (cit. on p. 48).

[BPH15] S. Björklund, H. Petersson, and G. Hendeby, "Features for micro-Doppler based activity classification," *IET Radar, Sonar and Navigation*, vol. 9, no. 9, pp. 1181–1187, Dec. 2015. DOI: 10.1049/iet-rsn.2015.0084 (cit. on pp. 47, 48, 54, 58, 62, 63, 68).

[BTT90] R. Boulic, N. M. Thalmann, and D. Thalmann, "A global human walking model with real-time kinematic personification," *The Visual Computer*, vol. 6, no. 6, pp. 344–358, Nov. 1990. DOI: 10.1007/BF01901021 (cit. on p. 41).

[Che19] V. C. Chen, *The Micro-Doppler Effect in Radar*, 2nd ed. Norwood, MA, USA: Artech House, 2019 (cit. on p. 41).

[CPM+15] C. Clemente *et al.*, "A novel algorithm for radar classification based on Doppler characteristics exploiting orthogonal pseudo-Zernike polynomials," *IEEE Transactions on Aerospace and Electronic Systems*, vol. 51, no. 1, pp. 417–430, Jan. 2015. DOI: 10.1109/TAES.2014.130762 (cit. on p. 47).

[Cra99] H. Cramér, *Mathematical Methods of Statistics*. Princeton, NJ, USA: Princeton University Press, 1999 (cit. on p. 62).

[GWL+15] N. M. Gell *et al.*, "Mobility device use in older adults and incidence of falls and worry about falling: Findings from the 2011–2012 national health and aging trends study," *Journal of the American Geriatrics Society*, vol. 63, no. 5, pp. 853–859, May 2015. DOI: 10.1111/jgs.13393 (cit. on p. 53).

[GM17] A. Gouelle and F. Mégrot, "Interpreting spatiotemporal parameters, symmetry, and variability in clinical gait analysis," in *Handbook of Human Motion*, B. Müller *et al.*, Eds., Cham, Germany: Springer, 2017, pp. 1–20. DOI: 10.1007/978-3-319-30808-1_35-1 (cit. on p. 71).

[GECT15] S. Z. Gürbüz *et al.*, "Operational assessment and adaptive selection of micro-Doppler features," *IET Radar, Sonar and Navigation*, vol. 9, no. 9, pp. 1196–1204, Dec. 2015. DOI: 10.1049/iet-rsn.2015.0144 (cit. on p. 54).

[JWHT13] G. James *et al.*, *An Introduction to Statistical Learning*. Springer, 2013. DOI: 10.1007/978-1-4614-7138-7 (cit. on pp. 62, 74).

[KM16] Y. Kim and T. Moon, "Human detection and activity classification based on micro-Doppler signatures using deep convolutional neural networks," *IEEE Geoscience and Remote Sensing Letters*, vol. 13, no. 1, pp. 8–12, Jan. 2016. DOI: 10.1109/LGRS.2015.2491329 (cit. on p. 69).

[KL09] Y. Kim and H. Ling, "Human activity classification based on micro-Doppler signatures using a support vector machine," *IEEE Transactions on Geoscience and Remote Sensing*, vol. 47, no. 5, pp. 1328–1337, May 2009. DOI: 10.1109/TGRS.2009.2012849 (cit. on p. 54).

[Koc13] I. Koch, *Analysis of Multivariate and High-Dimensional Data*. Cambridge, UK: Cambridge University Press, 2013. DOI: 10.1017/CBO9781139025805 (cit. on p. 59).

[LBAN14] S. Lauziere *et al.*, "Understanding spatial and temporal gait asymmetries in individuals post stroke," *International Journal of Physical Medicine & Rehabilitation*, vol. 2, no. 3, pp. 1–11, May 2014. DOI: 10.4172/2329-9096.1000201 (cit. on p. 71).

[Lew95] J. P. Lewis, "Fast template matching," in *Vision Interface*, 1995 (cit. on p. 72).

[Lip06] L. Lippert, "Gait," in *Clinical Kinesiology and Anatomy*, 4th ed., Philadelphia, PA, USA: F. A. Davis, 2006, ch. 21 (cit. on p. 37).

[Mit10] H. B. Mitchell, "Image similarity measures," in *Image Fusion: Theories, Techniques and Applications*, Berlin, Heidelberg, Germany: Springer, 2010, pp. 167–185. DOI: 10.1007/978-3-642-11216-4_14 (cit. on p. 74).

[Ote05] M. Otero, "Application of a continuous wave radar for human gait recognition," in *SPIE Defense and Security*, 2005. DOI: 10.1117/12.607176 (cit. on pp. 47, 54).

[PK17] W. Pirker and R. Katzenschlager, "Gait disorders in adults and the elderly," *Wiener Klinische Wochenschrift*, vol. 129, no. 3-4, pp. 81–95, Oct. 2017. DOI: 10.1007/s00508-016-1096-4 (cit. on p. 53).

[RB15] R. Ricci and A. Balleri, "Recognition of humans based on radar micro-Doppler shape spectrum features," *IET Radar, Sonar and Navigation*, vol. 9, no. 9, pp. 1216–1223, Dec. 2015. DOI: 10.1049/iet-rsn.2014.0551 (cit. on pp. 47, 48, 58, 62, 63, 68).

[Sch78] G. Schwarz, "Estimating the dimension of a model," *Annals of Statistics*, vol. 6, no. 2, pp. 461–464, Mar. 1978. DOI: 10.1214/aos/1176344136 (cit. on p. 75).

[SAZ17] A.-K. Seifert, M. G. Amin, and A. M. Zoubir, "New analysis of radar micro-Doppler gait signatures for rehabilitation and assisted living," in *IEEE International Conference on Acoustics, Speech and Signal Processing*, 2017. DOI: 10.1109/ICASSP.2017.7952908 (cit. on p. 39).

[SAZ18] A.-K. Seifert, M. G. Amin, and A. M. Zoubir, "Radar classification of human gait abnormality based on sum-of-harmonics analysis," in *IEEE Radar Conference*, 2018. DOI: 10.1109/RADAR.2018.8378687 (cit. on pp. 39, 53).

[SAZ19] A.-K. Seifert, M. G. Amin, and A. M. Zoubir, "Toward unobtrusive in-home gait analysis based on radar micro-Doppler signatures," *IEEE Transactions on Biomedical Engineering*, vol. 66, no. 9, pp. 2629–2640, Sep. 2019. DOI: 10.1109/TBME.2019.2893528 (cit. on pp. 37, 39, 53).

[SZA19] A.-K. Seifert, A. M. Zoubir, and M. G. Amin, "Detection of gait asymmetry using indoor Doppler radar," in *IEEE Radar Conference*, (Best Student Paper Award, 1st prize), 2019. DOI: 10.1109/RADAR.2019.8835611 (cit. on p. 71).

[SZA17] A.-K. Seifert, A. M. Zoubir, and M. G. Amin, "Radar-based human gait recognition in cane-assisted walks," in *IEEE Radar Conference*, 2017. DOI: 10.1109/RADAR.2017.7944431 (cit. on pp. 39, 53).

[SSAZ18] A.-K. Seifert *et al.*, "Subspace classification of human gait using radar micro-Doppler signatures," in *European Signal Processing Conference*, 2018. DOI: 10.23919/EUSIPCO.2018.8553592 (cit. on pp. 53, 66).

[SÖG18] M. S. Seyfioğlu, A. M. Özbaygglu, and S. Z. Gürbüz, "Deep convolutional autoencoder for radar-based classification of similar aided and unaided human activities," *IEEE Transactions on Aerospace and Electronic Systems*, vol. 54, no. 4, pp. 1709–1723, Aug. 2018. DOI: 10.1109/TAES.2018.2799758 (cit. on p. 69).

[Shl14] J. Shlens. (Apr. 2014). A tutorial on principal component analysis, [Online]. Available: https://arxiv.org/pdf/1404.1100.pdf (cit. on p. 59).

[WBSS04] Z. Wang *et al.*, "Image quality assessment: From error visibility to structural similarity," *IEEE Transactions on Image Processing*, vol. 13, no. 4, pp. 600–612, Apr. 2004. DOI: 10.1109/TIP.2003.819861 (cit. on p. 74).

[Whi03] G. Whipps, "Coupled harmonics: Estimation and detection," Master's thesis, Ohio State University, Electrical and Computer Engineering, 2003 (cit. on p. 57).

[YZFY04] J. Yang *et al.*, "Two-dimensional PCA: A new approach to appearance-based face representation and recognition," *IEEE Transactions on Pattern Analysis and Machine Intelligence*, vol. 26, no. 1, pp. 131–137, Jan. 2004. DOI: 10.1109/TPAMI.2004.1261097 (cit. on p. 59).

[ZZ05] D. Zhang and Z.-H. Zhou, "$(2D)^2$PCA: Two-directional two-dimensional PCA for efficient face representation and recognition," *Neurocomputing*, vol. 69, no. 1, pp. 224–231, Dec. 2005. DOI: 10.1016/j.neucom.2005.06.004 (cit. on p. 60).

Part III

TOWARD RADAR-BASED GAIT ANALYSIS

"Progress lies not in enhancing what is,
but in advancing toward what will be."

— *Kahlil Gibran*

9 SYSTEM DESCRIPTION AND DATA COLLECTION

The analyses presented in this part of the thesis are based on another experimental data set, which is outlined in this chapter. Section 4.1 introduces the experimental setup for recording the radar data, and Section 4.2 outlines the subject information along with the experimental protocol.

The material presented in this chapter is partly taken from [SGZ20].

9.1 EXPERIMENTAL SETUP

Figure 9.1 schematically shows the experimental setup. The radar data were collected using a continuous-wave radar (SDR-KIT 2400AD, Ancortek, Fairfax, VA, USA) with a transmitting frequency of 24 GHz [Anc20]. The horn antennas, one transmitting and one receiving, were positioned at approximately knee-height, i.e., $h_r - h_t = 0.58\,\text{m}$ above the treadmill surface and $d_r = 1.75\,\text{m}$ in front of or behind the center of the treadmill. At the center of the treadmill, the radar's 3 dB beam width covers the vertical range from approximately 12 cm to 104 cm above the treadmill surface. The radar systems were positioned such that the test subjects walked in a 0° angle to the radar's LOS. Only one radar system was active at a time.

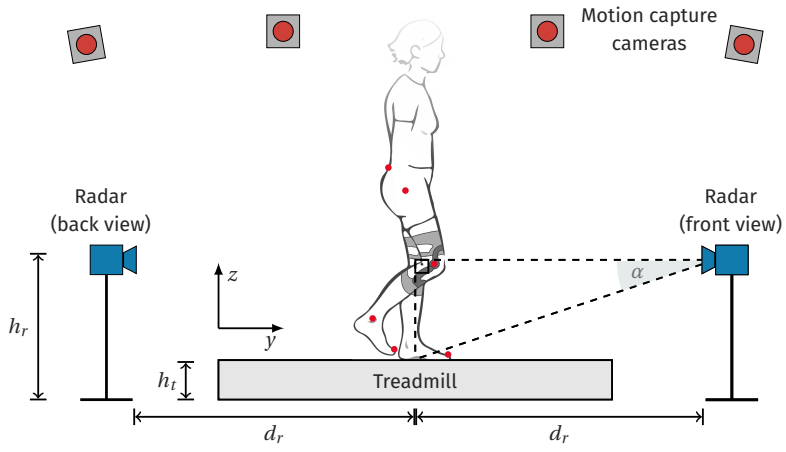

Figure 9.1: Schematic of the experimental setup (at the Locomotion Laboratory, Technische Universität Darmstadt, Germany) with an instrumented treadmill that measures ground reaction forces (GRFs), a motion capture system with 12 infrared cameras, and two radar systems (whereof only one was active at a time). The red dots indicate the positions of the reflective markers on the body for motion capturing. (illustration of person adapted from [Lip06])

Vertical ground reaction forces (GRFs) were individually recorded at 480 GHz for the left and right limb using a custom instrumented treadmill (type ADAL-WR, HEF Tecmachine, Andrezieux Boutheon, France). Based on integrated force-measuring plates (Kistler, Winterthur, Switzerland), one for each leg, the vertical GRF (in z-direction) were acquired for the left and right leg separately.

A three-dimensional (3D) motion capture (MoCap) system (12 high-speed infrared cameras, model Qqus, Qualisys, Sweden) recorded body segment

(a) (b) (c)

Figure 9.2: Photos of (a) the complete experimental setup and (b, c) the placement of nine reflective markers (highlighted by red circles) on a subject for motion capturing.

kinematics from nine reflective markers at 500 GHz. Figure 9.2 shows the positioning of the reflective markers on a test subject for motion capturing. The nine markers were attached to the following body parts: toe (1st metatarsophalangeal joint), ankle (lateral malleolus), knee, hip (greater trochanter head), and lower back (sacrum).

The mono-static radar systems measures the radial velocity of targets (v^{rad}), i.e., velocities along the propagation direction of the EM wave. Since motion velocities along the x-direction are small, and thus do not significantly contribute to the radial we focus on motions in the sagittal plane, i.e., the y-z-plane as illustrated in Fig. 9.1. The radar is positioned at approximately knee height, such that for the knee's velocity we use $v^{\text{rad}} \approx v_y^{\text{moc}}$, where v_y^{moc} is the velocity in y-direction measured by the MoCap system. The radial velocities of ankle and toe, which are measured by the radar system, are approximated by $v^{\text{rad}} \approx v_y^{\text{moc}} \cos\alpha + v_z^{\text{moc}} \sin\alpha$, where $\alpha = 18°$ for the presented setup. Examples of sagittal velocities measured by the MoCap system are given in Fig. 3.3.

In order to simulate asymmetric gait, the right knee flexion was restricted by an adjustable orthosis (50K13 Knieorthese Genu Arexa, Otto Bock Healthcare GmbH, Duderstadt, Germany). Since wearing the orthosis changes the surface of the leg, and thus, its EM reflection characteristics, the study participants wore a second, unconfined orthosis on the left leg to ensure comparability between the radar backscatterings from the left and the right leg. We note that the knee markers were attached to the pivot point of the orthoses' joint, since they covered the knee joints.

9.2 SUBJECT INFORMATION AND EXPERIMENTAL PROTOCOL

Nineteen individuals (5 females and 14 males, aged 28.9 ± 7.5 years, height 176.5 ± 10.0 cm, mass 72.3 ± 11.5 kg) without gait impairment participated in

the study. The study protocol was approved by the Technische Universität Darmstadt ethics commission and all volunteers provided written consent prior to participation. The experiments were conducted at the Locomotion Laboratory at Technische Universität Darmstadt, Germany (no absorbers for EM waves). The test subjects were asked to walk at the center of the treadmill for four consecutive minutes under five different conditions. For the first two minutes the treadmill speed was set to 0.7 m/s, and the speed switched automatically to 1.1 m/s for another two minutes. To account for speeding up and slowing down phases, the first and last 10 s of each two minute interval are neglected such that the measurement duration is 100 s for each walking speed. In the following, the two treadmill speeds 0.7 m/s and 1.1 m/s are also referred to as *slow* and *fast* (speed), respectively. In a random order, the maximum knee flexion of the right knee was confined by an adjustable orthosis. Besides no confinement, which refers to normal gait, four different confinement angles, i.e., 45°, 30°, 20°, 10°, were investigated. Here, the angle describes the extent to which the knee could be bent, where 0° refers to a straight leg, e.g., while standing. These five experiments were performed twice in succession: once with the radar positioned in front of the test subject (five trials with randomized angle of deflection) and once behind the test subject (five trials with randomized angle of deflection). Between each experiment a rest period of approximately 5 min was required to adjust the orthosis and store the data. Due to synchronization errors between MoCap and GRF data, there are only 18 samples available for normal walking and a knee angle confinement of 45°.

10 EXTRACTION OF BIOMECHANICAL PARAMETERS

In this chapter, we utilize motion capture (MoCap) data to validate existing and new methods for extracting a variety of gait parameters from experimental radar data, including spatiotemporal and kinematic parameters. A new method to extract the swing phase (flight time) of individual legs from the radar data is introduced. Additionally, we propose new methods for obtaining sagittal velocities of individual lower limb joints, i.e., toe, ankle and knee velocities. Based on experimental data of 19 able-bodied volunteers walking on a treadmill, we investigate the capabilities of radar to capture gait parameters in unimpaired gait and for gait abnormalities that were introduced by an adjustable orthosis, such that one of the knees could not be fully bent. Further, we present results for two different walking speeds (0.7 m/s and 1.1 m/s) and discuss the differences in positioning the radar in front of or behind the test subject.

The remainder of this chapter is structured as follows. Section 10.1 describes the methods applied for processing radar data and MoCap data utilizing ground reaction forces (GRFs). Further, it covers a new method to detect the onset of the swing phase, the extraction of 11 gait parameters and the applied statistical hypothesis testing scheme for assessing the accuracy of the radar system. Finally, the extracted gait parameters based on radar micro-Doppler signatures and motion capturing are qualitatively and quantitatively compared in Section 10.2. A discussion of the experimental results is given in Section 10.3.

The material presented in this chapter is partly taken from [SGZ20].

10.1 METHODS

Figure 10.1 gives an overview of the proposed framework for the extraction and comparison of gait parameters based on radar data as well as MoCap data utilizing GRFs. In the following, the individual processing steps will be described in detail for both domains.

10.1.1 *Radar Signal Processing*

Since the radar backscatterings of gait motions are highly non-stationary, we analyze the data in the joint time-frequency domain [Che19]. For human motion analysis, the spectrogram is typically utilized, which is obtained by the squared magnitude of the short-time Fourier transform (STFT), as given in Eq. (2.7). The radar data are recorded at a sampling frequency of 12.8 kHz and sub-sampled to 2.56 kHz. A Hamming window of length $M = 256$ is used with an overlap of 255 samples, and zero-padding is applied to obtain $K = 2048$ discrete frequency points. Thus, we obtain a frequency resolution of 40 Hz (here equivalent to 0.25 m/s) and a time resolution of 0.1 s. For real time processing, the granularity along the time and frequency axis may be decreased to reduce computation time. Spectrograms of a person walking at 1.1 m/s on a treadmill are given in Fig. 10.2, where Fig. 10.2a shows the case where the radar is positioned in front of, and Fig. 10.2b behind the test subject. The ordinates of the spectrogram indicate both, the measured Doppler frequency

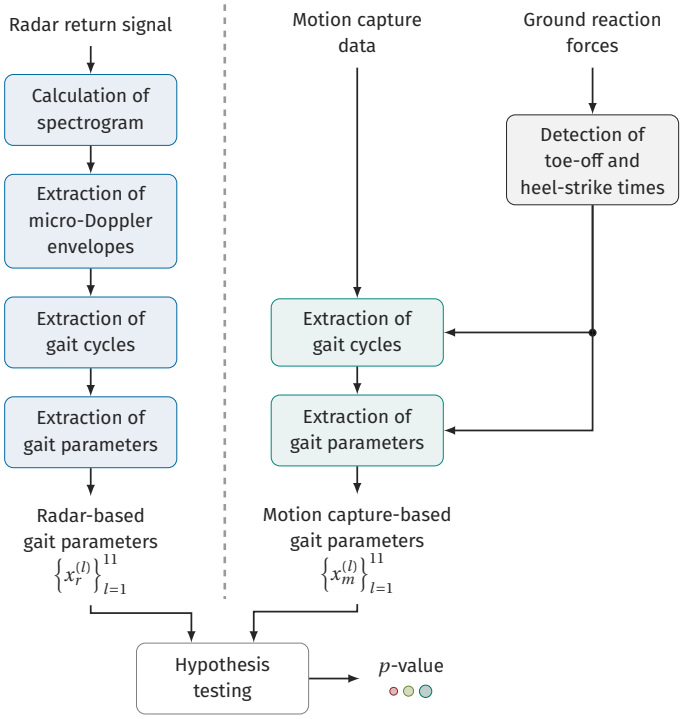

Figure 10.1: Overview of processing steps for the extraction and comparison of 11 biomechanical parameters based on radar micro-Doppler signatures (blue) and motion capture data (turquoise) utilizing ground reaction forces (gray).

and inferred radial velocity, which are related by Eq. (2.5). The radial velocity is defined in the direction of the propagation direction of the EM wave and assumes positive values when the target is moving away from the radar. Hence, the observed Doppler shift is positive and negative for toward and away from radar motions, respectively (compare ordinates in Figs. 10.2a and 10.2b). Here, we focus on those micro-Doppler signatures that arise from motions in the walking direction, i.e., positive and negative Doppler shifts for toward and away from radar motions, respectively. We note that the remaining micro-Doppler signatures are characteristic for treadmill walking and do not appear in this form in overground walking (compare spectrogram in Fig. 2.1). In the following, we will only refer to (the amplitude of) Doppler frequencies in the text, whereas, of course, for calculations the sign is considered where needed.

The background noise in the spectrogram is removed using an adaptive thresholding technique as explained in Section A.1.1. Based on the noise-reduced spectrogram, as shown in Fig. 10.2, the micro-Doppler envelope signal is extracted. For each time instant, we detect the highest Doppler frequency, where significant signal energy is present. By use of morphological operations, as detailed in Section 5.1.2, it is ensured that relevant signal components are considered even if lower Doppler components have less energy at a particular time instant. Examples of envelope signals are indicated in Fig. 10.2 by the black dashed lines.

To account for drifts in the sampling frequency of the systems, the MoCap and the radar data are synchronized prior to calculation of the spectrogram. For this, the micro-Doppler envelope is utilized. Analogously, a MoCap envelope is obtained by recording the maximal velocity among all recorded body parts for each time instant. Then, the maximum of the generalized cross-correlation

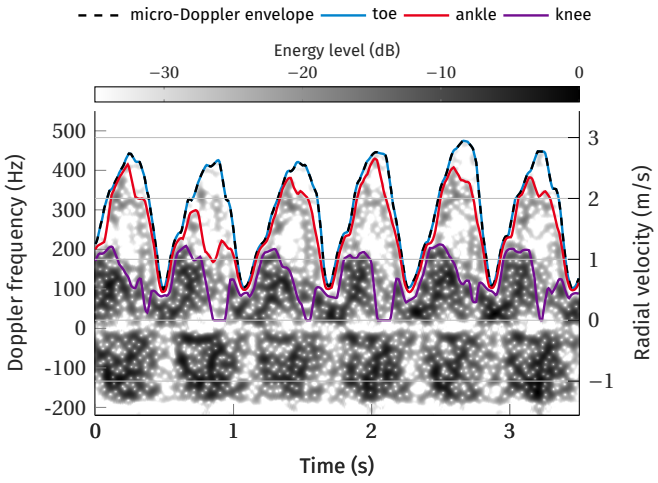

(a) front view

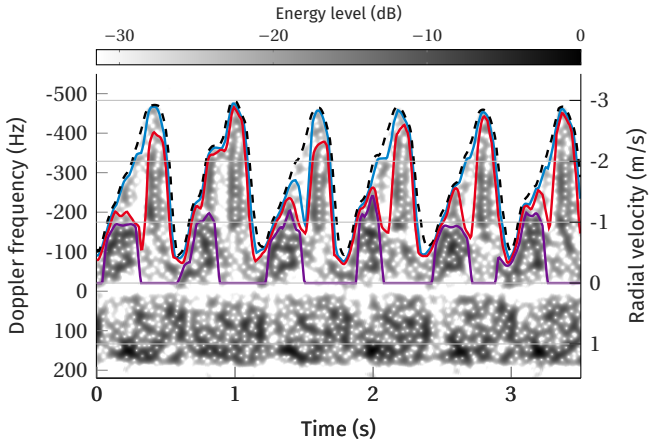

(b) back view

Figure 10.2: Examples of micro-Doppler signatures and extracted envelope signals. The black dashed lines are the standard micro-Doppler envelope signals, and the blue, red, and purple lines indicate the extracted envelope signals of toe, ankle and knee, respectively.

function between the radar and MoCap envelope is used to synchronize the signals in time, such that their correlation is maximal. Next, minima in the radar and the MoCap envelope signal are detected and their pair-wise time difference is calculated. Given these time differences as a function of the measurement duration, a robust linear least squares fit is employed to determine the drift in sampling frequency of the radar system compared to the MoCap system. The average drift over all measurements is found as 0.01 s/sample, and used to re-sample each radar measurement prior to calculation of the spectrogram. The synchronization of the radar and MoCap data is also utilized to determine which micro-Doppler step signature corresponds to which leg.

10.1.2 *Extraction of Micro-Doppler Envelope Signals*

The standard micro-Doppler envelope signal is frequently used to determine the maximal velocity of the swinging feet. Here, we utilize the procedure described in Section 6.1.1 to also extract the maximal velocity of other parts of

the lower limbs, i.e., ankle and knee. To do so, we adjust the noise threshold such that low energy components are neglected. The intuition is that the radar backscatterings from the ankle and the knee are expected to be stronger compared to those of the toe. Thresholding the micro-Doppler signatures using a proportionally higher noise threshold in micro-Doppler envelope signals that capture the ankle and knee velocities throughout a gait cycle. Examples of the extracted toe, ankle and knee envelope signals are shown in Fig. 10.2. The toe envelope signal is obtained using the adaptive noise threshold and 85 % of it for the front and back view, respectively. Using 85 % and 75 % of the adaptive noise threshold for the front and back radar, respectively, the ankle envelope signal is extracted. To extract the knee envelope signal, the spectrogram is thresholded at 55 % of the adaptive noise threshold for both radar perspectives. For further processing, the envelope signals are averaged over all gait cycles in a measurement. Examples of averaged micro-Doppler envelope signals for different lower limb joints are shown in Figs. 10.4c, 10.4f, 10.4i and 10.4l.

10.1.3 *Extraction of Gait Cycles*

Vertical GRFs are used to determine the toe-off and heel-strike times of each stride. First, the vertical GRF data are up-sampled to 1 kHz. In order to determine heel-strike events, a threshold of 400 N is employed [GSD+19]. Once the GRF exceeds this threshold, the heel-strike time is found by the time instant of the last preceding force value that falls below a threshold of 15 N, and is either greater than its subsequent force value or smaller than 1 N. To detect toe-off times, the GRFs are filtered with a zero-lag, second-order, low-pass Butterworth filter (cutoff frequency 20 Hz). Then, starting 100 ms after each heel-strike time, the first GRF value that falls below a threshold of 15 N is used to determine the toe-off time.

Figure 10.3 shows an example of vertical GRF for both legs at a treadmill speed of 1.1 m/s, where diamonds and circles indicate the toe-off and heel-strike times, respectively. A full gait cycle is defined from one heel-strike of one leg to the next one of the same leg. The duration of a gait cycle constitutes the

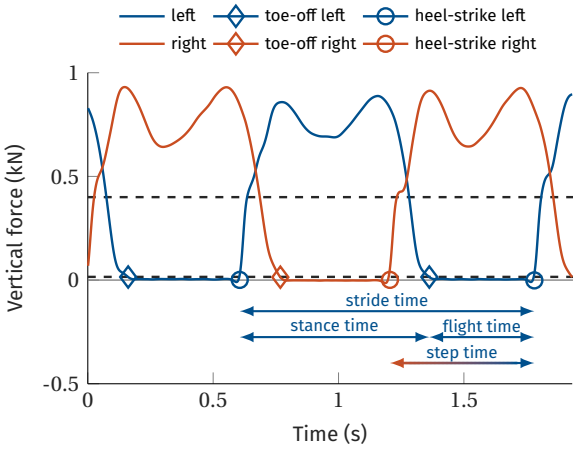

Figure 10.3: Example of vertical ground reaction forces at 1.1 m/s, where diamonds and circles mark the detected toe-off and heel-strike events, respectively. The dashed lines mark the thresholds used for toe-off and heel-strike detection. For the left foot, the stride time, stance time, flight time and step time are indicated.

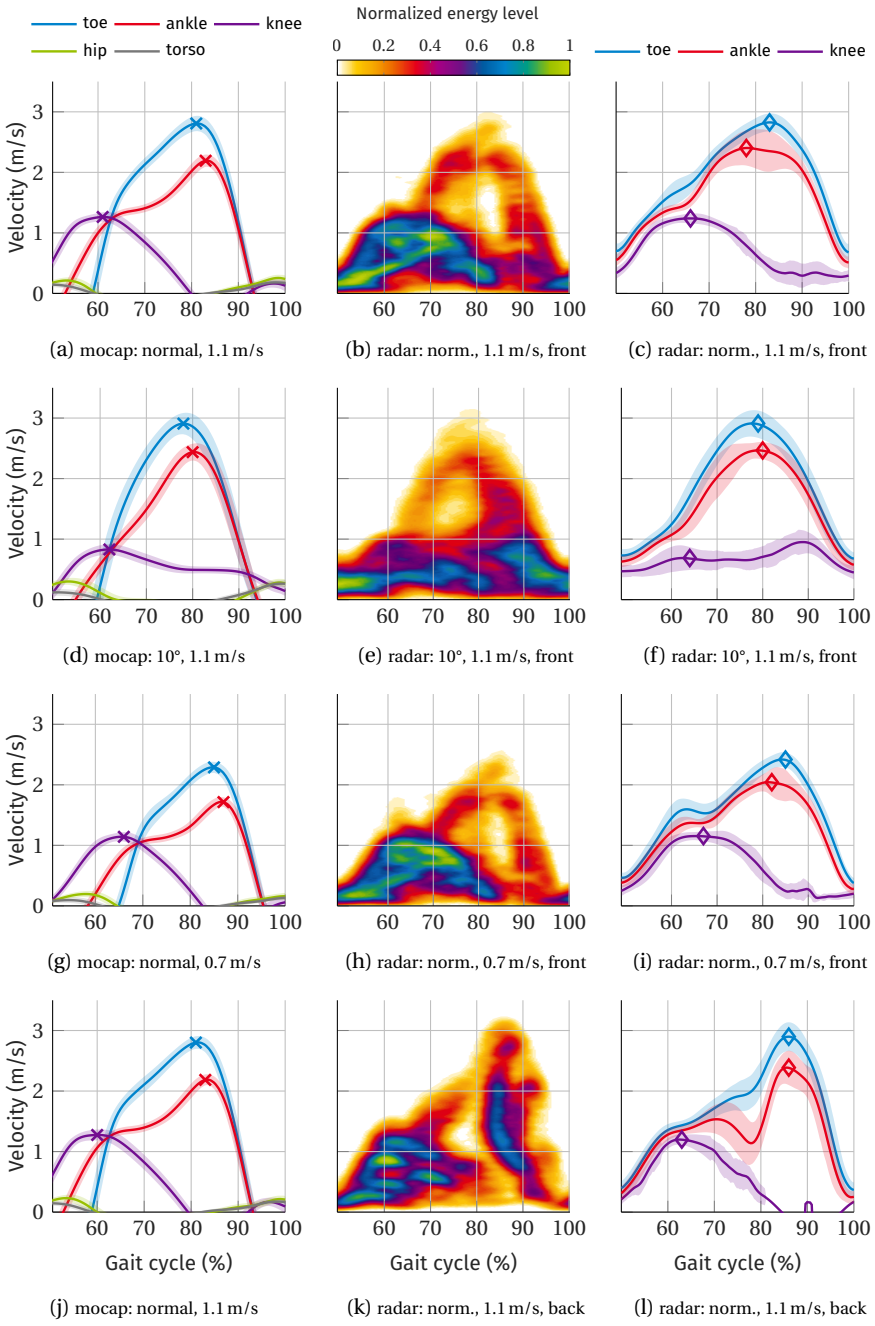

Figure 10.4: Motion capture (first column) and radar (second and third column) data of the right leg for one individual. The four columns represent the analyzed conditions: degree of knee angle confinement (no restriction vs. 10°), walking speed (1.1 m/s vs. 0.7 m/s), and radar positioning (front vs. back view). The time frame shown is the step time. In the first and third column, shaded areas indicate one standard deviation from the mean, and crosses and diamonds mark the maximal velocities of the lower limb joints for motion capture and radar data, respectively. The second column shows the averaged radar micro-Doppler signatures.

stride time. The stance time for one leg is given by the duration from heel-strike to toe-off time, where the flight time is determined by the time from toe-off to the next heel-strike. The step time is defined as the time between the heel-strike of one leg until the next heel-strike of the other leg. As indicated in Fig. 10.3, for the left leg, we define the step time as the duration from the heel-strike of the right leg to the heel-strike of the left leg.

In order to match the frequency of the GRF data, the MoCap data are upsampled to 1 kHz. The raw marker data are filtered using a zero lag, fourth-order, low-pass Butterworth filter (cutoff frequency 10 Hz). Then, GRFs of left and right leg are utilized to cut the MoCap data into individual gait cycles. The velocity information of each marker is averaged over all gait cycles in a measurement. The portions of the gait cycle that represent the step time of the right leg are shown in Figs. 10.4a, 10.4d, 10.4g and 10.4j. Hip and torso velocities are small since the test subjects were walking on a treadmill. The knee velocity generally reaches its maximum earlier in the gait cycle than the toe and ankle velocities. The latter exhibit higher maximal velocities compared to the knee.

To extract portions of the spectrogram that correspond to one gait cycle, the standard micro-Doppler envelop is utilized (see Fig. 10.2). Here, every second minimum in the micro-Doppler envelope signal defines the onset of a gait cycle for a particular leg. The so obtained micro-Doppler gait cycle signatures are averaged for each measurement. The resulting micro-Doppler signatures are less distorted and easier to interpret (visually). Examples of averaged micro-Doppler signatures for the right leg are shown in Figs. 10.4b, 10.4e, 10.4h and 10.4k.

10.1.4 *Definition of Flight Time*

The flight time of a foot is defined by the time duration between the toe-off time and the subsequent heel-strike of the same foot [GM17]. Since the radar system records the radial velocities of all body parts simultaneously, the flight time of a foot is generally not directly accessible from the radar micro-Doppler signatures, i.e., in the joint time-frequency domain, the time-varying Doppler shifts of a foot are obscured by those of other body parts. In general, it is a non-trivial task to separate these components [AAKS17]. Here, we propose to use the time instant at which the knee reaches its maximal velocity to indicate the beginning of the flight time, i.e., the toe-off time.

In order to justify this approach we show that the time instant of maximal knee velocity $t^{\text{moc}}_{\text{knee-max-v}}$ serves as a good approximation for the toe-off time $t^{\text{grf}}_{\text{toe-off}}$, where the former is obtained from MoCap data and the latter is determined based on vertical GRFs. For this, we analyze the time difference $t^{\text{grf}}_{\text{toe-off}} - t^{\text{moc}}_{\text{knee-max-v}}$, which is extracted for each gait cycle. Figure 10.5 shows the average differences for the right leg over all test subjects, where the error bars indicate the 95 % confidence interval for the mean. Here, the Gaussian assumption on the distribution of the average difference was verified empirically. For both, the slow and the fast walking speed, and for all conditions the average difference between the time instant of the maximal knee velocity and the toe-off time is small. The average differences range between 13 ms and 40 ms. Given the average flight time assumes 448 ms and 402 ms for 0.7 m/s and 1.1 m/s, respectively, the maximally expected error in flight time is approximately 9 % (40 ms) and 8 % (31 ms).

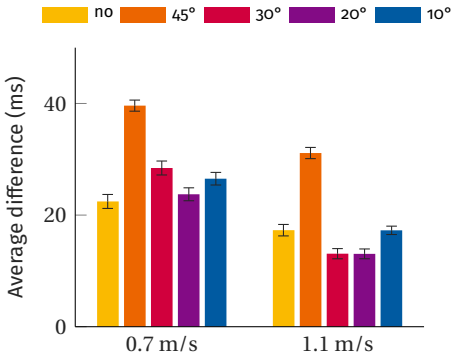

Figure 10.5: Average differences between the time instant of maximal knee velocity from motion capture data and the toe-off time from ground reaction forces for five different knee angle confinements. The error bars indicate the 95 % confidence interval for the average differences.

10.1.5 *Extraction of Gait Parameters*

In total, 11 gait parameters are considered. Where applicable, the kinematic meaning of each of these parameters is given first [GM17]. Then the extraction methods for GRF or MoCap and radar data are explained.

STRIDE TIME A full gait cycle is defined from one heel-strike to the next. The duration of a gait cycle is given by the stride time. Utilizing GRFs, the average time-span between two consecutive heel-strikes of the same leg yields the stride time. In case of radar data, every second minimum in the micro-Doppler envelope signal indicates the beginning of a new gait cycle. Thus, the average time between every second minimum serves as an estimate for the stride time.

STANCE TIME The stance time refers to the time duration that a foot is on the ground during a gait cycle. From GRFs, the stance time can be obtained as the average time between a heel-strike and subsequent toe-off event. Given radar data, the stance time is calculated by subtracting the flight time from the stride time.

FLIGHT TIME The flight time describes the length of the swing phase while taking a stride. Using GRFs, the flight time is defined from the toe-off time to the following heel-strike of the same leg. As described in Section 10.1.4, for the radar data, the flight time is defined from the time instant of maximal knee velocity to the end of the gait cycle.

STEP TIME The step time denotes the period of time taken for a step. Based on GRFs, the step time is defined from the heel-strike of one foot to the heel-strike of the following other foot. The step time is obtained by averaging the difference between two consecutive minima in the envelope signal. The averaged micro-Doppler signatures of full gait cycles are cut to two step signatures for the left and right foot based on the average step time of the first leg in the gait cycle.

CADENCE The cadence is typically defined as the number of steps per minute. For both, the GRF and radar data, the cadence is calculated based on the reciprocal of the average step time (in min).

STRIDE LENGTH The stride length describes the distance which is covered during one stride (or cycle). For both measurement systems, the stride length is calculated as the product of the stride time and the treadmill speed.

STEP LENGTH The step length describes the distance between successive heel-off events of the opposite feet. For both measurement systems, the step length is calculated as the product of the stride time and treadmill speed.

MAXIMAL FOOT VELOCITY Using MoCap data, the radial velocity of the toe marker is averaged over all gait cycles. The maximum of the averaged velocities yields the maximal foot velocity (see Figs. 10.4a, 10.4d, 10.4g and 10.4j). Given micro-Doppler signatures, the maximal foot velocity is determined by averaging the toe envelope signal over all gait cycles. The maximum of the averaged envelope signals yields the average maximal foot velocity (see Figs. 10.4b, 10.4e, 10.4h and 10.4k).

MAXIMAL ANKLE VELOCITY Similarly to the extraction of the maximal foot velocity, the maximal ankle velocity is given by the maximum of the average radial velocity of the marker positioned at the ankle (see Figs. 10.4a, 10.4d, 10.4g and 10.4j). In order to extract the average maximal ankle velocity from the radar data, the micro-Doppler envelope signal of the ankle is averaged over all gait cycles in a measurement. Its maximum gives the average maximal ankle velocity (see Figs. 10.4b, 10.4e, 10.4h and 10.4k).

MAXIMAL KNEE VELOCITY The maximal knee velocity is extracted from the MoCap data by finding the maximal average velocity of the knee marker in the y-direction (see Figs. 10.4a, 10.4d, 10.4g and 10.4j). Then, the knee envelope signal is found, as shown in Fig. 10.2, and averaged over all gait cycles. Its maximum gives the average maximal knee velocity (see Figs. 10.4b, 10.4e, 10.4h and 10.4k). In case of the knee envelope, the first local maximum is considered opposed to the global maximum (see e.g. Fig. 10.4f).

TIME INSTANT OF MAXIMAL KNEE VELOCITY Having detected the maximal knee velocity in the MoCap and radar data, respectively, the corresponding time instants during the gait cycle serve as an additional characteristic to describe the degree of abnormality. As explained in Section 10.1.4, for the radar data, we use the time instant of maximal knee velocity as the onset of the flight time.

10.1.6 *Hypothesis Testing*

To evaluate the accuracy of the radar system in measuring the aforementioned gait parameters in comparison to the MoCap system, we employ hypothesis testing. More specifically, we aim to show that there is no significant difference in measuring the gait parameters using radar compared to using motion capturing. For this, we resort to the Wilcoxon signed rank test, which is a non-parametric, paired, two-sided test for the null hypothesis that the differences come from a distribution with zero median [GC11]. The test is performed *individually* for each gait parameter, knee angle restriction, viewing angle of the radar and walking speed under analysis, such that in total $N_t = 220$ tests are performed. Let $X_{r,i}$ and $X_{m,i}$ be *one* of the gait parameters given in Section 10.1.5 obtained through radar and motion capturing, respectively, and $i = 1,\dots,19$ refer to the 19 test subjects. We consider the random sample of pairs $(X_{r,i}, X_{m,i})$ and form the differences $D_i = X_{m,i} - X_{r,i}$. Then, we test the hypothesis

$$\mathcal{H}_0 : \quad M_D = 0\,, \tag{10.1}$$

where M_D is the median of the population of differences D_i. Given observations $x_{m,i}$ and $x_{r,i}$, $i = 1,\ldots,19$,[1] we form the differences $d_i = x_{m,i} - x_{r,i}$ and calculate the sum of signed ranks. Based on this test statistic, we calculate the p-value for a confidence level of 95 % (confidence coefficient $\alpha = 0.05$). The p-value gives the probability of accepting the alternative hypothesis although the null hypothesis is true. Thus, in a first step, we test the hypotheses $\mathcal{H}_{(1)}, \mathcal{H}_{(2)}, \ldots, \mathcal{H}_{(N_t)}$ by comparing the corresponding p-values to α, where $\mathcal{H}_{(j)}$ denotes the null hypothesis for the jth test and $N_t = 220$. For $p \leq 0.05$, we reject the null hypothesis.

In a second step, we control the expected proportion of falsely rejected hypotheses by applying the Benjamini-Hochberg procedure which controls the false discovery rate [BH95]. For this, rank ordering of the calculated p-values is applied, such that $p_{(1)} \leq p_{(2)} \leq \cdots \leq p_{(N_t)}$. Then, we find $k = \{\max j \mid p_{(j)} \leq \frac{j}{N_t}\alpha\}$. Thus, through the BH procedure, we obtain $p^* := p_{(k)}$, which serves as a significance threshold for the p-values, i.e., for $p \leq p^*$ the null hypothesis is rejected (●). For $p > p^*$ we accept the null hypothesis (●).

Since very large p-values generally indicate high confidence in the null hypothesis, we highlight p-values with $p > 0.8$ (●).

10.2 EXPERIMENTAL RESULTS

Table 10.1 concisely presents the results of the applied Wilcoxon signed-rank test and subsequent BH procedure. The latter yields $p^* = 0.0057$ for the available data. From Table 10.1, it can be seen that the radar-based estimates for the stride time, step time, cadence, stride length and step length generally agree with the parameters obtained from MoCap data, i.e., the respective differences are small. This holds for both treadmill speeds as well as for both radar positions. The stance and flight time are accurately measured by the radar system for all conditions at the slow treadmill speed (0.7 m/s). At 1.1 m/s and when the radar has a back view on the target, both parameters can reliably be detected for all conditions except for unconstrained gait. However, both parameters are difficult to be extracted from the radar data at 1.1 m/s when the radar is positioned in front of the subject. The maximal toe, ankle and knee velocities can generally be extracted accurately from the radar data. Toe and ankle velocities are not correctly extracted in two out of the 20 scenarios, knee velocities in five. The time index of maximal knee velocity cannot be reliably detected using radar when the radar is positioned in front of the subject. However, when the radar is positioned behind the subject, the parameter can be reliably obtained from the radar data, except for the case of unconstrained gait at 1.1 m/s.

Figure 10.6 shows the estimated median values of the differences d_i and corresponding 95 % confidence intervals for the analyzed gait parameters. In order to put the amplitudes of the median of differences into relation, Table A.2 shows the corresponding mean values of the gait parameters. Fig. 10.6a indicates that the stride time can be measured more accurately by the radar for the fast walking speed. Accordingly, the median of differences for the stride length are smaller for 1.1 m/s, as shown in Fig. 10.6f. The relative measurement errors for these two gait parameters are very small. From Fig. 10.6d, it can be seen that, similar to the stride time, the step time is more accurately measured by the radar at 1.1 m/s. Similarly, the derived step length reveals small measurement errors at both walking speeds, as shown in Fig. 10.6g. The median values of

1 18 for the cases of no knee angle confinement, and 45°

Table 10.1: Results of testing the null hypothesis that the median of the differences in the parameter measured by the motion-capture and radar system is zero. For each treadmill speed (0.7 m/s, 1.1 m/s) and radar position (front, back), the results are shown for increasing knee restriction from left to right (no, 45°, 30°, 20°, 10°). The red dot symbol (●) indicates that the median is statistically significantly different from zero ($p < 0.0057$). The green (●) and turquoise (●) circles indicate that the null hypothesis cannot be rejected with $p > 0.0057$ and $p > 0.8$, respectively.

	0.7 m/s		1.1 m/s	
	front	back	front	back
1) stride time	○○○○○	○○○○●	○○○○○	○○○○●
2) stance time	●○○○○	○○○○●	●●●●○	○○○○○
3) flight time	●○○○○	○○○○●	●●●●○	○○○○○
4) step time	○●○○○	○○○○○	○○○○○	●○○○○
5) cadence	●○○○○	○○○○○	○○●○○	○○○○○
6) stride length	○○○○○	○○○○●	○○○○○	○○○○●
7) step length	○●○○○	○○○○○	○○○○○	●○○○○
8) max. foot velocity	●○○○●	○○●○●	○○○○○	○○○●●
9) max. ankle velocity	○○○○○	●○●○○	●○○○○	○●○●●
10) max. knee velocity	○●○○●	●○○○●	●○○●○	●○○○○
11) time max. knee vel.	●●○○●	○○○○●	●●●●○	●○○○○

differences for the stance time and the flight time are shown in Figs. 10.6b and 10.6c, respectively. From Fig. 10.6k, we can see that the front radar overestimates the time index of maximal knee velocity more severely in case of the fast treadmill speed compared to the slow one, which leads to a negative median value of differences. Thus, at 1.1 m/s the stance time is overestimated by radar, while consequently the flight time is underestimated. Fig. 10.6e shows that the cadence can be measured by the radar with high accuracy, since the median of differences assume very small values. As shown in Figs. 10.6h to 10.6j, the maximal velocity of the toe, ankle and knee reveal absolute median values that are smaller than 0.3 m/s. When the radar has a back view on the subject, the maximal knee velocity is measured less reliably, which can be concluded from the large confidence intervals in Fig. 10.6j.

Analyzing the last parameter in more detail, Fig. 10.7 reveals the decreasing maximal knee velocities for an increasing degree of knee angle restriction (see also parameter 10 in Table A.2). Based on the front radar, the radar measurements are more accurate for all degrees of knee angle confinement with only a few outliers, as shown in Figs. 10.7a and 10.7c. Figs. 10.7b and 10.7d show that the radar measurements are less accurate when observing the subject from behind such that the obtained differences are more dispersed.

10.3 DISCUSSION

Using MoCap data, we validated existing and new methods for extracting a variety of medically relevant gait parameters from experimental radar data.

Utilizing the standard micro-Doppler envelope, five spatiotemporal parameters related to rhythm (stride time, step time, cadence) and pace (stride length, step length) are extracted from the radar measurements. For these parameters, the differences between the values obtained through radar and motion capturing are close to zero for all analyzed conditions.

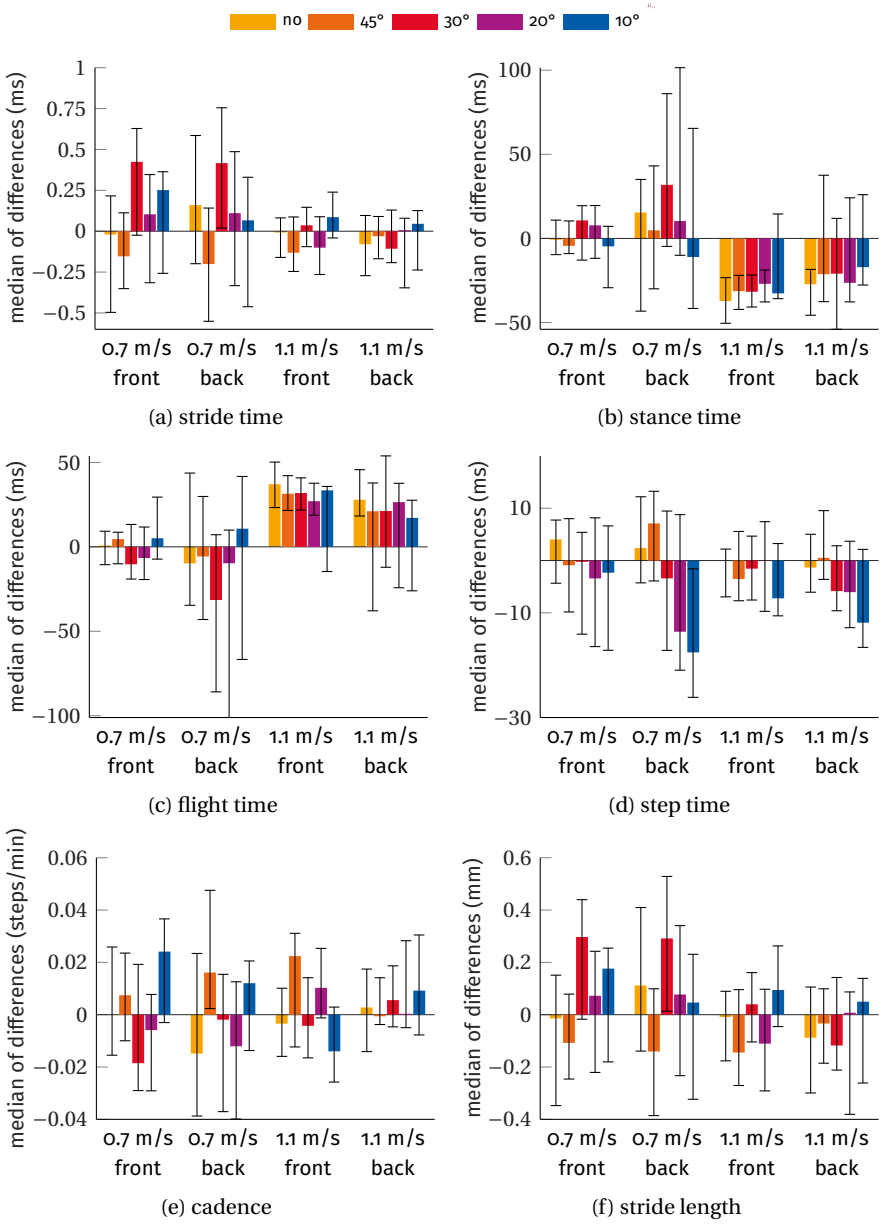

(a) stride time (b) stance time

(c) flight time (d) step time

(e) cadence (f) stride length

Figure 10.6: Detailed results for the analyzed gait parameters. The bars indicate the median of differences for the five different knee angle restrictions, the two treadmill speeds and the two radar positions. The error bars indicate the 95 % confidence intervals of the median. If the confidence intervals include the zero median, we cannot reject the null hypothesis that the median of differences is zero ($p \leq 0.05$).

Additional envelopes are extracted from the micro-Doppler signatures to measure kinematic parameters, i.e., the maximal velocity of the toe, ankle and knee joint during walking. For different knee angle confinements, the velocities measured by the radar system agree with those obtained using motion capturing in 51 out of the 60 analyzed cases (85 %). In particular, the changes in maximal knee velocity due to the restriction of the knee's motions are also captured by the radar. Here, the thresholds for extracting the envelope signals were found empirically. In general, the appearance of the micro-Doppler signatures depends on the subject's stature (height, mass), interfering noise component due to, e.g., multi-path, and transmitting power of the radar system, which can

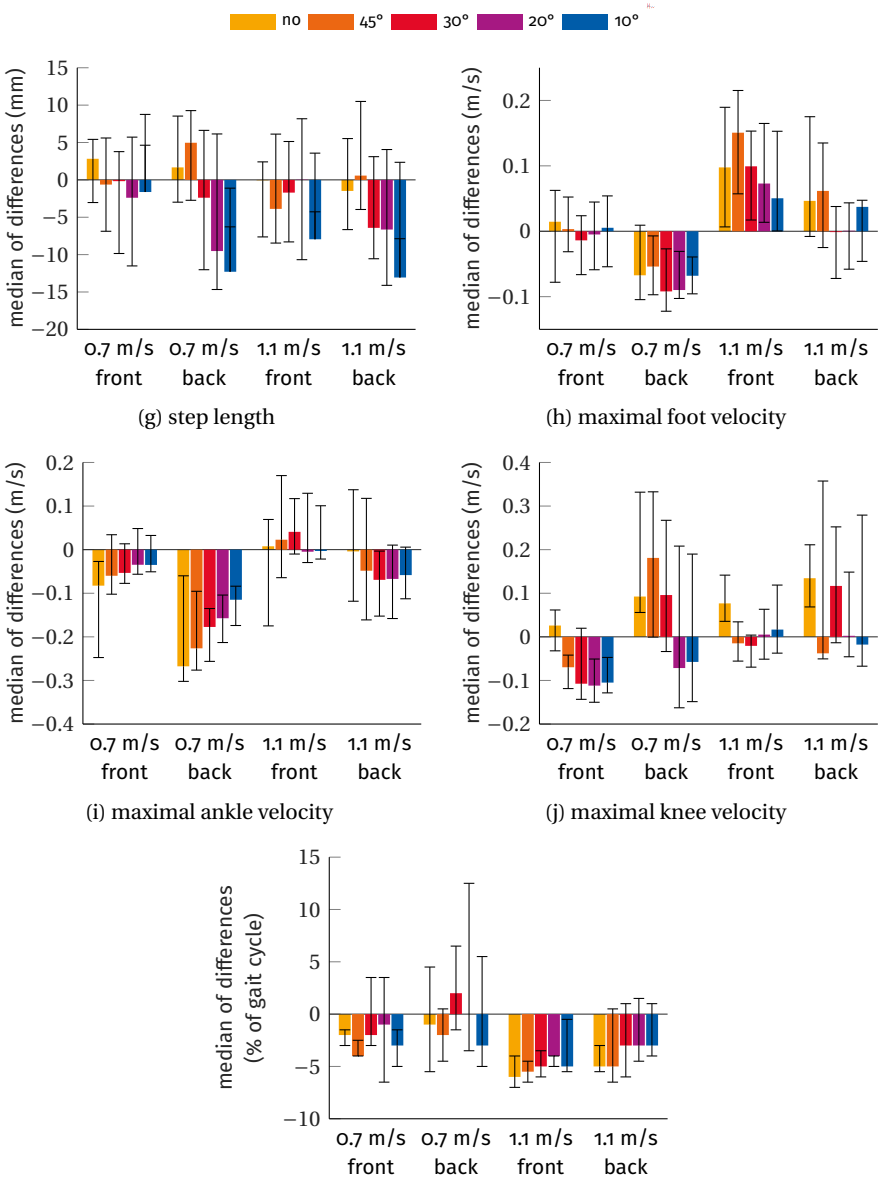

(g) step length

(h) maximal foot velocity

(i) maximal ankle velocity

(j) maximal knee velocity

(k) time instant of maximal knee velocity

Figure 10.6: Detailed results for the analyzed gait parameters (cont'd). The bars indicate the median of differences for the five different knee angle restrictions, the two treadmill speeds and the two radar positions. The error bars indicate the 95 % confidence intervals of the median. If the confidence intervals include the zero median, we cannot reject the null hypothesis that the median of differences is zero ($p \leq 0.05$).

result in different thresholds. Here, we note that the presented micro-Doppler signatures might be affected by the backscatterings from the orthosis. However, preliminary tests showed that the differences to not wearing an orthosis are negligible.

The knee's micro-Doppler envelope is further utilized to detect the time instant of maximal knee velocity. Due to the proposed definition of the flight time (see Section 10.1.4), the radar-based stance and flight time measurements rely on accurate detection of the time instant at which the knee reaches its maximal velocity during the gait cycle. Since radar micro-Doppler signatures are composed of overlaying reflections from different body parts, the knee's

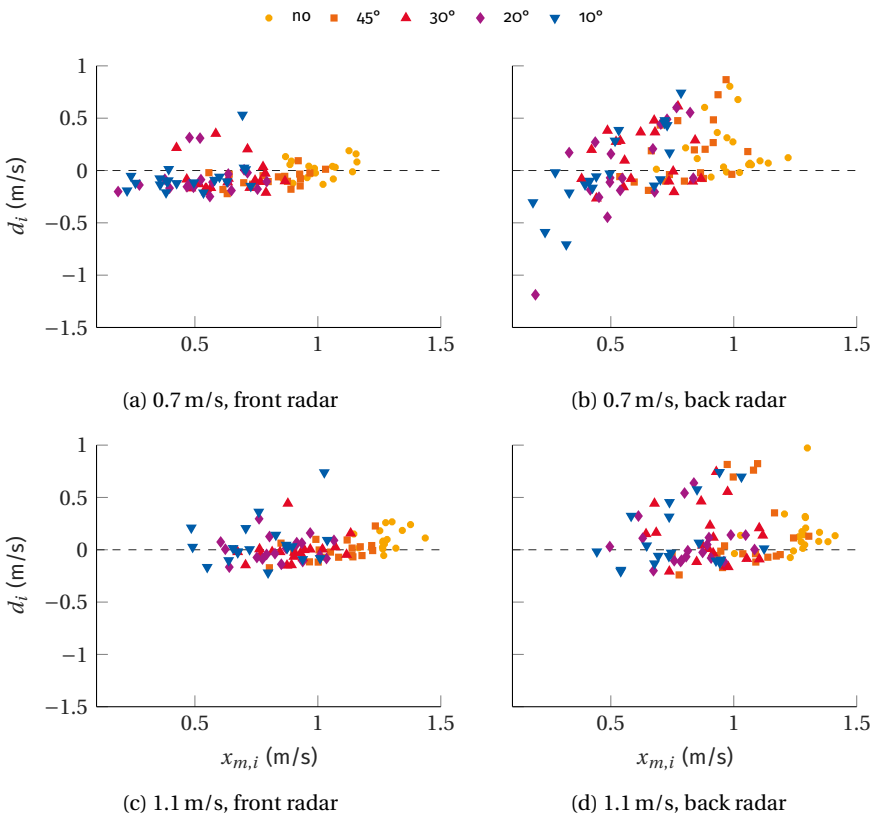

(a) 0.7 m/s, front radar

(b) 0.7 m/s, back radar

(c) 1.1 m/s, front radar

(d) 1.1 m/s, back radar

Figure 10.7: Decreasing maximal knee velocity for increasing knee angle confinement. The scatter plot shows the differences between motion capture and radar measurements ($d_i = x_{m,i} - x_{r,i}$) against the measured values using motion capturing ($x_{m,i}$). The black dashed line indicates that there is no difference between the value measured by the radar and the motion capture system.

signatures is obscured by backscatterings from the upper leg (mid upper leg to knee joint), which exhibits similar velocities as the knee joint while reflecting more energy of the EM wave. From Figs. 10.4b, 10.4e and 10.4h, it can be seen that in case the radar has a front view on the target, the toe and ankle signatures can be identified by the red areas that exhibit a sinusoidal shape between 55 % to 100 % of the gait cycle. When compared to Figs. 10.4a, 10.4d and 10.4g, the measured radial velocities generally align well with the recorded velocities by the MoCap system. However, when that radar is positioned behind the subject, the knee's signature does not exhibit the shape as proposed by the MoCap data, but appears to be much more complex, as shown in Fig. 10.4k. Here, an almost vertical line, also referred to as spike signature, appears at approximately 85 % of the gait cycle in Fig. 10.4k (see also Section 5.1.1). Thus, the precise measurement of the knee joint velocity during walking remains challenging using micro-Doppler signatures. In order to extract kinematic parameters more reliably from radar data, averaged micro-Doppler signatures, such as the ones shown in Figs. 10.4b, 10.4e and 10.4h, should be used as they are less corrupted by noise and hence more conclusive. Further, model-based approaches could be considered that are specifically designed to extract kinematic parameters by incorporating prior knowledge.

The presented results indicate the feasibility of using Doppler radar for unobtrusively measuring a variety of biomechanical parameters that can be of

use for basic gait analysis. The proposed methods need to be further evaluated using realistic in-home data without a treadmill and a larger clinical population. In general, treadmill walking differs from walking overground [HWI+16]. However, in terms of the here investigated gait parameters, i.e., spatiotemporal parameters and lower limb kinematics in the sagittal plane, studies suggest that there are only few or no differences (in mean values) between treadmill and overground walking (see e.g. [HWI+16; LH08]). In this regard, we note that most *spatiotemporal* parameters can also be extracted from realistic radar data from overground walking, as e.g. demonstrated by Wang *et al.* [WSRC14]. However, the extraction of *kinematic* parameters is more sensitive to the distance of the person to the radar and the viewing angle of the radar (vertical/horizontal) on the subject, who might not walk in a 0° angle to the radar's LOS Thus, while this work focused on the lower limbs' motions only, future studies should reevaluate the positioning of the radar, i.e., its distance to the subject and height, which directly affects the appearance of the micro-Doppler signatures. Further studies may also consider gait abnormalities that impact a larger number of gait parameters (more drastically). For example, opposed to only restricting the knee angle during walking, the ankle's motion could be constrained, too. This could emulate trans-tibia and trans-femoral amputees, respectively, where the latter induces a change in gait parameters compared to a healthy leg [NWD+03].

Finally, though the measured *absolute* values obtained through radar measurements ought not be sufficiently accurate for professional gait analysis (yet), we showed that radar is capable of sensing small changes in gait parameters induced by the orthosis, which can be of interest for assessing the *relative* progress of diseases affecting the gait [GTK+17]. Additionally, asymmetry measures could be calculated and used to detect and quantify gait impairments, as suggested in, e.g., [GM17; NWD+03]. Gait asymmetry measures typically depend on the difference in gait parameters from the left and right leg, rather than on their absolute values. Based on experimental radar measurements of 6 s duration, the gait asymmetry of four gait-impaired individuals was successfully detected in [SRZA19]. A sequential detection approach for increasing recognition speed and thus practicability, was presented in [SAZ19]. Further, deep learning methods could be utilized to automatically learn the relation between biomechanical parameters and radar micro-Doppler stride representations, without relying on specifically designed feature extraction methods. For example, Hannik *et al.* [HKP+17] proposed such a framework to extract eight spatiotemporal stride parameters from inertial sensors using deep convolutional neural networks. Hence, a radar-based long-term gait analysis system could provide useful information, e.g., on the progress of recovery from an injury in rehabilitation, to assist medical practitioners and physiotherapist in therapy.

11 ESTIMATION OF LOWER LIMB ANGULAR KINEMATICS

In this chapter, we move beyond discrete biomechanical measures to estimate the hip-knee cyclogram from radar backscattering. As described in Section 3.2, the cyclogram is obtained by plotting the hip vs. knee angles for different time instants [Gos98]. Unlike discrete measures, such as the cadence, stride length, and maximal foot velocity, the cyclogram reveals kinematic information over the entire gait cycle and enables a joint analysis of two leg joints. These aspects allow for better identification of subtle changes in the gait profile.

In order to estimate the hip and knee angle trajectories from the radar data, we formulate a mapping F of the ith joint angle θ_i parameterized by $\boldsymbol{\Theta}_i$ to the observed Doppler shift f^{D} of the respective body part (knee and ankle), i.e.,

$$f^{\mathrm{D}}(t;\boldsymbol{\Theta}_i) = F(\theta_i(t;\boldsymbol{\Theta}_i)).$$

To model θ_i, we use the bilateral symmetric model [YNC04], whose parameters directly reflect biomechanical mechanisms. In combination with the commonly used global human walking model by Boulic, Magnenat-Thalmann, and Thalmann [BTT90], we formulate F for the knee and the ankle joints. Thus, we obtain parametric models for the time-varying Doppler frequency of the respective body parts (knee and ankle). Using experimental motion capture (MoCap) data of 19 individuals walking with different degrees of knee angle confinements, we validate the proposed models and demonstrate their ability to account for gait abnormalities. Thus, we extend existing gait models by introducing additional degrees of freedom to account for knee angle restrictions. This aids in simulating radar micro-Doppler gait signatures with a large intra-class variance. In order to estimate the unknown parameter vector $\boldsymbol{\Theta}_i$ from experimental radar micro-Doppler signatures, we resort to TFRs and the Hough transform for pattern recognition. The Hough and Radon transforms have been successfully applied to estimate the micro-Doppler signature parameters in, e.g., [BL96; CZA08; SDTP15; GM19].

Next, Section 11.1 introduces the radar signal model, Boulic's global human walking model, and models for the lower limbs angular kinematics. The methodology of the proposed approach utilizing the Hough transform is given in Section 11.2. Section 11.3 presents the results based on real radar data of 19 test subjects. A discussion of the experimental results is given in Section 11.4.

11.1 SIGNAL MODELS

11.1.1 *Radar Signal Model*

As outlined in Section 2.2, the radar backscattering of a non-rigid target can be modeled by a multi-component frequency modulated signal given by

$$s(t) = \sum_i \rho_i e^{j\Phi_i(t;\boldsymbol{\Theta}_i)}, \tag{11.1}$$

where ρ_i is the path loss of the ith scattering component, and $\phi_i(t;\boldsymbol{\Theta}_i)$ describes the phase functions w.r.t. time which is parameterized by a parameter vector $\boldsymbol{\Theta}_i$. The IF of component i is defined as

$$f_i(t;\boldsymbol{\Theta}_i) = \frac{1}{2\pi}\frac{\mathrm{d}\Phi_i(t;\boldsymbol{\Theta}_i)}{\mathrm{d}t}. \tag{11.2}$$

In considering the radar data, the IF describes the time-varying Doppler frequency, which is proportional to the observed radial velocity v_i of the ith target component

$$v_i(t;\boldsymbol{\Theta}_i) \approx -f_i^{\mathrm{D}}(t;\boldsymbol{\Theta}_i)\frac{\lambda_c}{2}, \tag{11.3}$$

where λ_c is the wavelength of the transmitted EM wave. In the above equation, the radial velocity of the target is assumed to be much smaller than the propagation speed of the EM wave. When monitoring human motions with radar, the IF of the individual components is not necessarily linear in the parameter vector $\boldsymbol{\Theta}$. Specifically, the IF of the lower limb joints during walking can be modeled by nonlinear functions w.r.t. the parameter vector $\boldsymbol{\Theta}$, as described in the next sections.

11.1.2 *Boulic Global Human Walking Model*

In [BTT90], Boulic, Magnenat-Thalmann, and Thalmann proposed a global human walking model, which was derived from biomechanical experimental data. In this model, all dynamics can be described based on two input parameters, namely, the walking velocity and the height of the person. Since lateral motions of the lower limbs during walking are relatively small, we focus on motions in the sagittal plane, i.e., y-z-plane as indicated in Fig. 9.1. Assuming the radar system is positioned at knee height, we focus on the y-component only, and describe the horizontal displacement of the knee joint by

$$s_{\mathrm{knee},y}(t;l_{\mathrm{ul}}) = l_{\mathrm{ul}}\sin(\theta_{\mathrm{hip}}(t)), \tag{11.4}$$

where $l_{\mathrm{ul}} = 0.245\,h$ is the upper leg length with h being the height of the person (in m), and $\theta_{\mathrm{hip}}(t)$ describes the time-dependent hip angle.From Eq. (11.4), the radial velocity of the knee can be obtained by

model for radial knee velocity

$$v_{\mathrm{knee}}(t;l_{\mathrm{ul}}) \approx \frac{\mathrm{d}s_{\mathrm{knee},y}(t;l_{\mathrm{ul}})}{\mathrm{d}t} = l_{\mathrm{ul}}\cos(\theta_{\mathrm{hip}}(t))\,\dot{\theta}_{\mathrm{hip}}(t), \tag{11.5}$$

where $\dot{\theta}_{\mathrm{hip}}$ is the derivative of the hip angle function w.r.t. time.

Similarly, we can find an expression for the radial velocity of the ankle. Let α denote the viewing angle (elevation) of the radar on the ankle (see Fig. 9.1), the radial velocity of the ankle is given by

model for radial ankle velocity

$$v_{\mathrm{ankle}}(t;l_{\mathrm{ul}},l_{\mathrm{ll}}) \approx \frac{\mathrm{d}s_{\mathrm{ankle},y}(t;l_{\mathrm{ul}},l_{\mathrm{ll}})}{\mathrm{d}t}\cos(\alpha) + \frac{\mathrm{d}s_{\mathrm{ankle},z}(t;l_{\mathrm{ul}},l_{\mathrm{ll}})}{\mathrm{d}t}\sin(\alpha), \tag{11.6}$$

where

$$\begin{aligned} s_{\mathrm{ankle},y}(t;l_{\mathrm{ul}},l_{\mathrm{ll}}) &= \begin{bmatrix} \cos(\theta_{\mathrm{hip}}(t)) \\ -\sin(\theta_{\mathrm{hip}}(t)) \end{bmatrix}^{\top} \begin{bmatrix} l_{\mathrm{ll}}\sin(\theta_{\mathrm{knee}}(t)) \\ -l_{\mathrm{ul}} - l_{\mathrm{ll}}\cos(\theta_{\mathrm{knee}}(t)) \end{bmatrix}, \\ s_{\mathrm{ankle},z}(t;l_{\mathrm{ul}},l_{\mathrm{ll}}) &= \begin{bmatrix} \sin(\theta_{\mathrm{hip}}(t)) \\ \cos(\theta_{\mathrm{hip}}(t)) \end{bmatrix}^{\top} \begin{bmatrix} l_{\mathrm{ll}}\sin(\theta_{\mathrm{knee}}(t)) \\ -l_{\mathrm{ul}} - l_{\mathrm{ll}}\cos(\theta_{\mathrm{knee}}(t)) \end{bmatrix} \end{aligned} \tag{11.7}$$

describe the position of the ankle joint in y- and z-direction, respectively, $l_{\mathrm{ll}} = 0.246\,h$ is the lower leg length, and $\theta_{\mathrm{knee}}(t)$ is the time-dependent knee angle.

11.1.3 *Angular Kinematics of Lower Limbs*

From Eqs. (11.5) and (11.6) we see that the knee and ankle velocities can be expressed as functions of the time-varying hip and knee angles. The latter are defined as shown in Fig. 11.1, where the hip angle is measured w.r.t. the vertical axis, while the knee angle is given relative to the thigh rotation (see also Section 3.2).

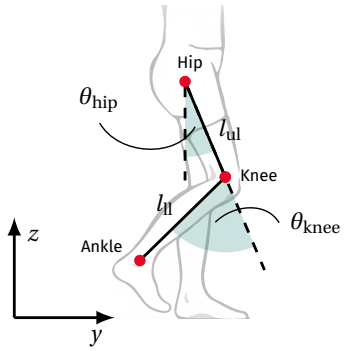

Figure 11.1: Definition of the hip and knee angles. The red circles represent the markers for motion capturing of the hip, knee, and ankle joints. (illustration partly adapted from [Lip06], own labels)

11.1.3.1 *Lower Limb Joint Angles According to Boulic*

When focusing on the lower limb joints, Boulic's walking model is based on the flexing functions of the ankle, knee and hip joints. In order to obtain the respective angle trajectories, five, four and three control points, respectively, are fitted via spline interpolation [BTT90; Che19]. The control points were found empirically and depend on the relative walking velocity $v_{\text{rel}} = \frac{v_0}{h_{\text{hip}}}$ [m/s], where v_0 is the walking speed, i.e., the speed of the treadmill in our case, and $h_{\text{hip}} = 0.491h$ is the dimensionless value of the hip height. An adjustment for modeling gait abnormalities is not straight forward, since the control points to not directly relate to the underlying biomechanics during walking. Examples of lower limb joint angles according to Boulic are given in, e.g., Fig. 11.5.

11.1.3.2 *Parameterization of Lower Limb Joint Angles*

The movement of the legs during walking can be modeled as two penduli joint in series [YNC04]. According to the bilateral symmetric model, the hip and knee angle trajectories during step time can be modeled as [YNC04]

bilateral symmetric model

$$\begin{aligned}\theta_{\text{hip}}(t; a_{\text{h}}, b_{\text{h}}, c_{\text{h}}, f_{\text{h}}) &= a_{\text{h}} \cos(2\pi f_{\text{h}} t + b_{\text{h}}) + c_{\text{h}} \\ \theta_{\text{knee}}(t; a_{\text{k}}, b_{\text{k}}, c_{\text{k}}, f_{\text{k}}) &= a_k \sin^2(2\pi f_{\text{k}} t + b_{\text{k}}) + c_{\text{k}}\end{aligned} \tag{11.8}$$

where $\{a_{\text{h}}, b_{\text{h}}, c_{\text{h}}, f_{\text{h}}\}$ and $\{a_{\text{k}}, b_{\text{k}}, c_{\text{k}}, f_{\text{k}}\}$ are the parameters for the hip and knee angle, respectively. Here, a describes the amplitude of the hip/knee rotation, i.e., the amount of extension/flexion of the upper/lower leg, f is the swing frequency of the upper/lower leg, b is a phase shift, and c is an offset. Using Eq. (11.8), we can express the radial velocity of the knee and ankle, i.e., Eqs. (11.5) and (11.6), as $v_{\text{knee}}(t; \boldsymbol{\Theta}_{\text{hip}}, l_{\text{ul}})$ and $v_{\text{ankle}}(t; \boldsymbol{\Theta}_{\text{hip}}, \boldsymbol{\Theta}_{\text{knee}}, l_{\text{ul}}, l_{\text{ll}})$, respectively, with $\boldsymbol{\Theta}_{\text{hip}} = \left[a_{\text{h}}, b_{\text{h}}, c_{\text{h}}, f_{\text{h}}\right]^\top$, and $\boldsymbol{\Theta}_{\text{knee}} = \left[a_{\text{k}}, b_{\text{k}}, c_{\text{k}}, f_{\text{k}}\right]^\top$.

11.2 METHODOLOGY

In Fig. 11.2, the general processing steps for the estimation of lower limb angular kinematics from radar data are shown. Here, MoCap data is utilized to validate lower limb kinematic models. In the following, the individual processing steps for the radar data will be described in more detail.

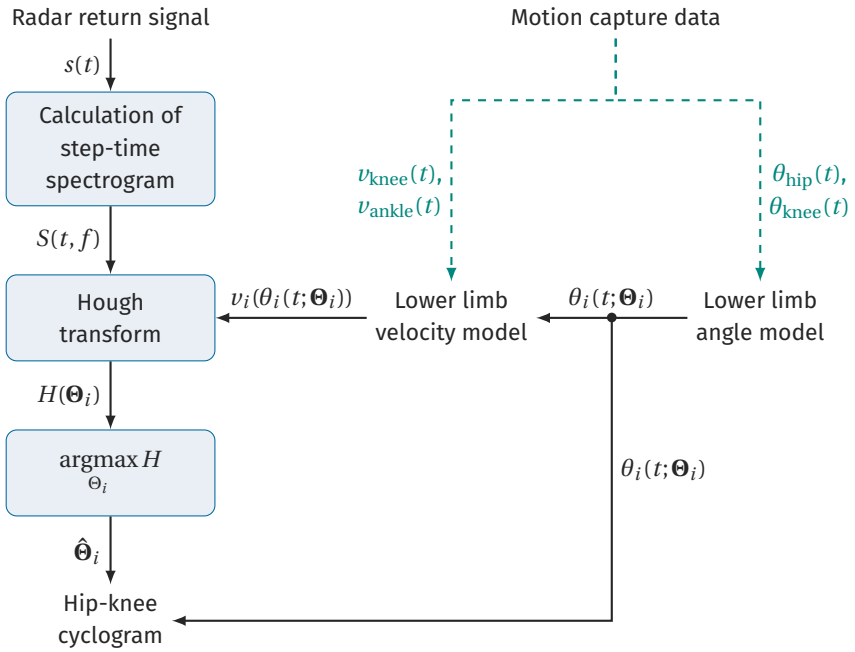

Figure 11.2: Processing steps for the estimation of biomechanical parameters based on radar micro-Doppler signatures and motion capture data utilizing ground reaction forces.

11.2.1 *Experimental Data Set*

Hereafter, only a subset of the experimental data outlined in Chapter 9 is considered, namely, toward radar motions recorded by the radar having a front view on the person (compare Fig. 9.1). Further, as in Chapter 10, only data of the right, i.e., restricted leg is utilized. It is noted that while the radar and MoCap data were recorded simultaneously, the systems were not synchronized during data collection, but the data were synchronized in post-processing as described in Section 10.1.1.

11.2.2 *Step Time Spectrograms*

Given the recorded radar backscattering signal $s(t)$ sampled at 2.56 kHz, we calculate the spectogram according to Eq. (2.7), where a Hamming window of length $M = 256$ samples and $K = 2048$ discrete frequency points are used. Since we rely on the micro-Doppler information, we focus on the step time, which includes the swing phase of the leg. The step time is estimated from the radar data as described in Section 10.1.5. Figures 11.3a and 11.3d shows examples of averaged micro-Doppler step signatures ($\bar{\mathrm{S}}$) for the right leg of one individual. The average was performed over 100 s measurement and the amplitude was normalized to the range of $[0, 1]$ afterwards.

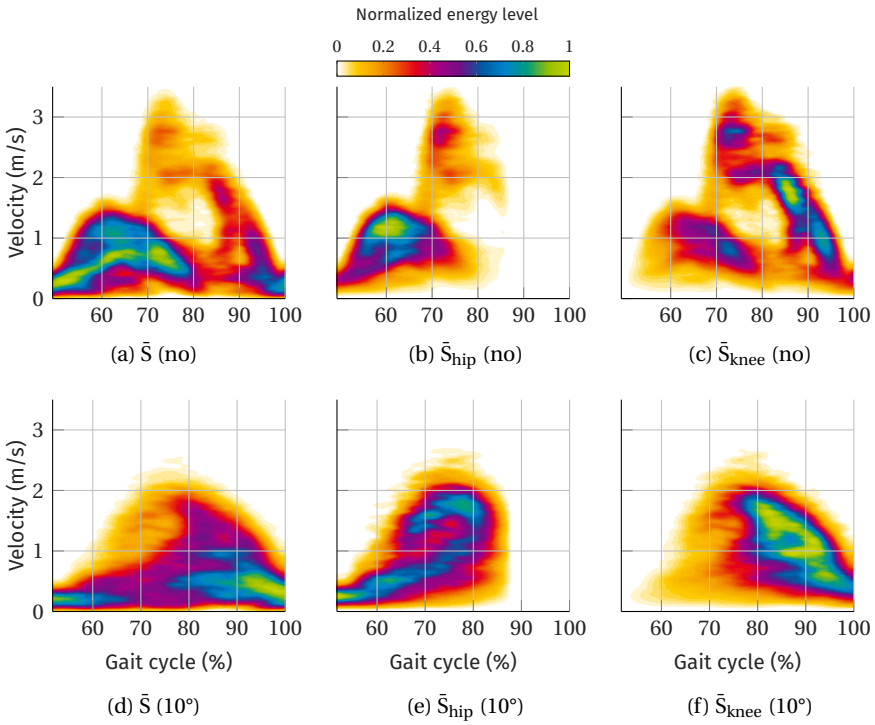

Figure 11.3: Step time spectrograms of one individual walking on a treadmill at 1.1 m/s (a) without (no) and (d) with maximal knee angle restriction (10°). Weighted spectrograms for the estimation of the hip and knee angle trajectories are given in (b, e) and (c, f), respectively.

In order to compensate for the smaller amplitudes of the reflections from the lower leg, the following weighting scheme is applied. First, the step time spectrograms are linearly weighted along the Doppler frequency axis up to the maximal swing velocity of the foot, which is estimated from the radar data (see Section 10.1.5). Here, larger Doppler shifts receive higher weights. Second, we compensate for the fact that the upper leg reflects more of the EM wave's energy in the beginning of a step, while the lower leg mainly does so during the mid-swing and deceleration phase, i.e., toward the end of the step time (see Figs. 11.3a and 11.3d). Accordingly, for the hip and knee angle estimation, the step time spectrograms are multiplied along the time axis with linearly decreasing and increasing weights, respectively. Examples of weighted step time spectrograms for the estimation of the hip angle ($\bar{S}_{hip}$) are shown in Figs. 11.3b and 11.3e for no and maximal knee angle restriction, respectively. Accordingly, Figs. 11.3c and 11.3f show weighted step time spectrograms used for the estimation of the hip angle trajectories ($\bar{S}_{knee}$).

11.2.3 *Gait Parameter Extraction via Hough Transform*

In order to estimate the hip and knee angles from the radar data, we follow the approach proposed by Barbarossa and Lemoine in [BL96], and formulate the IF estimation as a pattern recognition problem. Given the radar backscattering signal $s(t)$, the following steps are applied. First, we compute a TFR $S(t, f)$ of the signal $s(t)$, namely, the spectrogram. It is given by the squared magnitude of the signal's STFT as given in Eq. (2.7). Prior to applying the next step, we

process the spectrograms as described in Section 11.2.2. Then, we utilize the Hough transform to map the TFR onto the signal parameter space using [BL96]

Hough transform

$$H(\boldsymbol{\Theta}) = \int_{-\infty}^{+\infty} \Big(\bar{\mathrm{S}}_{\mathrm{hip}}(t, -2\, v_{\mathrm{knee}}(t; \boldsymbol{\Theta}_{\mathrm{hip}}, l_{\mathrm{ul}})/\lambda) + \bar{\mathrm{S}}_{\mathrm{knee}}(t, -2\, v_{\mathrm{ankle}}(t; \boldsymbol{\Theta}_{\mathrm{hip}}, \boldsymbol{\Theta}_{\mathrm{knee}}, l_{\mathrm{ul}}, l_{\mathrm{ll}})/\lambda) \Big) \mathrm{d}t, \quad (11.9)$$

where $\boldsymbol{\Theta} = \left[\boldsymbol{\Theta}_{\mathrm{hip}}^{\top}, \boldsymbol{\Theta}_{\mathrm{knee}}^{\top}\right]^{\top}$, and v_{knee} and v_{ankle} are the proposed models for the knee and ankle radial velocities, respectively, as given in Section 11.1.3.2. Since the ankle's velocity depends on both, the hip *and* knee angle, we jointly estimate $\boldsymbol{\Theta}_{\mathrm{hip}}$ and $\boldsymbol{\Theta}_{\mathrm{knee}}$, which leads to the sum within the integral. Finally, we search for the global maximum in the parameter space; its coordinates yield the estimates of the parameters.

11.2.4 *Hip-Knee Cyclograms*

In order to jointly analyze the angular kinematics of the lower limbs, we utilize the hip-knee cyclogram, as introduced in Section 3.2. Examples of hip-knee cyclograms for two test subjects are given in Fig. 11.4. The figure includes MoCap data of a tall person as well as a short person to account for the inter-person differences in the data set. The cyclograms depict the mean hip and knee angles, which were obtained by averaging all strides over one measurement period, where individual strides were identified utilizing GRFs. Since the Doppler radar only reveals the motions during the step time of individual legs, we focus on this segment of the gait cycle, which is represented by the colored parts of the cyclogram patterns.

As expected, we find that as a consequence of increased level of knee angle restriction (from yellow to blue), the maximal knee flexion angle decreases.

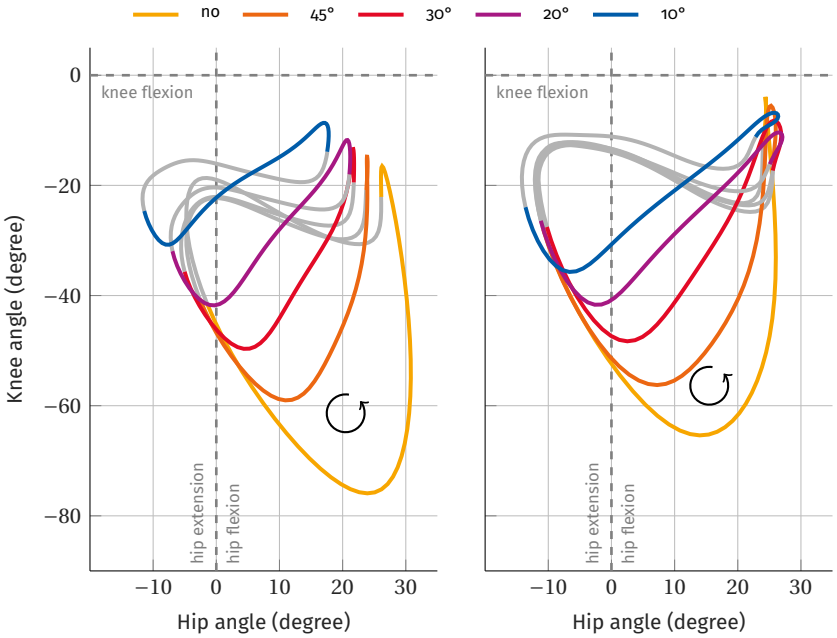

(a) tall person (b) short person

Figure 11.4: Hip-knee cyclograms based on MoCap data for two test subjects at a treadmill speed of 1.1 m/s. The colored parts refer to the step time (right leg).

Note that the knee angle restriction enforced by the orthosis (45°, 30°, 20°, 10°) is not directly reflected in the maximal knee angle measured by the MoCap system. For example, in the case of the tall person, the maximal knee angles assume approximately 60°, 50°, 42°, 31° instead. The cyclograms also show that the hip angle at the time instant of maximal knee flexion decreases (e.g. from ca. 23° to -8° for the tall person). In essence, the entire shape of the cyclogram changes with increasing knee angle restriction.

11.3 EXPERIMENTAL RESULTS

11.3.1 *Validation of Hip and Knee Angle Models*

Figure 11.5 shows the hip and knee angle trajectories of all individuals obtained via motion capturing (yellow) and using angles defined by Boulic *et al.* (gray) [BTT90]. The plotted excerpt corresponds to the step time of the right leg during treadmill walking at 1.1 m/s without knee angle restriction. The MoCap-based angles were averaged over all gait cycles in a 100 s measurement. The angles according to Boulic *et al.* are calculated using spline interpolation which is based on three and four control points for the hip and knee angle, respectively. The latter depend on the relative walking velocity v_{rel} and are indicated by gray circles in Fig. 11.5. The figures highlight the inter-person variability present in the data set. Corresponding plots for the cases with a restricted knee flexion are given in Section A.3.2.

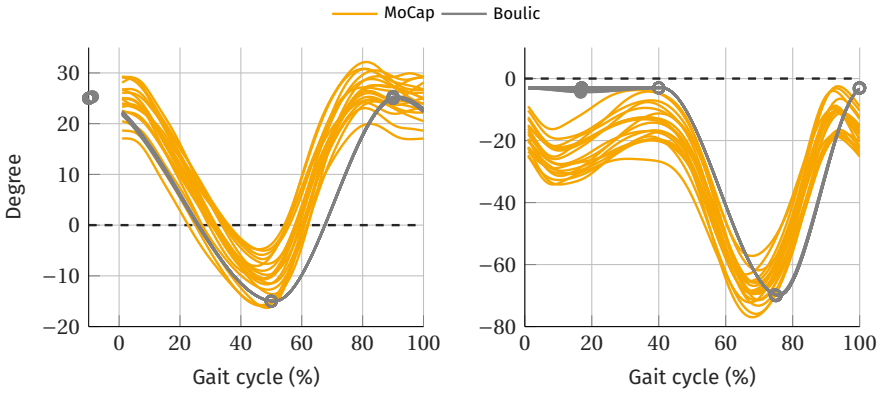

(a) hip angle (b) knee angle

Figure 11.5: Average MoCap hip and knee angle trajectories (over all strides in a measurement) of the right leg for each subject walking normally at a treadmill speed of 1.1 m/s. Angles according to Boulic *et al.* are shown in gray, where the gray circles mark the control points for the spline-based interpolation.

Figure 11.6 shows the average MoCap-based hip and knee angle trajectories over all individuals for different knee angle restrictions. Again, the angles according to Boulic *et al.* are shown in gray, where the control points for the spline-based interpolation are indicated by gray circles [BTT90]. The figures reveal the inter-gait variance in the data set. As indicated by the cyclograms in Fig. 11.4, the plots in Fig. 11.6 clearly show that a restricted knee flexion affects both, the hip and knee angle trajectories. In general, an increased knee angle restriction leads to a lower absolute value in the hip *and* knee angle trajectory.

The model parameters $\{a_{\text{h}}, b_{\text{h}}, c_{\text{h}}, f_{\text{h}}\}$ and $\{a_{\text{k}}, b_{\text{k}}, c_{\text{k}}, f_{\text{k}}\}$ are found by minimizing the squared error between the models in Eq. (11.8) and corresponding

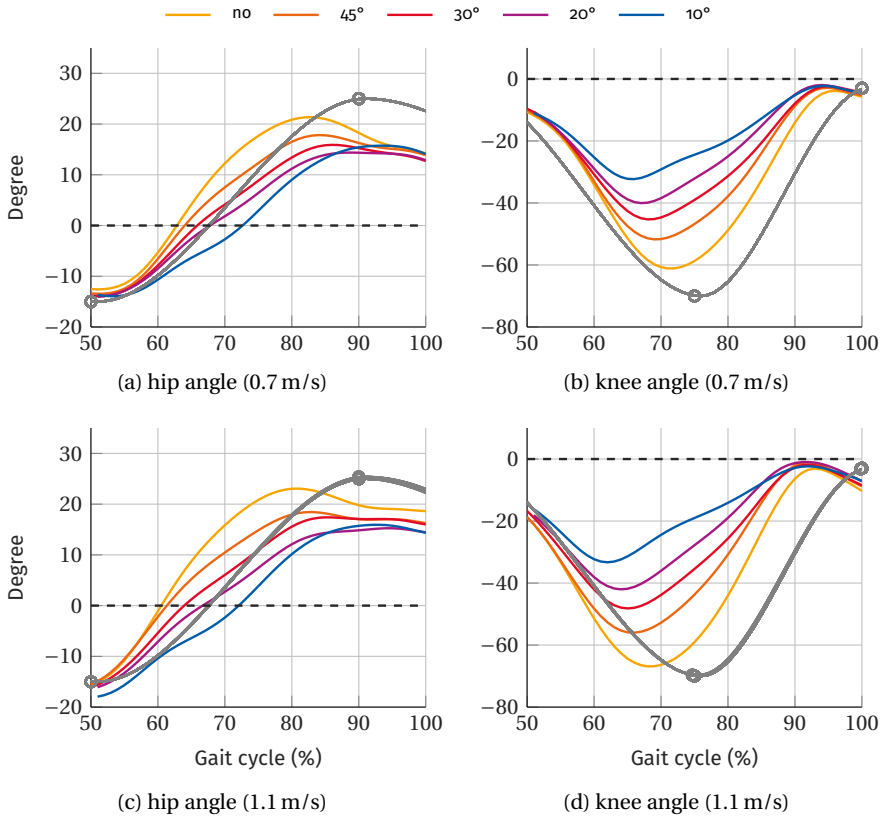

Figure 11.6: Average MoCap (a, c) hip and (b, d) knee angle trajectories (over all test subjects) for different knee angle restrictions and treadmill speeds. Angles according to Boulic's model using spline interpolation are shown in gray, where the circles mark the control points.

MoCap data. Here, the first 40 % of the step time are used, and the Levenberg-Marquardt algorithm is utilized to solve the NLS problem [Gav19; Kel99]. Table 11.1 shows the average parameters over all persons for each walking speed and gait abnormality. As expected from Fig. 11.6, the values for a_h and a_k are decreasing (in amplitude) for increased knee angle restrictions. Table 11.2 shows the root mean squared error (RMSE) between the MoCap-based hip and knee angle trajectories, and those obtained using the models in Eq. (11.8) and the estimated model parameters. For both walking speeds as well as the different knee angle restrictions, the average error is typically smaller than 1°, which shows that the hip and knee angle models are not only suitable for normal but also for abnormal gait.

Using the results from Table 11.1, we aim to reduce the number of parameters that need to be estimated. We find that the standard deviation (SD) of the parameters f_h and f_k is small across all gait abnormalities and walking speeds. Hence, for further analysis, we set $f_h = 1$ for both walking speeds, and set $f_k = 0.8$ and $f_k = 0.9$ for the slow and fast walking speed, respectively. Since the radar and MoCap data are not perfectly synchronized, we avoid estimating the shift parameters b. We note that their values generally depend on the detection of toe-off and heel strike times via GRFs (for details see Section 10.1.3), and thus, for other data sets, their values might deviate from the ones found here. Due to the large inter-person variability within the data set, the offset c reveals a comparably high SD, for both, the hip and the knee angle. Since the offset

Table 11.1: Estimated parameters (mean ± SD over all test subjects) for the (a) hip and (b) knee angle models in Eq. (11.8) obtained via NLS and MoCap data.

		a_h	b_h	c_h	f_h
0.7 m/s	non	17.2 ± 2.0	−1.5 ± 0.6	8.7 ± 3.0	1.2 ± 0.1
	45°	15.7 ± 1.8	−0.8 ± 0.6	7.0 ± 2.7	1.1 ± 0.1
	30°	15.1 ± 2.0	−0.5 ± 0.8	6.5 ± 3.2	1.0 ± 0.1
	20°	15.3 ± 2.2	−0.4 ± 0.7	6.2 ± 3.4	0.9 ± 0.1
	10°	15.1 ± 2.0	−0.7 ± 0.6	4.6 ± 3.0	0.9 ± 0.1
	all	15.7 ± 2.1	−0.8 ± 0.7	6.6 ± 3.3	1.0 ± 0.2
1.1 m/s	non	21.6 ± 2.2	−0.1 ± 0.6	5.7 ± 3.9	1.2 ± 0.1
	45°	20.6 ± 2.7	0.4 ± 0.6	3.8 ± 3.7	1.1 ± 0.1
	30°	19.3 ± 3.0	0.5 ± 0.6	4.5 ± 3.5	1.0 ± 0.1
	20°	19.3 ± 2.8	0.6 ± 0.6	4.0 ± 3.8	0.9 ± 0.1
	10°	19.3 ± 2.5	0.4 ± 0.5	3.5 ± 3.6	1.0 ± 0.1
	all	20.0 ± 2.8	0.4 ± 0.6	4.3 ± 3.7	1.0 ± 0.1

(a) hip angle

		a_k	b_k	c_k	f_k
0.7 m/s	non	−50.3 ± 6.3	0.4 ± 0.9	−15.6 ± 6.8	0.8 ± 0.1
	45°	−42.2 ± 4.3	0.3 ± 0.2	−13.4 ± 5.1	0.8 ± 0.1
	30°	−32.2 ± 6.1	0.3 ± 0.3	−12.8 ± 5.2	0.8 ± 0.1
	20°	−27.7 ± 6.0	0.3 ± 0.5	−11.3 ± 5.0	0.8 ± 0.1
	10°	−24.1 ± 5.8	0.4 ± 0.4	−9.2 ± 4.0	0.8 ± 0.1
	all	−35.1 ± 11.2	0.3 ± 0.5	−12.4 ± 5.6	0.8 ± 0.1
1.1 m/s	non	−61.8 ± 8.8	0.9 ± 0.4	−6.7 ± 9.2	0.8 ± 0.1
	45°	−52.3 ± 7.0	0.9 ± 0.4	−6.5 ± 7.0	0.9 ± 0.1
	30°	−40.0 ± 7.8	0.8 ± 0.4	−9.4 ± 6.8	0.9 ± 0.1
	20°	−34.3 ± 7.2	0.7 ± 0.4	−9.3 ± 5.3	1.0 ± 0.1
	10°	−29.6 ± 6.6	0.6 ± 0.4	−8.2 ± 3.3	1.0 ± 0.1
	all	−43.3 ± 14.0	0.8 ± 0.4	−8.1 ± 6.6	0.9 ± 0.1

(b) knee angle

Table 11.2: Root mean squared error (RMSE) (mean ± SD over all test subjects in degree) between the modeled and MoCap-based hip and knee angles.

knee angle restriction	0.7 m/s		1.1 m/s	
	hip	knee	hip	knee
non	0.50 ± 0.14	0.82 ± 0.37	0.58 ± 0.15	0.84 ± 0.30
45°	0.45 ± 0.12	0.88 ± 0.27	0.44 ± 0.15	0.67 ± 0.24
30°	0.38 ± 0.13	0.98 ± 0.31	0.42 ± 0.17	0.77 ± 0.32
20°	0.36 ± 0.12	0.98 ± 0.39	0.42 ± 0.17	0.84 ± 0.32
10°	0.37 ± 0.14	1.04 ± 0.30	0.42 ± 0.18	0.91 ± 0.34
all	0.41 ± 0.14	0.94 ± 0.34	0.45 ± 0.18	0.81 ± 0.32

c is sensitive to the precise placement of the MoCap markers, we do not seek the estimation of their values. In essence, utilizing the MoCap-based shift and offset parameters, we limit ourselves to estimating the amplitude parameters a_h and a_k.

11.3.2 *Validation of Boulic's Global Walking Model*

Next, we investigate the applicability of Boulic's global walking model for calculating the velocity trajectories of the lower limb joints from given hip and knee angle trajectories. Figure 11.7 show the radial velocities for the knee and ankle joint during the step time of the right leg. The MoCap data (black dashed) was averaged over all strides in the measurement. The Boulic model (gray) is based on Eqs. (11.5) and (11.6), and joint angles obtained via spline interpolation as indicated in Fig. 11.6. Since the stride time is different for the two measurements, the velocity trajectories differ. Using Boulic's velocity models (Eqs. (11.5) and (11.6)) and MoCap-based angles, we find that the obtained velocities (turquoise) align well with the MoCap data. Using Boulic's velocity models (Eqs. (11.5) and (11.6)) in combination with the proposed models for the hip and knee angles (Eq. (11.8) with fixed f as described in Section 11.3.1), we find that the resulting velocity trajectories (green) are generally in good alignment with the MoCap data (black dashed). The average RMSE between the two latter velocity trajectories over all knee angle restrictions and walking speeds is calculated as 0.12 m/s and 0.24 m/s for the knee and ankle velocities, respectively. Table A.1 gives the RMSE for all considered conditions.

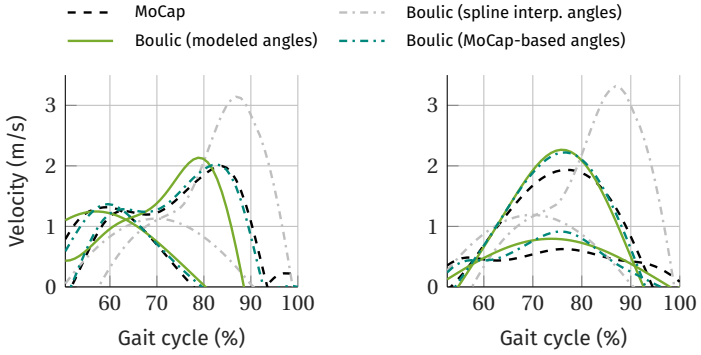

(a) no restriction (b) maximal restriction (10°)

Figure 11.7: Comparison of measured (MoCap) and modeled lower limb radial velocities. The latter are based on Boulic's velocity model and modeled angles (green), interpolated angles using splines (gray), and MoCap-based angles (turquoise). The data is from a test subject (same as in Fig. 11.3) walking on a treadmill at 1.1 m/s.

11.3.3 *Hip-knee Cyclogram Estimation*

In order to evaluate the performance of the proposed framework, we calculate the RMSE between the estimated and the MoCap-based hip and knee angle trajectories. Figures 11.7a and 11.7b indicate that the ankle's maximal velocity is overestimated when using Boulic's model; particularly when the knee angle is restricted. In order to mitigate this offset, we adapt Eq. (11.6) w.r.t. the lower leg length parameter l_ll, which directly affects the maximal ankle velocity. Thus, the lower leg length is empirically set to $0.8 \cdot l_\mathrm{ll}$.

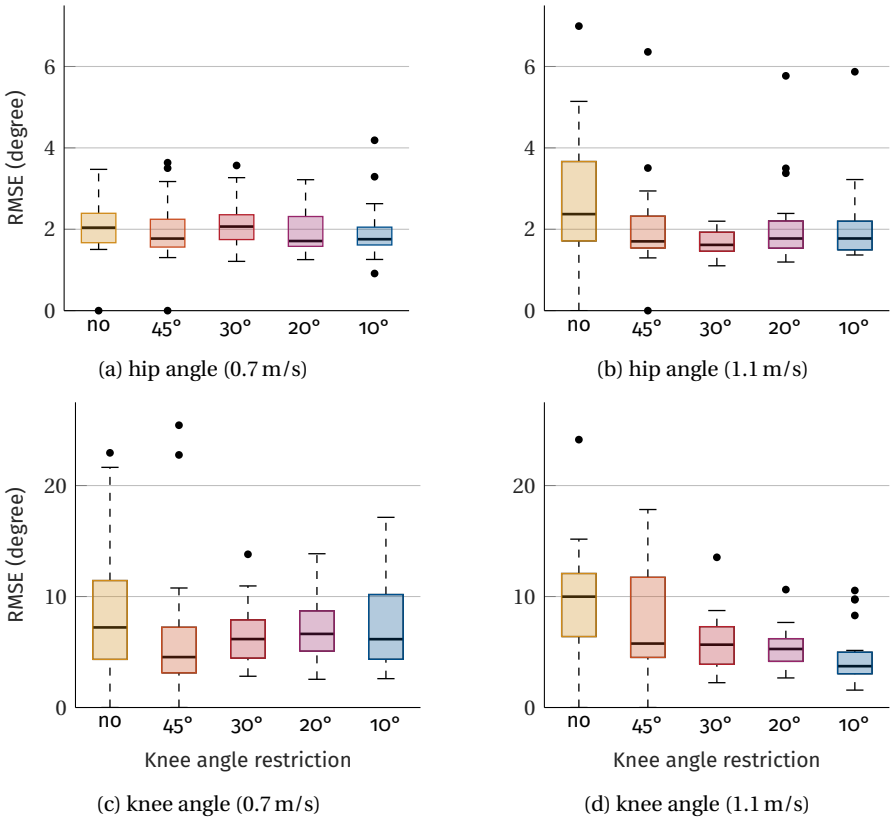

(a) hip angle (0.7 m/s)

(b) hip angle (1.1 m/s)

(c) knee angle (0.7 m/s)

(d) knee angle (1.1 m/s)

Figure 11.8: Boxplots of the root mean squared error (RMSE) between MoCap-based and estimated hip and knee angle trajectories. The central mark in each box gives the median RMSE, and the bottom and top edges of the box indicate the 25th and 75th percentiles, respectively. Errors that are far away from the median (falling below or exceeding the 25th and 75th percentiles by 1.5 times the interquartile range), are considered as outliers and indicated by dots.

Figure 11.8 shows boxplots of the resulting RMSEs for the hip and knee angle and the two walking speeds. In general, the hip angle can be estimated more accurately from the radar data compared to the knee angle. Further, errors tend to be larger for normal walking opposed to walking with a knee angle confinement. The overall median RMSE for the hip angle is 1.8° and 1.8° for the slow and fast walking speed, respectively. For the knee angle, the median RMSE assumes 6.2° and 5.7° for the slow and fast walking speed, respectively.

Figure 11.9 shows examples of estimated cyclograms of two individuals (same as in Fig. 11.4). For both individuals, the estimated cyclograms deviate most in case of normal walking (yellow). In case of the short person, the maximal knee angle during walking is generally underestimated for all knee angle restriction. However, the *relative* positions of the cyclograms, i.e., from yellow to blue, is correctly detected for both individuals.

11.4 DISCUSSION

We demonstrated that it is generally possible to extract detailed kinematic information of the gait, i.e., hip and knee angle trajectories, by analyzing radar micro-Doppler signatures. Even though the estimated the hip-knee cyclograms do not perfectly coincide with the true cyclograms in all cases, the gait abnor-

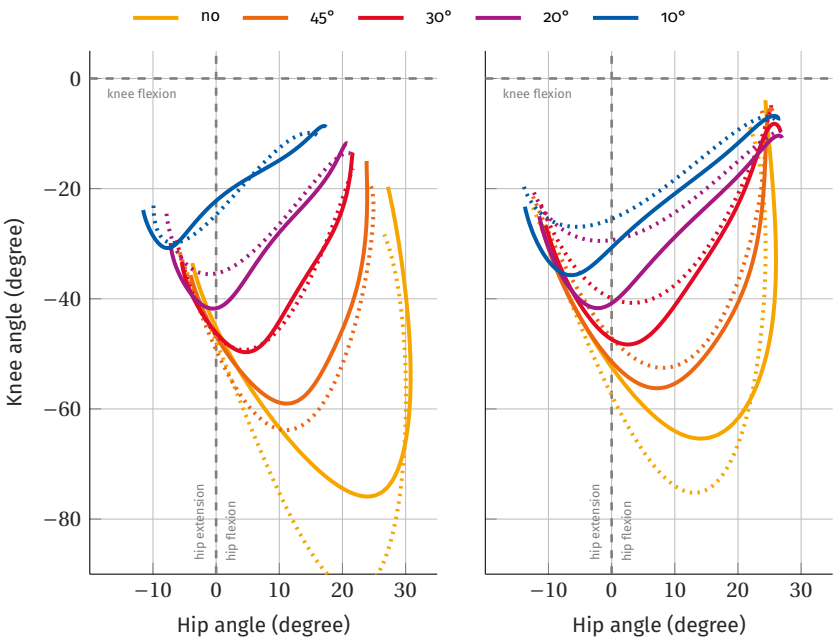

(a) tall person (b) short person

Figure 11.9: MoCap-based (solid) and estimated (dashed) hip-knee cyclograms for two test subjects at a treadmill speed of 1.1 m/s.

mality is often correctly identified for one individual, i.e., the *relative* difference in hip and knee angle trajectories for increased knee angle restrictions. Thus, the hip-knee cyclograms could be used as an indicator for changes in the gait pattern of a person without the need for wearable sensors.

Our findings are based on treadmill walking and the proposed framework has to be reevaluated for translational walking. Future studies should include more test subjects (possibly with gait disorders). We used one medium size orthosis for all volunteers to artificially restrict their knee angle. Since the knee marker was attached to the orthosis, a misfit directly affects the angle calculation and thus the model parameters. Due to the limited number of test subjects in our experiments, the choice of values for the parameters f_h and f_k might not generalize to a larger group of individuals. In order to further improve the accuracy of the parameter estimates, particularly for the knee angle, one could incorporate the reflectivity of individual body parts over time by approximating their surfaces as ellipsoids [Che19] or cylinders [vDG03]. In addition, the locations of the scattering points on the lower leg have to be investigated. We did not find the tibia ($0.5 \cdot l_{\text{ll}}$) to be most reflective point on the lower leg, as often employed in micro-Doppler simulators [Che19].

We point out that the method could be extended to estimating the ankle's trajectory, too. As for the knee and ankle joints, Boulic's model can be used to model the radial velocity of the swinging foot during a gait cycle. The proposed parametric angle models in combination with Boulic's walking model can be utilized to simulate micro-Doppler gait signatures with a large intra-class variance, which can be e.g. useful to train deep learning architectures without the need of conducting studies involving (a large number of) humans [EGA20]. Further, the proposed models can be combined with limb joint tracking techniques (see e.g., [QTP+19; DT14]), or efficient micro-Doppler parameter estimation methods [LV14].

12

SUMMARY

In this part of the thesis, we utilized simultaneously recorded radar and MoCap data to investigate if Doppler radar is capable of extracting biomechanical gait parameters in a similar quality as marker-based motion capturing.

In Chapter 10, new methods were introduced to measure the flight time and lower limb joint radial velocities based on radar micro-Doppler signatures. Existing and new methods for extracting spatiotemporal and kinematic parameters were evaluated in unimpaired gait and for gait abnormalities introduced by an orthosis, at different walking speeds, and at a frontal and a rear positioning of the radar. Based on experimental data of 19 volunteers walking on a treadmill, the gait parameters obtained through radar and motion capturing were qualitatively compared and differences were statistically analyzed. Five spatiotemporal and three kinematic parameters could be extracted from the radar data with high accuracy for most of the considered conditions. However, in the proposed method, flight and stance time measurements rely on the correct detection of the time instant of maximal knee velocity.

Further, in Chapter 11, we considered parametric models for the hip and knee angles during treadmill walking, whose parameters are related to gait kinematics. In combination with the walking model by Boulic *et al.*, the proposed models were used to calculate radial knee and ankle velocities. Utilizing the Hough transform, the hip-knee cyclograms were estimated from radar micro-Doppler signatures. Results show that micro-Doppler signatures are sensitive to changes in gait patterns and enable the extraction of medically pertinent biomechanical gait indicators.

REFERENCES

[AAKS17] S. Abdulatif *et al.*, "Real-time capable micro-Doppler signature decomposition of walking human limbs," in *IEEE Radar Conference*, 2017. DOI: 10.1109/RADAR.2017.7944367 (cit. on p. 94).

[Anc20] Ancortek Inc. (Jun. 2020). SDR-KIT 2400AD, [Online]. Available: http://ancortek.com/sdr-kit-2400ad (cit. on p. 85).

[BL96] S. Barbarossa and O. Lemoine, "Analysis of nonlinear FM signals by pattern recognition of their time-frequency representation," *IEEE Signal Processing Letters*, vol. 3, no. 4, pp. 112–115, Apr. 1996. DOI: 10.1109/97.489064 (cit. on pp. 103, 107, 108).

[BH95] Y. Benjamini and Y. Hochberg, "Controlling the false discovery rate: A practical and powerful approach to multiple testing," *Journal of the Royal Statistical Society: Series B (Methodological)*, vol. 57, no. 1, pp. 289–300, 1995. DOI: 10.1111/j.2517-6161.1995.tb02031.x (cit. on p. 97).

[BTT90] R. Boulic, N. M. Thalmann, and D. Thalmann, "A global human walking model with real-time kinematic personification," *The Visual Computer*, vol. 6, no. 6, pp. 344–358, Nov. 1990. DOI: 10.1007/BF01901021 (cit. on pp. 103–105, 109).

[Che19] V. C. Chen, *The Micro-Doppler Effect in Radar*, 2nd ed. Norwood, MA, USA: Artech House, 2019 (cit. on pp. 89, 105, 114).

[CZA08] L. Cirillo, A. Zoubir, and M. Amin, "Parameter estimation for locally linear FM signals using a time-frequency Hough transform," *IEEE Transactions on Signal Processing*, vol. 56, no. 9, pp. 4162–4175, Sep. 2008. DOI: 10.1109/TSP.2008.924797 (cit. on p. 103).

[DT14] Y. Ding and J. Tang, "Micro-Doppler trajectory estimation of pedestrians using a continuous-wave radar," *IEEE Transactions on Geoscience and Remote Sensing*, vol. 52, no. 9, pp. 5807–5819, Jan. 2014. DOI: 10.1109/TGRS.2013.2292826 (cit. on p. 114).

[EGA20] B. Erol, S. Z. Gürbüz, and M. G. Amin, "Motion classification using kinematically sifted ACGAN-synthesized radar micro-Doppler signatures," *IEEE Transactions on Aerospace and Electronic Systems*, 2020, to be pusblished. DOI: 10.1109/TAES.2020.2969579 (cit. on p. 114).

[Gav19] H. P. Gavin. (Aug. 2019). The Levenberg-Marquardt method for nonlinear least squares curve-fitting problems, [Online]. Available: http://people.duke.edu/~hpgavin/ce281/lm.pdf (cit. on p. 110).

[GM19] S. Ghio and M. Martorella, "Inverse Radon transform scaling via spin rate estimation for resident space object size assessment," *IET Radar, Sonar and Navigation*, vol. 13, no. 6, pp. 900–905, Jun. 2019. DOI: 10.1049/IET-RSN.2018.5337 (cit. on p. 103).

[GTK+17] F. Gholami *et al.*, "A Microsoft Kinect-based point-of-care gait assessment framework for multiple sclerosis patients," *IEEE Journal of Biomedical and Health Informatics*, vol. 21, no. 5, pp. 1376–1385, Sep. 2017. DOI: 10.1109/JBHI.2016.2593692 (cit. on p. 102).

[GC11] J. D. Gibbons and S. Chakraborti, "Nonparametric statistical inference," in *International Encyclopedia of Statistical Science*, M. Lovric, Ed., Berlin, Heidelberg, Germany: Springer, 2011. DOI: 10.1007/978-3-642-04898-2_420 (cit. on p. 96).

[Gos98] A. Goswami, "A new gait parameterization technique by means of cyclogram moments: Application to human slope walking," *Gait & Posture*, vol. 8, no. 1, pp. 15–36, Aug. 1998. DOI: 10.1016/S0966-6362(98)00014-9 (cit. on p. 103).

[GM17] A. Gouelle and F. Mégrot, "Interpreting spatiotemporal parameters, symmetry, and variability in clinical gait analysis," in *Handbook of Human Motion*, B. Müller *et al.*, Eds., Cham, Germany: Springer, 2017, pp. 1–20. DOI: 10.1007/978-3-319-30808-1_35-1 (cit. on pp. 94, 95, 102).

[GSD+19] M. Grimmer *et al.*, "Stance and swing detection based on the angular velocity of lower limb segments during walking," *Front. Neurorobot.*, vol. 13, no. 57, pp. 1–15, Jul. 2019. DOI: 10.3389/fnbot.2019.00057 (cit. on p. 92).

[HKP+17] J. Hannink *et al.*, "Sensor-based gait parameter extraction with deep convolutional neural networks," *IEEE Journal of Biomedical and Health Informatics*, vol. 21, no. 1, pp. 85–93, Jan. 2017. DOI: 10.1109/JBHI.2016.2636456 (cit. on p. 102).

[HWI+16] J. H. Hollman *et al.*, "A comparison of variability in spatiotemporal gait parameters between treadmill and overground walking conditions," *Gait & Posture*, vol. 43, pp. 204–209, Jan. 2016 (cit. on p. 102).

[Kel99] C. T. Kelley, *Iterative methods for optimization*. Philadelphia, PA, USA: Society for Industrial and Applied Mathematics, 1999 (cit. on p. 110).

[LH08] S. J. Lee and J. Hidler, "Biomechanics of overground vs. treadmill walking in healthy individuals," *Journal of Applied Physiology: Respiratory, Environmental and Exercise Physiology*, vol. 104, no. 3, pp. 747–755, Mar. 2008 (cit. on p. 102).

[LV14] G. Li and P. K. Varshney, "Micro-Doppler parameter estimation via parametric sparse representation and pruned orthogonal matching pursuit," *IEEE J. Sel. Topics Appl. Earth Observ.*, vol. 7, no. 12, pp. 4937–4948, Dec. 2014. DOI: 10.1109/JSTARS.2014.2318596 (cit. on p. 114).

[Lip06] L. Lippert, "Gait," in *Clinical Kinesiology and Anatomy*, 4th ed., Philadelphia, PA, USA: F. A. Davis, 2006, ch. 21 (cit. on pp. 85, 105).

[NWD+03] L. Nolan *et al.*, "Adjustments in gait symmetry with walking speed in trans-femoral and trans-tibial amputees," *Gait & Posture*, vol. 17, no. 2, pp. 142–151, Apr. 2003. DOI: https://doi.org/10.1016/S0966-6362(02)00066-8 (cit. on p. 102).

[QTP+19] F. Quaiyum *et al.*, "Noncontact human gait analysis and limb joint tracking using doppler radar," *IEEE Journal of Electromagnetics, RF and Microwaves in Medicine and Biology*, vol. 3, no. 1, pp. 61–70, Mar. 2019. DOI: 10.1109/JERM.2018.2881238 (cit. on p. 114).

[SGZ20] A.-K. Seifert, M. Grimmer, and A. M. Zoubir, "Doppler radar for the extraction of biomechanical parameters in gait analysis," *IEEE Journal of Biomedical and Health Informatics*, 2020, (to be published). DOI: 10.1109/JBHI.2020.2994471 (cit. on pp. 85, 89).

[SAZ19] A.-K. Seifert, M. G. Amin, and A. M. Zoubir, "Toward unobtrusive in-home gait analysis based on radar micro-Doppler signatures," *IEEE Transactions on Biomedical Engineering*, vol. 66, no. 9, pp. 2629–2640, Sep. 2019. DOI: 10.1109/TBME.2019.2893528 (cit. on p. 102).

[SRZA19] A.-K. Seifert *et al.*, "A robust and sequential approach for detecting gait asymmetry based on radar micro-Doppler signatures," in *European Signal Processing Conference*, 2019. DOI: 10.23919/EUSIPCO.2019.8902343 (cit. on p. 102).

[SDTP15] L. Stanković *et al.*, "Inverse Radon transform-based micro-Doppler analysis from a reduced set of observations," *IEEE Transactions on Aerospace and Electronic Systems*, vol. 51, no. 2, pp. 1155–1169, Apr. 2015. DOI: 10.1109/TAES.2014.140098 (cit. on p. 103).

[vDG03] P. van Dorp and F. C. A. Groen, "Human walking estimation with radar," *IEE Proceedings Radar, Sonar and Navigation*, vol. 150, no. 5, pp. 356–365, Oct. 2003. DOI: 10.1049/ip-rsn:20030568 (cit. on p. 114).

[WSRC14] F. Wang *et al.*, "Quantitative gait measurement with pulse-Doppler radar for passive in-home gait assessment," *IEEE Transactions on Biomedical Engineering*, vol. 61, no. 9, pp. 2434–2443, Sep. 2014. DOI: 10.1109/TBME.2014.2319333 (cit. on p. 102).

[YNC04] C. Yam, M. S. Nixon, and J. N. Carter, "Automated person recognition by walking and running via model-based approaches," *Pattern Recognition*, vol. 37, no. 5, pp. 1057–1072, May 2004. DOI: 10.1016/j.patcog.2003.09.012 (cit. on pp. 103, 105).

Part IV

CONCLUSIONS AND OUTLOOK

„Damit das Mögliche entsteht,
muß immer wieder das Unmögliche versucht werden."

— *Hermann Hesse, 1960.*

13 SUMMARY AND CONCLUSIONS

In this thesis, the applicability of radio frequency (RF) sensing for gait analysis was investigated. While radar has been typically employed for discriminating different human motions, this thesis focused on an intra-class motion classification problem, namely, gait recognition. Having applications such as remote health and telemedicine in mind, unaided and aided walking styles were classified. Further, the detection of gait asymmetry based on radar backscatterings has been addressed. To assist health professionals and physiotherapists in treatment and rehabilitation, medically relevant gait parameters were extracted from radar data. Here, spatiotemporal and kinematic parameters were considered.

This chapter provides a summary and the main conclusions of the work performed in this thesis. Section 13.1 focuses on achievements in the area of radar-based gait classification, and Section 13.2 outlines the contributions toward radar-based gait analysis.

13.1 RADAR-BASED GAIT CLASSIFICATION

Classification of Abnormal and Cane-Assisted Gait

A signal processing framework has been developed to classify five different walking styles based on radar backscatterings. It utilizes subspace-based features that are automatically extracted from the cadence-velocity diagram (CVD). Unsupervised feature learning via PCA and its extensions has been shown to be more effective in capturing the underlying gait characteristics compared to pre-defined feature sets. The CVD is a time-invariant 2D signal representation and has been shown to be more suitable for unsupervised feature learning than the spectrogram. As such, it was demonstrated that the choice of radar signal representation is key for achieving high classification rates. Results are based on experimental radar data of ten able-bodied individuals. Besides normal and simulated limping gait, two cane-assisted walking styles were considered. In addition, the proposed framework was assessed based on radar recordings of four individuals with diagnosed gait disorders.

The proposed framework for radar-based gait classification shows superior performance when compared to state-of-the-art gait recognition methods utilizing pre-defined features. Here, the proposed subspace-based feature learning from the CVD is more effective in exploiting the information contained in the radar backscatterings.

Detection of Gait Asymmetry

In the area of radar-based gait analysis for remote health and telemedicine, long-term monitoring of gait patterns can help to identify various pathologies at an early stage. To this end, a gait asymmetry detection framework has been developed. Using radar data of short observation times, and thus a limited number of observed steps, the gait asymmetry of four diagnosed persons was correctly detected with high reliability for at least one of the considered motion directions, i.e., walking toward or away from the radar system.

The proposed detector allows for automatic detection of gait asymmetry based on realistic radar measurements of short durations, and irrespective of the degree of gait abnormality.

13.2 TOWARD RADAR-BASED GAIT ANALYSIS

Extraction of Biomechanical Parameter

In order to demonstrate the richness of information provided by the RF sensing modality, signal processing methods were developed to extract 11 spatiotemporal and kinematic parameters from radar micro-Doppler signatures. By qualitatively and quantitatively comparing the radar-based parameters to those obtained from simultaneously recorded marker-based motion capture (MoCap) data, the accuracy of the radar system was assessed. Further, by systematically introducing various degrees of gait abnormality via an adjustable orthosis, the effectiveness of radar in capturing fine changes in gait patterns was demonstrated.

The presented signal processing schemes allow for automatic extraction of medically relevant gait parameters from radar backscatterings with sufficient accuracy for basic gait analysis.

Estimation of Lower Limb Angular Kinematics

Besides discrete biomechanical parameters, time-varying gait kinematics are of interest in gait analysis. For the estimation of lower limb angular kinematics, parametric models for the lower limb radial velocities have been proposed. Using these models and the Hough transform as a pattern recognition tool, the hip and knee angle trajectories during step time were estimated from radar micro-Doppler signatures.

The proposed models for the lower limb radial velocities enable automatic extraction of time-varying gait kinematics from radar data. In addition, since their parameters reflect underlying gait biomechanics, they can also be utilized too simulated radar micro-Doppler signatures of abnormal gait.

14 FUTURE RESEARCH DIRECTIONS

In this chapter, possible future research directions for radar-based gait analysis are outlined.

14.1 EXPLOITATION OF RADIO-FREQUENCY SENSING CAPABILITIES

In this thesis, a continuous-wave radar system was employed. As such, only the time-varying Doppler information, represented in the time-frequency domain, was exploited. However, of course, radar systems can also provide range information when, e.g., operated in frequency modulated continuous wave (FMCW) mode. Then additional 2D joint-variable representations, namely, range vs. slow time, and range vs. Doppler maps, become available. Each of these 2D signal representations provides valuable information that might not be present or difficult to extract from other domains. These representations have successfully been exploited in, e.g., fall motion detection methods [JA18]. Further, a combined Doppler, range, and slow time analysis results in a 3D signal representation, also referred to as radar data cube [EA19]. For radar-based human activity classification, the information provided by the radar data cube has successfully been exploited by use of multi-subspace learning [EA19].

Also radar-based gait analysis system could benefit form the additional information provided by the range measurement. In this respect, additional spatial gait parameters such as the step width might be extracted from the radar backscatterings. An overview on multi-domain human motion classification and respective signal processing approaches can be found in, e.g., [LFD+19; Ami17].

14.2 SENSOR FUSION

The performance and reliability of RF-based gait analysis systems could potentially be further improved by using multiple radar devices simultaneously. When each radar has a different viewing angle on the target's motion, the actual walking path becomes less important. As such, for in-home scenarios, usual walking paths rather than pre-defined ones can be monitored. Multi-static radar systems, which provide different viewing angles on the target, have successfully been applied for human motion sensing, including gait classification [CLFG18; FRGG17; FRG15a; FRG15b].

Besides using multiple radar systems, the combination of different sensing modalities should be investigated. Diverse sensing bears the chance to overcome disadvantages of individuals sensors, and, thus, increase the system's accuracy and reliability. Here, wearable sensors (e.g. instrumented shoes or insoles, gyroscopes, electromyography) as well as other non-contact sensors (e.g. video cameras, microphones, force mats) could be combined with radar systems. Existing multi-sensory approaches that combine radar with other sensing technologies include, e.g., [LLS+19; LSH+19].

14.3 DEEP LEARNING APPROACHES

Multi-dimensional radar signal representations as outlined in Section 14.1, and multi-modal sensing as described in Section 14.2 lead to higher data dimensionality, an increased number of data samples, or both simultaneously. This calls for deep learning approaches that can be trained to automatically extract relevant information, such as biomechanical or kinematic parameters, from the backscattered radar signals. Since deep learning architectures do not rely on pre-defined features, but learn the salient data characteristics through excessive training, they can outperform common machine learning algorithms in terms of classification or prediction accuracy. For these reasons, the use of deep learning approaches has become of increased interest for radar-based human motion recognition [GA19].

In particular for healthcare applications, the treating physician or physiotherapist might not be interested in interpreting, e.g., time-varying gait kinematics, but prefers to directly assess gait parameters that are representative for the medical situation. In this case, deep learning approaches can aid in translating abstract data representations into context-related knowledge [HKP+17].

However, a major drawback of deep learning methods is that they typically require a large number of (training) data [EGA20; SÖG18]. In the case of human motion analysis, real data are particularly challenging to obtain since it requires experiments involving humans. These studies are often time-consuming and rely on the participation of volunteers. Hence, the available training data often lack sufficient variability in terms of motion articulations and individuals. Recent approaches to overcome this problem include the simulation of diversified micro-Doppler signatures, where height, walking speed, and stride rate were varied to obtain a large training data set (32000 samples) from limited experimental data (55 samples) [SEGA18]. Further, it has been shown that the use of generative adversarial networks (GANs) to generate kinematically correct radar micro-Doppler signatures improves the classification performance on eight different ADLs [EGA20]. In this regard, the parametric models for the lower limb gait kinematics proposed in this thesis can be used to either simulate micro-Doppler signatures with a larger intra-class variance, or to aid in assessing whether GAN-based generated micro-Doppler signatures are kinematically meaningful.

14.4 ADDITIONAL APPLICATIONS

Finally, we would like to highlight some additional applications where radar-based gait analysis can facilitate the respective decision making processes.

In radar-based indoor motion classification, an open problem is the real-time detection of the starting and ending times of motions. In practical scenarios, we observe a *stream of motions*, rather than clearly separated activities. Recent works in this area consider the *human ethogram*, which defines the *possible* motion transitions, e.g., walking after getting up from sitting, where getting up is a motion of its own [Ami20; Gue19]. In this context, e.g., fall motion detection systems could benefit from either the detection of gait alternations shortly before a fall, or gait abnormalities in general, including the use of an assistive walking device. In these cases, the system should be more sensitive since mobility device users and individuals with a history of falls are more likely to fall again, and often have an increased fear of falling [GWL+15].

Lastly, it is pointed out that the human gait is often regarded as a biometric trait [BHP05]. In security applications, radar can contribute to advanced person identification tools by recognizing physical or behavioral characteristics of individuals. Also in smart homes, e.g., lighting configurations or unlocking specific doors or cupboards can be based on the identification of a person through RF backscatterings. The applicability of radar in recognizing individuals by their gait motions has been demonstrated in [VKJ+18; CLFG18; TSM+18]. While, in general, the methods presented in this thesis could contribute to enhancing these systems, their applicability have to be re-evaluated for the inter-person classification problem.

REFERENCES

[Ami17] M. G. Amin, Ed., *Radar for Indoor Monitoring: Detection, Classification, and Assessment*. Boca Raton, FL, USA: CRC Press, 2017 (cit. on p. 123).

[Ami20] M. G. Amin, "Micro-Doppler classification of activities of daily living incorporating human ethogram," in *SPIE Defense and Commercial Sensing*, SPIE, 2020. DOI: 10.1117/12.2558322 (cit. on p. 124).

[BHP05] N. V. Boulgouris, D. Hatzinakos, and K. N. Plataniotis, "Gait recognition: A challenging signal processing technology for biometric identification," *IEEE Signal Processing Magazine*, vol. 22, no. 6, pp. 78–90, Nov. 2005. DOI: 10.1109/MSP.2005.1550191 (cit. on p. 125).

[CLFG18] Z. Chen *et al.*, "Personnel recognition and gait classification based on multistatic micro-Doppler signatures using deep convolutional neural networks," *IEEE Geoscience and Remote Sensing Letters*, vol. 15, no. 5, pp. 669–673, May 2018. DOI: 10.1109/LGRS.2018.2806940 (cit. on pp. 123, 125).

[EGA20] B. Erol, S. Z. Gürbüz, and M. G. Amin, "Motion classification using kinematically sifted ACGAN-synthesized radar micro-Doppler signatures," *IEEE Transactions on Aerospace and Electronic Systems*, 2020, to be pusblished. DOI: 10.1109/TAES.2020.2969579 (cit. on p. 124).

[EA19] B. Erol and M. G. Amin, "Radar data cube processing for human activity recognition using multisubspace learning," *IEEE Transactions on Aerospace and Electronic Systems*, vol. 55, no. 6, pp. 3617–3628, Apr. 2019. DOI: 10.1109/TAES.2019.2910980 (cit. on p. 123).

[FRG15a] F. Fioranelli, M. Ritchie, and H. Griffiths, "Classification of unarmed/armed personnel using the NetRAD multistatic radar for micro-Doppler and singular value decomposition features," *IEEE Geoscience and Remote Sensing Letters*, vol. 12, no. 9, pp. 1933–1937, Sep. 2015. DOI: 10.1109/LGRS.2015.2439393 (cit. on p. 123).

[FRGG17] F. Fioranelli *et al.*, "Feature diversity for optimized human micro-Doppler classification using multistatic radar," *IEEE Transactions on Aerospace and Electronic Systems*, vol. 53, no. 2, pp. 640–654, Apr. 2017. DOI: 10.1109/TAES.2017.2651678 (cit. on p. 123).

[FRG15b] F. Fioranelli, M. Ritchie, and H. Griffiths, "Aspect angle dependence and multistatic data fusion for micro-Doppler classification of armed/unarmed personnel," *IET Radar, Sonar and Navigation*, vol. 9, no. 9, pp. 1231–1239, Dec. 2015. DOI: 10.1049/iet-rsn.2015.0058 (cit. on p. 123).

[GWL+15] N. M. Gell *et al.*, "Mobility device use in older adults and incidence of falls and worry about falling: Findings from the 2011–2012 national health and aging trends study," *Journal of the American Geriatrics Society*, vol. 63, no. 5, pp. 853–859, May 2015. DOI: 10.1111/jgs.13393 (cit. on p. 124).

[Gue19] R. G. Guendel, "Radar classification of contiguous activities of daily living," Master's thesis, Villanova University, Department of Electrical and Computer Engineering, Dec. 2019. eprint: https://arxiv.org/pdf/2001.01556.pdf (cit. on p. 124).

[GA19] S. Z. Gürbüz and M. G. Amin, "Radar-based human-motion recognition with deep learning: Promising applications for indoor monitoring," *IEEE Signal Processing Magazine*, vol. 36, no. 4, pp. 16–28, Jul. 2019. DOI: 10.1109/MSP.2018.2890128 (cit. on p. 124).

[HKP+17] J. Hannink *et al.*, "Sensor-based gait parameter extraction with deep convolutional neural networks," *IEEE Journal of Biomedical and Health Informatics*, vol. 21, no. 1, pp. 85–93, Jan. 2017. DOI: 10.1109/JBHI.2016.2636456 (cit. on p. 124).

[JA18] B. Jokanović and M. Amin, "Fall detection using deep learning in range-Doppler radars," *IEEE Transactions on Aerospace and Electronic Systems*, vol. 54, no. 1, pp. 180–189, Feb. 2018. DOI: 10.1109/TAES.2017.2740098 (cit. on p. 123).

[LFD+19] J. Le Kernec *et al.*, "Radar signal processing for sensing in assisted living: The challenges associated with real-time implementation of emerging algorithms," *IEEE Signal Processing Magazine*, vol. 36, no. 4, pp. 29–41, Jul. 2019. DOI: 10.1109/MSP.2019.2903715 (cit. on p. 123).

[LLS+19] H. Li *et al.*, "Hierarchical sensor fusion for micro-gestures recognition with pressure sensor array and radar," *IEEE Journal of Electromagnetics, RF and Microwaves in Medicine and Biology*, 2019, to be published. DOI: 10.1109/JERM.2019.2949456 (cit. on p. 123).

[LSH+19] H. Li *et al.*, "Magnetic and radar sensing for multimodal remote health monitoring," *IEEE Sensors Journal*, vol. 19, no. 20, pp. 8979–8989, Oct. 2019. DOI: 10.1109/JSEN.2018.2872894 (cit. on p. 123).

[SÖG18] M. S. Seyfioğlu, A. M. Özbaygglu, and S. Z. Gürbüz, "Deep convolutional autoencoder for radar-based classification of similar aided and unaided human activities," *IEEE Transactions on Aerospace and Electronic Systems*, vol. 54, no. 4, pp. 1709–1723, Aug. 2018. DOI: 10.1109/TAES.2018.2799758 (cit. on p. 124).

[SEGA18] M. S. Seyfioğlu *et al.*, "Diversified radar micro-Doppler simulations as training data for deep residual neural networks," in *IEEE Radar Conference*, 2018. DOI: 10.1109/RADAR.2018.8378629 (cit. on p. 124).

[TSM+18] F. K. Teklehaymanot *et al.*, "Bayesian target enumeration and labeling using radar data of human gait," in *European Signal Processing Conference*, 2018. DOI: 10.23919/EUSIPCO.2018.8553444 (cit. on p. 125).

[VKJ+18] B. Vandersmissen *et al.*, "Indoor person identification using a low-power FMCW radar," *IEEE Transactions on Geoscience and Remote Sensing*, vol. 56, no. 7, pp. 3941–3952, Jul. 2018. DOI: 10.1109/TGRS.2018.2816812 (cit. on p. 125).

APPENDIX

A.1 FUNDAMENTALS

A.1.1 *Estimation of Noise Level in the Spectrogram*

For each measurement, the noise level in the spectrogam is estimated based on samples from a Doppler frequency band without signal components (see blue dashed box in Fig. A.1a). Assuming a normal distribution, the mean and standard deviation are estimated based on the noisy samples, i.e., $\hat{\mu}_{\text{noise}}$ and $\hat{\sigma}_{\text{noise}}$. The threshold is then calculated as $\tau_{\text{noise}} = \hat{\mu}_{\text{noise}} + 2\hat{\sigma}_{\text{noise}}$, as shown by the red dashed line in Fig. A.1b. All amplitudes in the spectrogram smaller than the noise threshold are set to τ_{noise}. For comparison, the histogram found from samples containing also signal components is shown in green in Fig. A.1b.

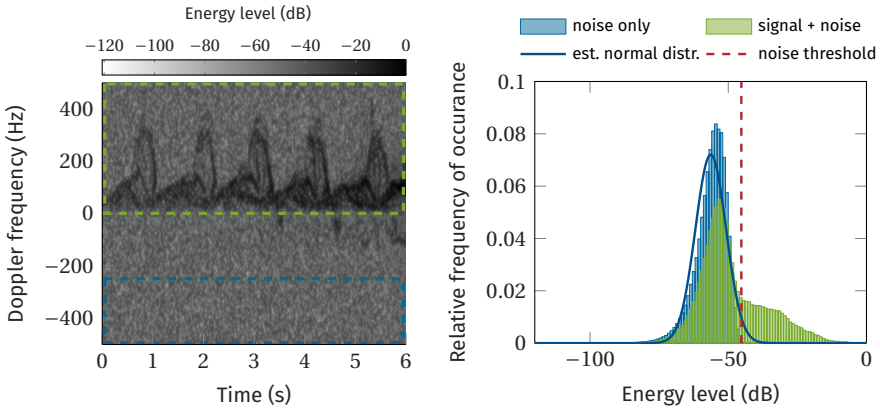

(a) noisy spectrogram

(b) threshold estimation

Figure A.1: Estimation of noise threshold. From (a) the noisy spectrogram, a Doppler frequency band containing only noise is extracted (blue dashed box). (b) The threshold is calculated based on the estimated distribution of the noisy samples (blue).

A.2 RADAR-BASED GAIT CLASSIFICATION

A.2.1 *Cadence-Velocity Diagrams of Persons With Diagnosed Gait Disorders*

Figures A.2 and A.3 show examples of cadence-velocity diagrams (CVDs) for four individuals with diagnosed gait disorders (for details see Section 4.2). Along with the CVDs, the mean cadence spectra (MCS) are shown.

In the case of Person K, the asymmetry of the gait is more clearly revealed in the CVD than in the MCS as shown in Figs. A.2a and A.3a. While the latter has a clear peak at the stride rate of approximately 1.4 Hz, there are no apparent sub-harmonics. However, in the CVD the gait asymmetry becomes obvious beyond Doppler shifts of approximately 200 Hz. Here, a clear pattern with increased energy levels at half the stride rate and the stride rate itself is revealed.

As shown in Fig. A.2b, the MCS of Person L walking toward the radar systems is not conclusive. However, similarly to Person K, the asymmetric gait pattern is revealed in the CVD beyond 200 Hz, where there is not only an increased energy level at the stride rate (1.2 Hz), but also at half of it (0.6 Hz). When the

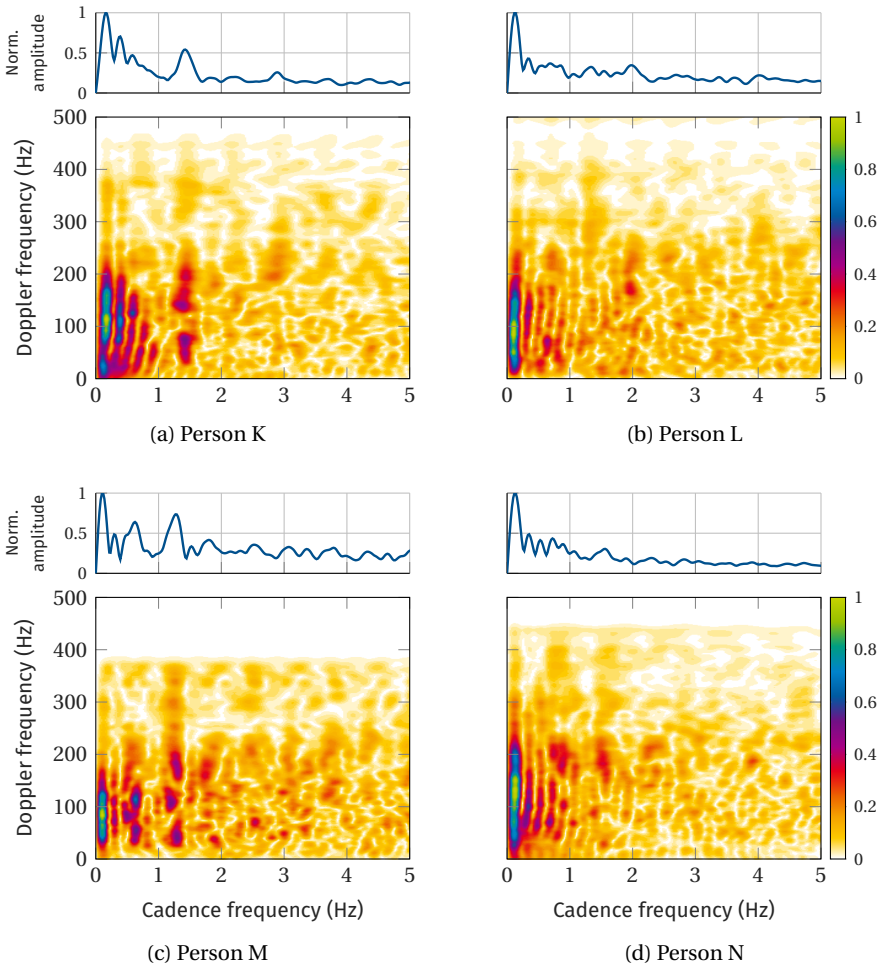

(a) Person K (b) Person L

(c) Person M (d) Person N

Figure A.2: Examples of CVDs and mean cadence spectra for Persons K–N walking toward the radar system. In the CVD, the color indicates normalized amplitudes. The CVDs are obtained from the spectrograms given in Fig. 5.5.

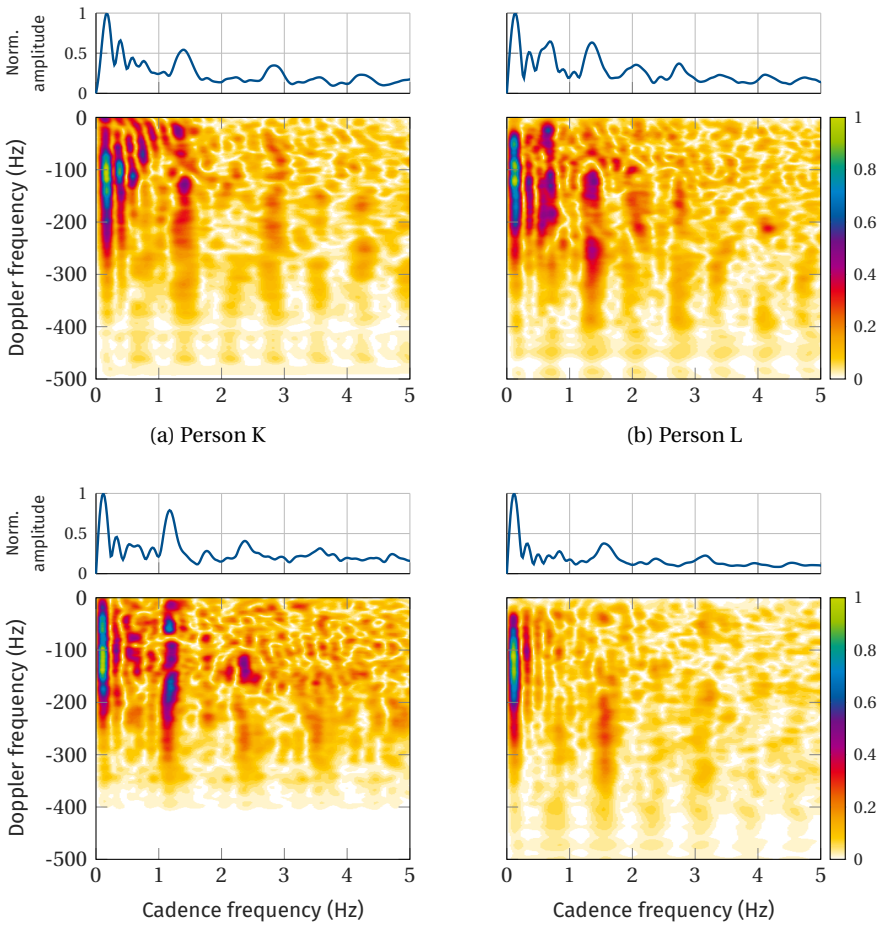

Figure A.3: Examples of CVDs and mean cadence spectra for Persons K–N walking away from the radar system. In the CVD, the color indicates normalized amplitudes. The CVDs are obtained from the spectrograms given in Fig. 5.6.

radar observes the gait of Person L from behind, the gait asymmetry is clearly revealed in both, the CVD and the MCS, as shown in Fig. A.3b.

Similarly, the CVD and the MCS in Fig. A.2c clearly indicate the asymmetry in the gait of Person M. Besides the stride rate of approximately 1.3 Hz, we also find significantly higher energy levels in the CVD and the MCS at half of the stride rate. As can be seen in Fig. A.3c, when the person is walking away from the radar, the CVD reveals the gait asymmetry when considering the cadence frequencies for Doppler shifts of approximately 220 Hz. The corresponding MCS has a clear peak at the stride rate of approximately 1.2 Hz, but shows only a weak sub-harmonic at half of the stride rate.

The CVD and the MCS of Person N walking toward the radar system, as shown in Fig. A.2d, are very similar to those of Person L. While the MCS does not have a clear peak at the stride rate, the CVD reveals both, the stride rate of approximately 1.6 Hz, and a sub-harmonic at 0.8 Hz beyond Doppler shifts of 180 Hz. When the gait of Person N is monitored from behind, as shown in Fig. A.3d, it is again difficult to assess the gait asymmetry from the MCS. However, the CVD clearly shows the gait asymmetry for Doppler shifts larger than 200 Hz.

A.2.2 *Eigenimages Obtained Through Principal Component Analysis of Cadence-Velocity Diagrams*

Figure A.4 shows examples of eigenimages of preprocessed cadence-velocity diagrams (CVDs). Bright and dark areas represent high and low amplitudes, respectively. Thus, the first eigenimage captures normal walking, with high amplitudes at f_{mD} and three harmonics with decreasing amplitudes. The second eigenimage is the inverse of the first eigenimage regarding the amplitudes. Here, the eigenimage shows high values at 1/3 and 2/3 of f_{mD}, which resembles the gait class CW/oos. Similarly, the third and fourth eigenimage can be interpreted to be representative for the gait classes CW and L1, with high values at 1/2 of f_{mD}.

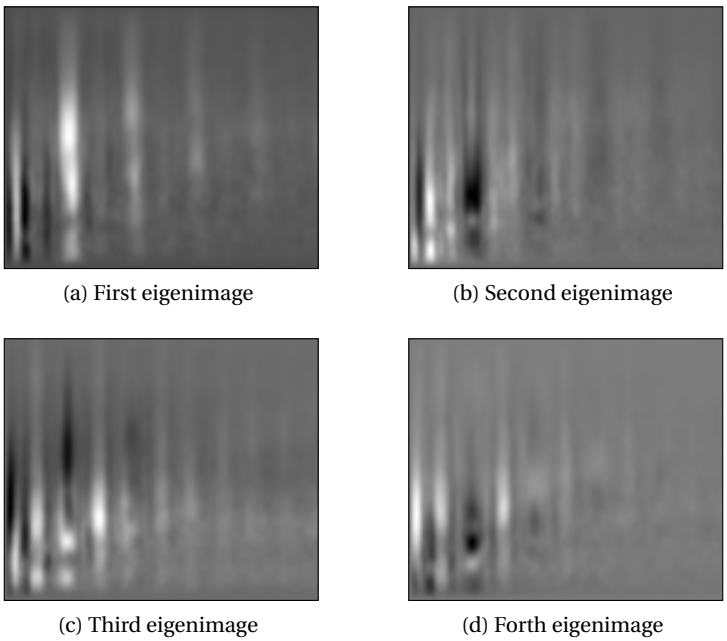

(a) First eigenimage (b) Second eigenimage

(c) Third eigenimage (d) Forth eigenimage

Figure A.4: Example of eigenimages of pre-processed CVDs corresponding to the first four principal components.

A.2.3 *Differently Preprocessed Cadence-Velocity Diagrams*

Figure A.5 shows examples of preprocessed cadence-velocity diagram (CVD) images that are used for automatic feature learning utilizing PCA. When compensating for different maximal Doppler shifts $f_{\mathrm{max}}^{\mathrm{D}}$ between measurements, the CVD is only considered up to the respective Doppler frequency. Different micro-Doppler repetition frequencies f_{mD} are compensated by warping the image along the horizontal image axis, i.e., compressing or stretching.

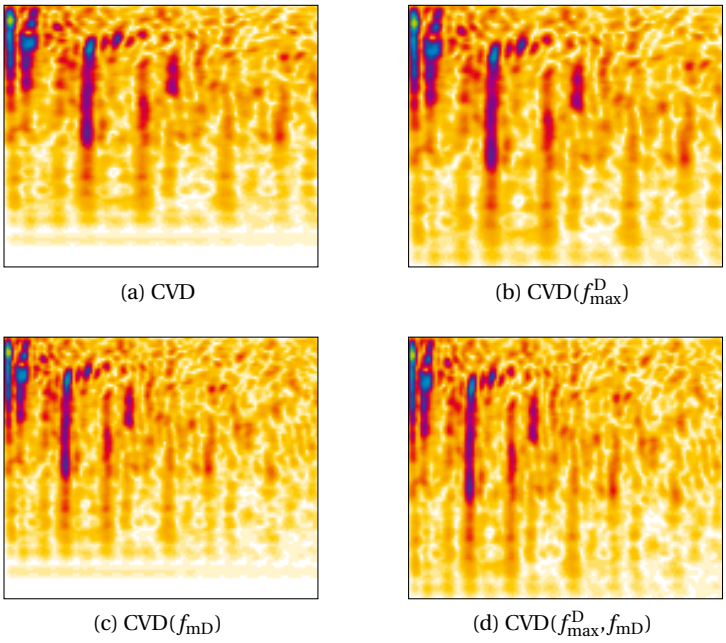

(a) CVD (b) CVD($f_{\mathrm{max}}^{\mathrm{D}}$)

(c) CVD(f_{mD}) (d) CVD($f_{\mathrm{max}}^{\mathrm{D}}$,$f_{\mathrm{mD}}$)

Figure A.5: Examples of preprocessed cadence-velocity diagram (CVD) images.

A.2.4 *Receiver Operating Characteristics for Gait Asymmetry Detection*

Figure A.6 shows the ROCs of the developed gait asymmetry detector for excluding one of the four individuals with diagnosed gait disorders (Persons K–N) from the training set. Generally, the performance of the detector is higher when monitoring the gait from behind (*away*). Not considering the motion direction (*both*), typically results in a decreased detection performance.

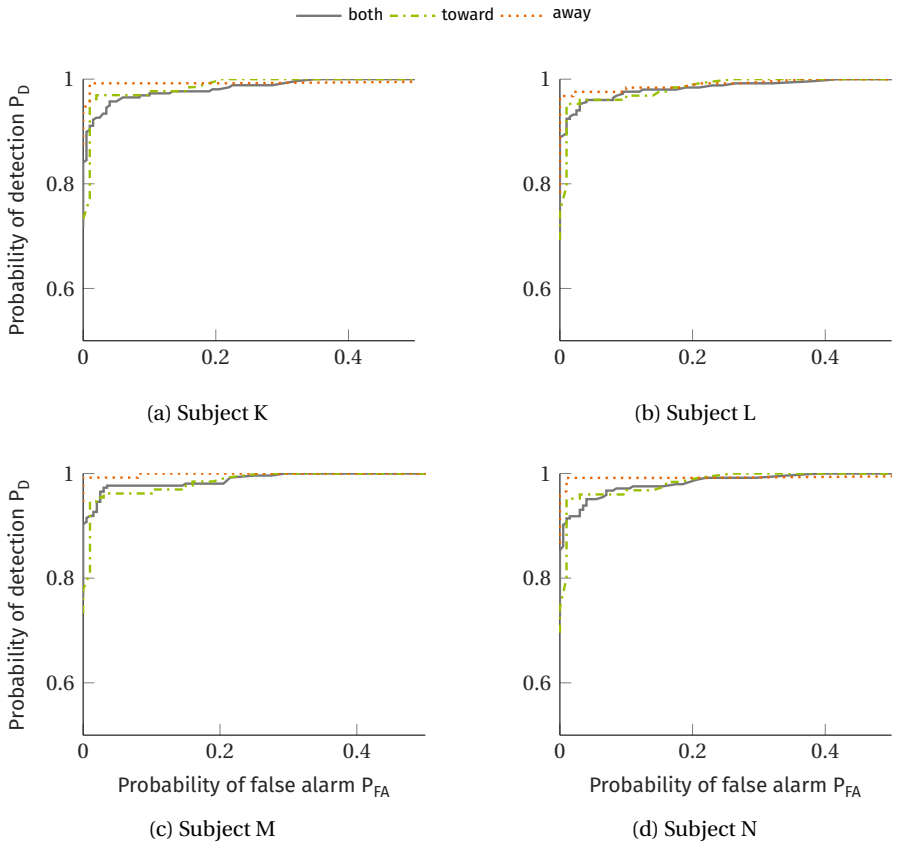

(a) Subject K

(b) Subject L

(c) Subject M

(d) Subject N

Figure A.6: Receiver operating characteristics (ROCs) for the best model per motion direction for the four individuals with diagnosed gait disorders (Persons K–N).

A.3 TOWARD RADAR-BASED GAIT ANALYSIS

A.3.1 *Effect of Knee Angle Confinement on the Analyzed Gait Parameters*

Table A.2 shows the mean values of the considered biomechanical gait parameters over all individuals. Here, both, the values measured by the radar and by the MoCap system are given. Due to the limited number of test subjects, these mean values are not conclusive, since (positive and negative) errors are averaged out. However, the table serves as reference for the magnitude of estimated values, and reveals significant trends in the data.

A.3.2 *Inter-Person Variability in Lower Limb Angular Kinematics*

Figure A.7 shows the MoCap-based hip and knee angle trajectories for all individuals averaged over all strides in a 100 s measurement. It can be seen that the inter-person variability is high for all knee angle confinements. For certain phases in the gait cycle, the variance across subjects even increases for constrained knee flexions.

A.3.3 *Validation of Proposed Lower Limb Velocity Models*

Table A.1 shows the RMSE between the MoCap-based trajectories of the knee and ankle joint and those obtained using Boulic's model (Eqs. (11.5) and (11.6)) in combination with the proposed models for the hip and knee angles (Eq. (11.8).

Table A.1: RMSE (mean ± SD over all test subjects in m/s) between MoCap-based velocities of the knee and ankle joint, and velocities obtained using Boulic's model with modeled hip and knee angle trajectories.

knee angle restriction	0.7 m/s		1.1 m/s	
	knee	ankle	knee	ankle
non	0.10 ± 0.02	0.30 ± 0.07	0.15 ± 0.02	0.33 ± 0.09
45°	0.11 ± 0.02	0.22 ± 0.05	0.13 ± 0.01	0.25 ± 0.07
30°	0.10 ± 0.02	0.18 ± 0.04	0.12 ± 0.03	0.26 ± 0.08
20°	0.11 ± 0.03	0.19 ± 0.04	0.12 ± 0.03	0.26 ± 0.07
10°	0.12 ± 0.03	0.19 ± 0.04	0.14 ± 0.04	0.26 ± 0.07
all	0.11 ± 0.02	0.21 ± 0.07	0.13 ± 0.03	0.27 ± 0.08

Table A.2: Effect of knee angle confinement on the analyzed gait parameters. For each treadmill speed (0.7 m/s, 1.1 m/s) and radar position (front, back), the table shows from left to right the mean values of each parameter for increasing knee restriction (no, 45°, 30°, 20°, 10°). The values in the first line are measured by a marker-based motion capture system and values in the second line are obtained using a Doppler radar system.

	0.7 m/s										1.1 m/s										unit
	front					back					front					back					
1) stride time	1.24	1.24	1.23	1.23	1.23	1.25	1.25	1.28	1.27	1.26	1.04	1.03	1.02	1.02	1.02	1.04	1.03	1.05	1.05	1.03	s
	1.24	1.24	1.23	1.23	1.23	1.25	1.25	1.28	1.27	1.26	1.04	1.03	1.02	1.02	1.02	1.04	1.03	1.05	1.05	1.03	
2) stance time	0.81	0.80	0.78	0.78	0.78	0.81	0.80	0.82	0.80	0.79	0.64	0.64	0.63	0.63	0.62	0.64	0.63	0.64	0.63	0.63	s
	0.81	0.80	0.77	0.78	0.79	0.81	0.80	0.77	0.76	0.77	0.68	0.67	0.65	0.66	0.64	0.66	0.63	0.66	0.64	0.63	
3) flight time	0.42	0.44	0.44	0.45	0.45	0.44	0.45	0.46	0.46	0.47	0.39	0.40	0.40	0.39	0.40	0.40	0.40	0.41	0.42	0.41	s
	0.43	0.44	0.45	0.45	0.43	0.45	0.45	0.51	0.51	0.48	0.36	0.36	0.37	0.37	0.38	0.38	0.40	0.39	0.40	0.40	
4) step time	0.62	0.61	0.61	0.60	0.60	0.63	0.62	0.63	0.62	0.61	0.52	0.51	0.51	0.50	0.50	0.52	0.51	0.52	0.51	0.51	s
	0.62	0.61	0.61	0.61	0.61	0.62	0.62	0.64	0.63	0.63	0.52	0.52	0.51	0.50	0.50	0.52	0.51	0.52	0.52	0.51	
5) cadence	97.64	97.37	98.37	98.15	98.69	96.38	96.49	94.24	95.02	95.88	116.02	116.32	117.73	117.92	118.07	116.01	116.47	114.56	114.72	116.41	steps/min
	97.63	97.36	98.35	98.17	98.67	96.42	96.47	94.26	95.03	95.88	116.02	116.31	117.73	117.91	118.08	116.01	116.46	114.55	114.71	116.39	
6) stride length	86.52	86.57	85.82	85.99	86.05	87.64	87.52	89.56	88.71	88.09	114.20	113.81	112.56	112.32	112.27	114.13	113.65	115.59	115.29	113.74	cm
	86.53	86.58	85.79	85.99	86.05	87.60	87.54	89.53	88.71	88.10	114.21	113.82	112.56	112.33	112.25	114.14	113.65	115.59	115.31	113.74	
7) step length	43.17	42.96	42.41	42.24	42.07	43.77	43.62	44.20	43.62	42.97	56.82	56.58	55.75	55.37	54.89	56.80	56.51	57.12	56.64	55.73	cm
	43.11	43.02	42.69	42.52	42.40	43.49	43.30	44.52	43.97	43.88	57.14	56.70	55.89	55.44	55.05	56.85	56.12	57.27	56.99	56.29	
8) max. foot velocity	2.00	2.01	1.96	1.95	1.92	2.00	2.00	1.94	1.92	1.89	2.63	2.67	2.65	2.63	2.59	2.63	2.65	2.59	2.54	2.56	m/s
	2.02	2.00	1.98	1.96	1.92	2.04	2.05	2.02	1.98	1.96	2.55	2.54	2.56	2.54	2.51	2.54	2.60	2.61	2.55	2.57	
9) max. ankle velocity	1.59	1.65	1.68	1.69	1.69	1.61	1.66	1.66	1.67	1.68	2.14	2.22	2.25	2.26	2.24	2.16	2.22	2.21	2.19	2.24	m/s
	1.61	1.61	1.66	1.62	1.64	1.82	1.80	1.83	1.80	1.79	2.12	2.09	2.08	2.09	2.07	2.21	2.19	2.23	2.18	2.20	
10) max. knee velocity	1.00	0.81	0.64	0.54	0.48	0.98	0.81	0.63	0.56	0.51	1.26	1.07	0.90	0.85	0.77	1.27	1.05	0.90	0.82	0.77	m/s
	0.99	0.89	0.70	0.62	0.54	0.78	0.64	0.51	0.56	0.49	1.17	1.08	0.91	0.84	0.71	1.07	0.90	0.78	0.76	0.66	
11) time max. knee vel.	63.44	61.28	62.47	61.68	61.47	63.53	61.58	62.84	63.37	62.16	60.11	59.22	59.79	59.79	59.21	59.95	58.47	60.21	59.74	59.11	%
	65.50	64.56	63.16	63.00	64.63	64.47	63.74	60.21	59.74	61.58	65.61	64.72	63.89	64.26	62.26	63.32	61.58	62.42	61.37	60.95	

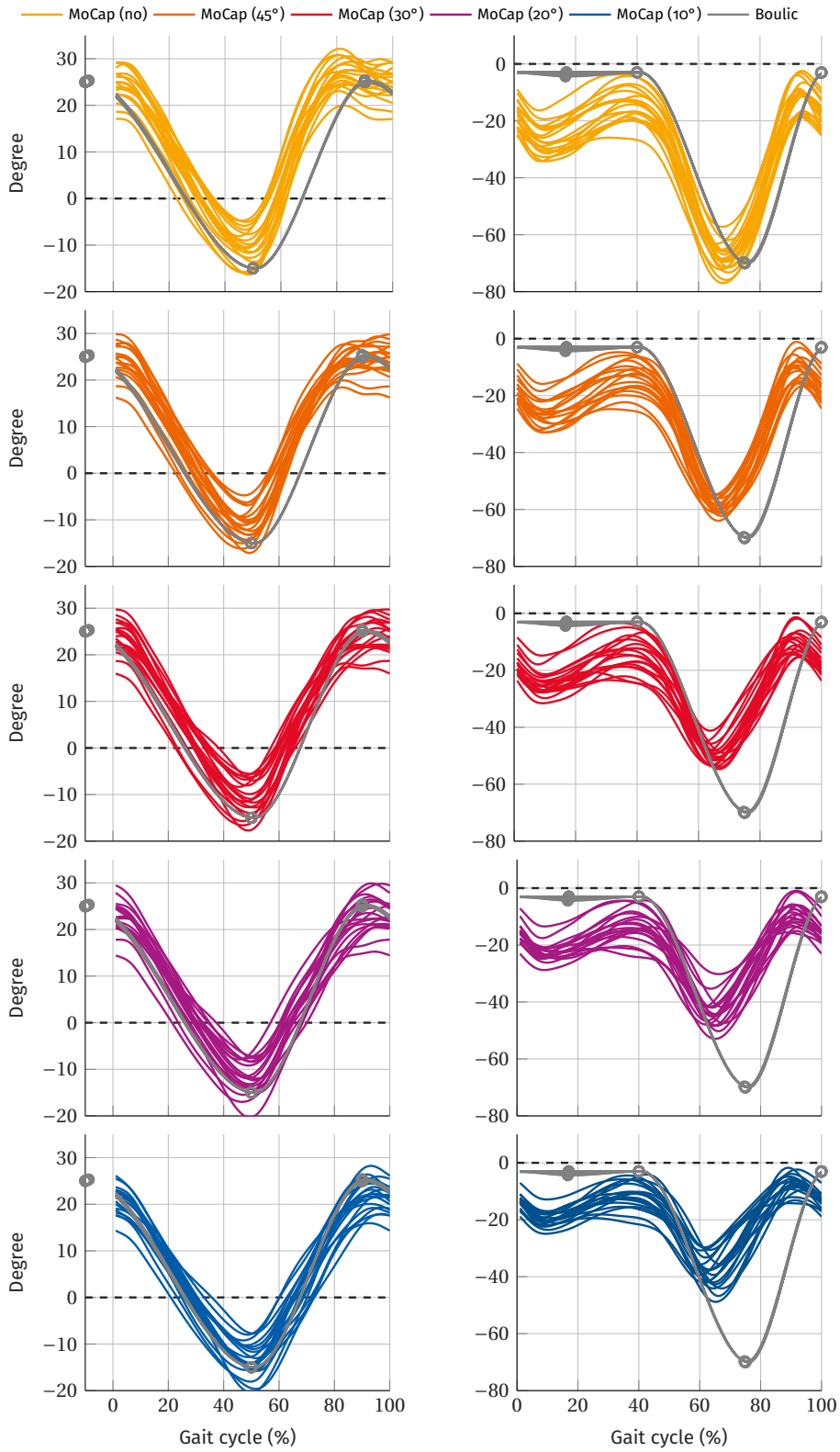

Figure A.7: Average MoCap hip and knee angle trajectories (over all strides in a measurement) of the right leg for each subject walking at a treadmill speed of 1.1 m/s. Angles according to Boulic *et al.* are shown in gray, where the gray circles mark the control points for the spline-based interpolation.

ERKLÄRUNGEN LAUT PROMOTIONSORDNUNG

§8 Abs. 1 lit. c PromO

Ich versichere hiermit, dass die elektronische Version meiner Dissertation mit der schriftlichen Version übereinstimmt.

§8 Abs. 1 lit. d PromO

Ich versichere hiermit, dass zu einem vorherigen Zeitpunkt noch keine Promotion versucht wurde. In diesem Fall sind nähere Angaben über Zeitpunkt, Hochschule, Dissertationsthema und Ergebnis dieses Versuchs mitzuteilen.

§9 Abs. 1 PromO

Ich versichere hiermit, dass die vorliegende Dissertation selbstständig und nur unter Verwendung der angegebenen Quellen verfasst wurde.

§9 Abs. 2 PromO

Die Arbeit hat bisher noch nicht zu Prüfungszwecken gedient.

Darmstadt, 15. Juni 2020

Ann-Kathrin Seifert

COLOPHON

This document was typeset using the typographical look-and-feel `classicthesis` developed by André Miede and Ivo Pletikosić. The style was inspired by Robert Bringhurst's seminal book on typography "*The Elements of Typographic Style*". `classicthesis` is available for both LaTeX and LyX:

https://bitbucket.org/amiede/classicthesis/

Happy users of `classicthesis` usually send a real postcard to the author, a collection of postcards received so far is featured here:

http://postcards.miede.de/